Le développement de LiDAR satellitaire multifonctions : analyse exploratoire du potentiel de capteurs LiDAR pour le suivi altimétrique et bathymétrique des surfaces en eau continentales et côtières

H. Abdallah

THESE

Pour obtenir le grade de

DOCTEUR DE L'UNIVERSITE MONTPELLIER II

École doctorale I2S (Information Structure Systèmes)

Spécialité : SYAM (Systèmes Automatiques et Microélectroniques)

Le développement de LiDAR satellitaire multifonctions. Analyse exploratoire du potentiel de capteurs LiDAR pour le suivi altimétrique et bathymétrique des surfaces en eau continentales et côtières

Présentée et soutenue par

Hani ABDALLAH

Le 14 Septembre 2012

Jury

M. Christophe DELACOURT, Professeur Université de Brest, Rapporteur

M. Laurent POLIDORI, Professeur CNAM, Rapporteur

M. Francesco ZUCCA, Chercheur Università degli studi di Pavia, Examinateur

M. Bruno CUGNY, Sous-Directeur adjoint charges Utiles Scientifiques, CNES, Examinateur

M. Nicolas BAGHDADI, Directeur de recherche, Irstea, Directeur de thèse

M. Jean-Stéphane BAILLY, Enseignant-Chercheur AgroParisTech, Co-directeur de thèse

Thèse préparée à l'unité mixte de recherche « Territoires, environnement, télédétection et information spatiale ».
UMR TETIS, Maison de la télédétection, 500 rue Jean-François Breton, 34093 Montpellier Cedex 5, France.

Résumé

Disposer de données précises, spatialisées et actualisées sur les niveaux et les profondeurs des eaux côtières ou continentales est nécessaire pour assurer et anticiper une meilleure gestion des eaux littorales et continentales. Parmi les techniques de télédétection de suivi de la bathymétrie et d'altimétrie des eaux, le LIDAR apparaît, de par son potentiel de précision, de résolution et de répétitivité spatiale des mesures, comme une technique adaptée et prometteuse, déjà éprouvée sur des plateformes aéroportées.

L'objectif de cette thèse est d'évaluer le potentiel du transfert de la technologie LiDAR sur satellite pour estimer l'altimétrie et la bathymétrie des eaux de surfaces continentales et côtières. Une approche expérimentale basée sur des données LiDAR réelles, puis une approche théorique basée sur des formes d'onde LiDAR simulées ont été utilisées pour explorer les performances de capteurs LiDAR satellitaires.

Dans une première partie, la qualité des données altimétriques du capteur LiDAR satellitaire GLAS/ICESat fut évaluée pour le suivi de l'altimétrie de plans d'eau. La méthode d'évaluation développée repose sur la prise en compte des phénomènes d'autocorrélation des mesures successives lors des comparaisons de l'élévation GLAS/ICESat avec les niveaux d'eau mesurés aux stations hydrométriques. Les précisions estimées sont de l'ordre de 12 cm.

Dans une seconde partie, un modèle de simulation des trains d'ondes LiDAR a été développé. La confrontation des simulations issues du modèle par comparaison à des trains d'ondes observés par des capteurs satellitaires et aéroportés a été effectuée.

Dans une dernière partie, les performances de deux configurations de potentiels capteurs LiDAR spatiaux émettant dans l'UV (355 nm) ou dans le vert (532 nm) ont été évaluées à partir des formes d'ondes simulées suivant des distributions globales des différents paramètres de l'eau assumées comme représentatives à l'échelle mondiale et pour quatre types d'eaux différents. Une analyse de sensibilité a été effectuée pour identifier et ordonner les paramètres environnementaux qui influent le plus sur l'écho LiDAR du fond de l'eau, signal déterminant dans la faisabilité de la mesure bathymétrique. Ensuite, les probabilités de mesure de la bathymétrie ainsi la précision sur l'estimation de la bathymétrie ont été calculées suivant un plan d'expérience qui respecte les distributions globales des paramètres d'eau. Cette thèse propose une méthodologie globale, point de départ pour explorer les performances globales et les facteurs limitant de futurs capteurs LiDAR satellitaires dédiés totalement ou partiellement à l'altimétrie et la bathymétrie des eaux côtières et continentales.

Abstract

Possessing accurate, spatial and current data on the water levels and the depths are necessary for anticipation and better management of coastal and continental waters. Among the remote sensing techniques to monitor the water bathymetry and altimetry, the LIDAR appears as an adapted and promising technique, already proven on airborne platforms, because of its potential accuracy, spatial resolution and repeatability of measurements.

The objective of this thesis is to evaluate the potential of the transfer technology on satellite LiDAR to estimate the water altimetry and bathymetry of continental and coastal areas. An experimental approach based on actual LiDAR data and a theoretical approach based on simulated LiDAR waveforms were used to explore the performance of satellite LiDAR sensors.

In the first part, the altimetry data quality from the satellite LiDAR sensor GLAS / ICESat was evaluated in order to monitor the altimetry of water bodies. The evaluation method developed is based on the consideration of the autocorrelation phenomena of successive measurements when comparing the elevation GLAS / ICESat with water levels measured at gauging stations. Accuracies are estimated in the order of 12 cm.

In the second part, a simulation model of LiDAR waveform has been developed. The confrontation between simulations from the model compared to observed waveform provided by satellite and aircraft sensors was performed.

In the last section, the performance of two space borne LiDAR emitting in the UV (355 nm) or the green (532 nm) were evaluated using a methodology based on waveform simulation following aggregate distributions of various water parameters assumed to be representative on a global scale and for four different types of water. A sensitivity analysis was performed to identify and order the environmental parameters that influence the most the LiDAR bottom echo of the water signal in determining the feasibility of measuring bathymetry. Then, the probability of measuring water depth and the accuracy of estimating the bathymetry were calculated according to an experimental design that meets the global distributions of water parameters. This thesis proposes a global methodology, a starting point to explore the overall performance and the limiting factors for future satellite LiDAR sensors totally or partially dedicated to altimetry and bathymetry of coastal and inland waters.

Remerciements

Je tiens en premier lieu à remercier très sincèrement mes deux directeurs Nicolas Baghdadi et Jean-Stéphane Bailly qui ont assuré avec une rigueur et un dynamisme sans faille l'encadrement de cette thèse. Ces travaux sont le résultat d'une direction impeccable. L'un et l'autre ont su m'apporter le savoir et le soutien indispensables à la réalisation d'un tel travail.

Mes premiers remerciements vont aussi au CNES et EADS qui m'ont permis de réaliser ce doctorat grâce à leur financement. Egalement un grand merci à l'Irstea de m'avoir accueilli pendant la durée de la thèse. Je remercie sincèrement Fréderic Fabre (EADS) et Yves Pastol (SHOM) pour leurs aides précieuses au cours de mes travaux de recherche et lors de la rédaction du présent mémoire.

Je remercie également toutes les personnes de la Maison de la Télédétection: Tristan, Marc, Maelle, Mohamed, Cédric, Roberto, Jean, Veonique, Isabelle...

Un énorme merci à mes amis de Montpellier, ceux avec eux j'ai passé des moments inoubliables: Mojtaba, Ali, Ziad, Marina, Farah, Rita, Reem, Mohamed, Suzan, Rana, Lama, Saeb, Elie, Jad. Une pensée toute spéciale va à mon ami Anass et sa femme Hazar et je n'oublie pas le petit Rayan.

Enfin, tout ce chemin n'aurait pu être parcouru sans le soutien et les encouragements de mes parents et de mon cousin Chadi Abdallah.

Table des matières

Introduction

Le développement de LiDAR satellitaire multifonctions. Analyse exploratoire du potentiel de capteurs LiDAR pour le suivi altimétrique et bathymétrique des surfaces en eau continentales et côtières

Introduction Générale

L'eau recouvre 360 millions de km^2 environ, soit 71% de la surface de la Terre. Toute mission spatiale d'observation de la terre à échantillonnage régulier sur la surface observe donc principalement des surfaces en eau.

Les eaux salées océaniques profondes et les eaux salées côtières représentent respectivement 93 % et 4 % de la réserve d'eau sur terre. Sur les 3% restant, les eaux douces continentales ne représentent que 0,65% et les eaux de surfaces (lacs, rivières, marais), facilement accessibles, seulement 0.3 % des ces eaux douces continentales (Cazenave et Nerem, 2002).

Dans les décennies à venir, l'accès à la ressource en eau douce, en termes de qualité et de quantité, sera un enjeu capital pour les usages domestiques, pour l'agriculture (et donc la satisfaction des besoins alimentaires mondiaux) et pour l'industrie (Cosgrove and Rijsberman, 2000).

Les zones côtières, quant à elles, figurent parmi les lieux les plus évolutifs de la planète. A l'interface entre milieu océanique et terrestre, elles sont le lieu de processus géomorphologiques très actifs (érosion) et subissent de nombreux aléas : tempêtes, ouragans, cyclones et tsunamis. De surcroît, elles concentrent près des deux tiers de la population mondiale, leur niveau d'occupation est cinq fois plus élevé que la densité moyenne des terres habitées et elles comptent huit des dix plus grandes agglomérations du globe (McGranahan et al., 2007). D'ici trente ans, on estime que les trois quarts de l'humanité vivront dans des zones proches du rivage. Qui plus est, les risques côtiers liés à la sécurité de la navigation proche du rivage (pollutions, naufrages, etc) qui est une préoccupation traditionnelle des zones côtières, demeurent un enjeu majeur, du fait de l'intensification du trafic maritime, d'une hétérogénéité des cartes marines et d'une méconnaissance de la bathymétrie (Ward and Gallaher, 2011). En effet, la plupart des services hydrographiques sont obligés par l'OHI (Organisation Hydrographique Internationale) de produire des cartes marines qui couvrent leurs eaux nationales en nombre suffisant et à des échelles qui permettent, dans les eaux côtières, une navigation sûre à toutes les catégories de navires, des plus petits aux plus grands, y compris pour les grands ports dans lesquels font escale les plus gros navires. Sous cet aspect chaque pays membre de l'OHI est obligé de publier les cartes de ses propres eaux (OHI, Edition

4.2.0, 2008). De fait, les zones côtières sont des zones à risques importants, accrus par une pression anthropique croissante et les effets du changement climatique (élévation du niveau de la mer).

Ces quelques enjeux suffisent à démontrer la place centrale qu'occupent aujourd'hui les eaux côtières et continentales au sein des activités humaines. La connaissance de leurs caractéristiques physiques et leur suivi sont donc un enjeu scientifique majeur. Disposer de données précises, homogènes, spatialisées et actualisées sur les niveaux et les profondeurs des eaux côtières ou continentales, définies respectivement par l'altimétrie et la bathymétrie, est une des clés d'une meilleure gestion des eaux littorales et continentales.

1. Contexte

1.1. Contexte sociétal de l'altimétrie des eaux

Le suivi du niveau des eaux océaniques et côtières permet la prévention des risques liés au réchauffement climatique. Le réchauffement climatique a pour conséquence la montée du niveau des mers et des océans, du fait de la fonte des calottes glacières, et provoque la dilatation thermique des eaux (Vorosmarty et al., 2000). Les climatologues de la NASA estiment l'élévation du niveau des mers et des océans à environ 2,25 mètres d'ici la fin du siècle (Houghton et al., 2001). Cette élévation n'est pas uniforme sur tout le globe et pourra aller de quelques dizaines de centimètres à plusieurs mètres. La conséquence la plus importante de cette élévation des eaux est l'inondation des zones côtières où 634 millions de personnes vivent à 10 mètres ou moins du niveau de la mer (Brown, 2011). La montée des eaux combinée à des événements climatiques (tempêtes**,** cyclones**,** ouragans) provoquerait l'inondation de la majeure partie de ces zones vulnérables (McCulloch et al,. 2002). De plus, cette élévation du niveau des mers aurait comme incidence d'accroître les problèmes d'érosion côtière de certaines régions (Ruggiero et al., 2001). La submersion des rives et les glissements de terrains pourraient également devenir plus fréquents, particulièrement dans les zones côtières sensibles.

Le suivi de l'altimétrie des eaux continentales permet quant à lui i) le suivi du régime hydrologique des cours d'eaux en participant à l'estimation des débits (Leon et al., 2006) et ii) le suivi des flux d'eaux dans les lacs reconnu comme une source

supplémentaire d'information utile des ressources en eau, réserves d'eau douce accessibles à une hauteur de 68 % (Cretaux et Birkett, 2006). Pour ces deux points, l'altimétrie permet une meilleure connaissance du cycle de l'eau sur les surfaces émergées et donc une meilleure prévision du climat et un contrôle plus fin des ressources en eau de la planète, du moins lorsque le suivi altimétrique est rendu systématique (Frappart et al., 2005; Lee et al., 2009).

1.2. Contexte sociétal de la bathymétrie des eaux

Au-delà de la mesure des niveaux (altimétrie) sur les eaux, la mesure de profondeur de l'eau (bathymétrie) et de la géométrie des surfaces immergées sont deux autres caractéristiques physiques d'importance des eaux côtières et continentales.

La bathymétrie des eaux côtières peut répondre aux enjeux (i) de protection du littoral contre l'érosion qui provoque une modification du trait de côte et altère la faune et la flore littorale (Gopinath and Seralathan, 2005), (ii) de délimitation maritime avec pour objet l'établissement de cartes de navigation maritime et de frontières entre les zones maritimes (Miles, 1998) et (iii) d'aménagement du territoire (Clark, 1995, Von Szalay and McConnaughey, 2002). Pour le premier point, les zones côtières connaissent un recul spectaculaire suite aux actions érosives des facteurs naturels (houle, marée, vent) et anthropiques (aménagement et constructions balnéaires). Ces facteurs sont à l'origine, en général, d'un déséquilibre sédimentaire au niveau des côtes qui se manifeste par une érosion plus ou moins importante et rapide. En conséquence, le suivi topographique et géomorphologique des fonds côtiers est un besoin majeur identifié pour lutter contre l'érosion des côtes (Esteves et al., 2002). Pour le deuxième point, des normes de précision bathymétrique ont été définis par plusieurs organismes :

- l'Organisation Hydrographique Internationale (OHI) a déclaré en 2008, pour la bathymétrie des eaux côtières, (i) une précision bathymétrique verticale demandée de l'ordre de 25 cm, ainsi une pénétration maximale à 40 m de profondeur dans des conditions idéales (Hilldale and Raff, 2007). (ii) Pour les eaux ayant une profondeur maximale de 100m, la précision verticale demandée est de 50 cm (IHO Standard, 2008).

- Le U.S. Army Corps of Engineers déclare des spécifications légèrement différentes : 15 cm de précision verticale et une profondeur de pénétration de 40 m (Lillycrop et al., 1996).
- Le Service Hydrographique et Océanographique de la Marine Français (SHOM) et l'Institut national de l'information géographique et forestière (IGN) se sont associés pour la constitution d'un référentiel géométrique tridimensionnel à haute résolution et continu terre-mer sur la bande littorale du territoire français définie par le projet Litto3D. Les normes bathymétriques ont été déclarées en 2008 pour ce projet suivant une précision verticale de 20 cm et une profondeur maximale de 40 m avec une haute densité de sondage (2points/m²) (Jolivet et al., 2009).

La bathymétrie des eaux continentales (rivières, fleuves et lacs) peut répondre aux enjeux 1) de calcul des flux hydrauliques et de mesures de débits 2) de caractérisation des habitats aquatiques, notamment piscicoles, en couplant la mesure bathymétrique à un modèle hydraulique (vitesse, matières en suspension) (Hilldale and Mooney, 2007) et 3) de caractérisation de changements géomorphologiques liés aux flux sédimentaires provenant de mécanismes de transport et dépôts solides. La bathymétrie des eaux continentales permet donc d'appuyer une démarche de gestion durable des lacs et cours d'eaux (Lane et al., 1994; Marks and Bates, 2000; Westaway et al., 2000).

2. Techniques de mesures altimétriques et bathymétriques

2.1. Altimétrie de surfaces en eau

2.1.1. Systèmes de mesure au sol

Le suivi du niveau des eaux a été assuré jusqu'à présent par des réseaux de stations limnimétriques au sol (capteurs capacitifs, capteurs de pression, capteurs bulle à bulle, échelle analogique, etc) organisées généralement par pays ou région. Ces réseaux sont chargés de mesurer les variations temporelles des niveaux d'eau. Cette technique connaît un véritable déclin depuis une vingtaine d'années dû aux interruptions intempestives des enregistrements, et aux coûts d'entretien des stations. D'autre part, les temps d'accès à ces informations sont souvent incompatibles avec les systèmes de prévision qui seraient nécessaires (Calmant and

Seyler, 2006, Créteaux and Birkett, 2006). Ce déclin est particulièrement important dans les régions pauvres où les moyens technologiques et les infrastructures manquent cruellement. Dans cette situation d'accroissement des besoins en eau et de diminution des systèmes terrestres de quantification de cette ressource, il devient essentiel de diminuer les coûts, donc d'optimiser et de pérenniser les systèmes de mesure, et de diminuer les temps d'accès aux données.

2.1.2. RADAR

L'altimétrie satellitaire radar a connu un très fort développement au cours des trois dernières décennies sur la base d'une finalité majeure de suivi dans le temps et dans l'espace du niveau des océans au service de différentes applications en océanographie. Les développements méthodologiques sont entrés en phase opérationnelle avec les satellites ERS-1/2 et Topex/Poséidon suivis d'ENVISAT, Jason-1 et Jason-2. La couverture spatiale quasi-globale et la périodicité temporelle adaptée à l'observation des phénomènes hydrologiques ont montré un potentiel très favorable pour le suivi des eaux continentales. Les études préliminaires dans ce domaine ont commencé avec SKYLAB (Brown, 1977), GEOS 3 (Miller, 1979), et ERS1 (Mason et al., 1985). Cependant, les missions Seasat (Brooks, 1982), Geosat (Koblinsky et al., 1993; Morris et Gill, 1994a) et Topex/Poseidon (Morris and Gill, 1994b; Birkett, 1995a), sont celles qui ont permis de développer des études plus concrètes sur les surfaces d'eau continentale comme les grands lacs américains et africains ainsi que les mers intérieures (Ponchaut et Cazenave, 1998; Birkett et al., 1999; Cazenave et al., 1997; Birkett, 1995b; Mercier, 2001; Mercier et al., 2002, Aladin et al., 2005). Finalement, c'est à partir de 1998 que les mesures d'altimétrie radar ont commencé à être exploitées pour l'hydrologie des grands bassins fluviaux et en particulier pour le bassin Amazonien (Birkett, 1998; De Oliveira Campos et al., 2001; Birkett et al., 2002; Maheu et al., 2003; Kouraev et al., 2004; Frappart et al., 2005 ; Kosuth et al., 2006). Les systèmes radars altimétriques utilisent généralement un système géodésique propre (modèle ellipsoïdal terrestre). C'est le système géodésique mondial WGS84 qui est le plus fréquemment utilisé comme référence avec le modèle de géoïde EGM96 (Bercher, 2008).

L'empreinte au sol (ou spot) du satellite Topex/Poséidon varie de quelques centaines de mètres à quelques kilomètres, ce qui restreint les études hydrologiques à la mesure moyenne sur des cibles de grande dimension tels que les grands lacs. Les

précisions trouvées varient de quelques centimètres sur les Grands Lacs aux États-Unis (Morris et Gill, 1994) à une dizaine de centimètres pour le lac Tchad en Afrique (Birkett ; 2000). Des résultats similaires ont été obtenus sur le lac Issykkul au Kirghizistan avec une précision de 5 cm et sur le lac Chardarya au Kazakhstan avec une précision de 10 cm (Crétaux et Birkett, 2006). Dans toutes ces études, les précisions obtenues sont directement liés à la taille des plans d'eau puisque la mesure par satellite par rapport à la réalité de terrain est généralement obtenue en faisant la moyenne de mesures individuelles prise le long de la trace du satellite. Pour cette raison, le cas des rivières apparaît plus difficile à étudier en raison de leur dimension (largeur) réduite. Les premières études relatives aux cours d'eau ont été effectuées dans le bassin amazonien, où les fleuves et rivières sont de dimension importante ; des précisions de mesure altimétrique allant de 40 cm et 1.1 m ont été obtenues (Birkett et al. 2002 ; Bercher, 2008).

L'utilisation de données de radars altimétriques sur les eaux continentales est récente et elle présente encore plusieurs difficultés (Calmant et Seyler, 2006). Citons entre autres : i) la dimension du spot, large de plusieurs centaines de mètres, qui restreint la possibilité de mesure à des lacs et des cours d'eau de grandes dimensions (au moins de l'ordre de 2 fois la taille du spot) ; ii) du point de vue de la mesure altimétrique, il est possible de considérer les eaux océaniques comme un milieu homogène : l'écho radar n'est réfléchi que par l'eau. Par contre, en milieu continental, cette situation ne se reproduira que sur les grandes surfaces en eau comme sur les grands lacs ou les fleuves larges sinon, la tache au sol de l'altimètre sera fréquemment perturbée par la présence de terres émergées. Interprétée comme une hétérogénéité de la surface réfléchissante, cette perturbation a des conséquences notables sur le fonctionnement de l'instrument et la précision des mesures.

2.1.3. LiDAR altimétriques aéroportés

L'acronyme LiDAR signifie Ligth Detection And Ranging. Un LiDAR se compose d'un laser chargé d'émettre l'onde lumineuse et d'un télescope qui collecte l'onde rétrodiffusée par une cible et d'une chaîne de traitement numérique qui quantifie le signal reçu. Un LiDAR altimétrique aéroporté est un distance-mètre laser à balayage porté par un vecteur aérien (un avion en général). La position de l'avion et son orientation absolue (ou attitude) est donnée par un système de positionnement

composé d'un récepteur D-GPS et d'une centrale inertielle. Le laser émet des impulsions à haute fréquence (quelques dizaines de kHz). Un système de balayage (en général un miroir oscillant) dévie le faisceau laser de part et d'autre de la trace de l'avion, de façon à couvrir une surface en un seul passage.

Le LiDAR altimétrique émet une impulsion laser généralement dans le proche infrarouge (1064 nm) qui sera réfléchie par la surface de l'eau. La durée du trajet aller-retour de l'impulsion permet la mesure de la distance entre le capteur et la surface de l'eau puis le calcul de la côte de la cible (altimétrie) (Guenther, 2000).

Dans le cadre de l'altimétrie des surfaces en eaux, il n'y a pas de LiDAR aéroporté complètement dédié à cette application. Les LiDAR altimétriques aéroportés standard émettant dans le Proche Infra Rouge (PIR) ont même une sensibilité des détecteurs telle qu'ils n'enregistrent pas d'écho rétro-diffusés par les surfaces en eau (faible puissance reçue) afin de ne pas saturer le signal reçu par des cibles beaucoup plus réfléchissantes (terre). Seuls des capteurs LiDAR aéroportés dédiés, dit « hydrographiques » ou « bathymétriques », et s'appuyant sur des lasers PIR ou vert permettent l'altimétrie de surfaces en eau. Dans ce cadre, outre le coût important de telles missions (Baltsavias, 1999) et l'inhomogénéité des données issues de ces capteurs d'un site à l'autre (Bilodeau, 2010), les principaux avantages du LiDAR aéroportés sont :

- la densité spatiale élevée des mesures. Ces systèmes émettant généralement à 10 ou 30 kHz (DeJoinville et al., 2002), il est alors possible de mesurer l'altitude d'une surface en un grand nombre de point, la densité de points au sol étant généralement de l'ordre de 0,1 à 5 points par m² (Bergeon, 2004).
- la précision de la mesure altimétrique, de l'ordre de 10 cm (Ackermann, 1999; Hodgson & Bresnahan, 2004).

2.1.4. LiDAR altimétrique satellitaire

Le 13 janvier 2003, ICESat (Ice, Cloud, and land Elevation Satellite) a été mis en orbite par le fusée Delta II depuis la base de lancement de Vandenberg en Californie et placé sur une orbite polaire à une altitude de 600 km. La mission s'est arrêtée le 14 août 2010. Le Geoscience Laser Altimeter System (GLAS) embarqué à bord du satellite ICESat était le premier instrument LiDAR qui équipait un satellite pour l'observation globale et continue de la Terre. Le premier objectif était de déterminer

le bilan de masse des calottes polaires et leurs contributions aux changements du niveau des océans. Le deuxième objectif était de mesurer la hauteur des nuages et des aérosols dans l'atmosphère, et de cartographier la topographie des surfaces terrestres (Zwally et al., 2002).

L'instrument GLAS transmet des courtes impulsions (4-6 ns) dans l'infrarouge (1064 nm) et le vert (532 nm) à une fréquence de 40 Hz, ce qui correspond à une mesure le long de la trace tous les 170 m. L'infrarouge est utilisé pour mesurer l'altimétrie des surfaces et le vert pour mesurer la distribution verticale des nuages et des aérosols. La mission prévoyait plusieurs périodes d'exploitations à raison de trois campagnes par an pendant cinq ans, ce qui a fourni des données d'élévation sur toutes les surfaces de la terre. GLAS offre un potentiel intéressant pour la caractérisation des eaux continentales grâce à son empreinte au sol de diamètre 70 m en moyenne (50 à 90m).

Avec GLAS, les précisions altimétriques estimées sur les grands lacs américains et notamment le lac américain Pontchartrain (Etats-Unis d'Amérique) sont de 3 à 8 cm pour la RMSE (Root Mean Square Error) (Chipman et Lillesand, 2007 ; Urban et al., 2008). Sur des lacs de petites tailles, par exemple dans le Minnesota (États Unis), la précision estimée est d'environ 20 cm (Bhang et al., 2007). Les cours d'eau ont fait l'objet de très peu d'études jusqu'à présent. En 2006, Urban et al., a étudié la précision de GLAS sur le fleuve du Tapajos (bassin amazonien) en utilisant une trace ICESAT exceptionnellement longue de 50 km. La précision obtenue est de 3 cm par beau temps, 8 à 15 cm sous ciel partiellement nuageux et de 25 cm par mauvais temps. En effet, le signal GLAS est suffisant pour pénétrer une fraction importante de nuages et obtenir un écho de surface pour une mesure de l'altitude. Dans certaines conditions de transmission à travers les nuages, la rétrodiffusion des photons laser par les nuages entraine le retard de quelques photons en prenant un chemin plus long tout en restant dans le champ de vue de GLAS. Le signal pour les photons retardés apparaît plus tard dans la forme d'onde reçue ce qui affecte la précision altimétrique (Duda et al., 2000).

2.2. Bathymétrie

2.2.1. Techniques passives : imagerie optique

Des techniques passives de télédétection basées sur l'utilisation d'images optiques conjointement à une calibration terrain permettent d'estimer la profondeur de l'eau à partir des comptes numériques de l'image acquise (Marcus et al., 2003; Gao, 2009). Les capteurs optiques passifs qui ont comme source d'illumination le soleil mesurent la réflectance, c'est-à-dire l'intensité du rayonnement solaire réfléchi par la surface, la colonne et le fond de l'eau. Lorsque les propriétés optiques de la surface de l'eau, de la colonne d'eau et du fond de l'eau sont homogènes, il existe une relation linéaire décroissante entre le logarithme de la réflectance et la profondeur (Lyzenga 1978) : plus la profondeur est grande plus le rayonnement est absorbé et plus la réflectance mesurée est faible (Chaponnière, 2004).

La télédétection optique passive s'est beaucoup développée en imagerie multispectrale (LANDSAT, SPOT, IKONOS …) (Lafond et al., 2002 ; Lyzenga et al., 2006). Ces capteurs mutlispectraux ont montré leur potentiel pour le suivi de la turbidité, des concentrations en particules minérales en suspension, en chlorophylle, en matières organiques dissoutes colorées, et l'estimation de la profondeur d'eau (Binding et al., 2005; Alder-Golden et al., 2005). Les capteurs hyperspectraux, aéroportés ou satellitaires (AVIRIS, CASI, Hyperion …), fournissent des images de la Terre dans environ 200 bandes spectrales du visible au proche-infrarouge ((0,4-2,5µm), (3-5µm) et (8-12µm)) (Jing et Datt, 2010). L'imagerie hyperspectrale permet d'une part l'augmentation de la précision d'estimation des variables actuellement observées par les capteurs multispectraux (turbidité, pigments, matière organique dissoute, matière en suspension, bathymétrie), et d'autre part l'accès à de nouvelles variables d'intérêt (type et taille de particules en suspension, types de pigments, de matière organique, cyanobactéries, polluants inorganiques, etc.) (Hegee et al., 2007).

Depuis les années 90, la résolution spatiale des capteurs hyperspectraux s'est améliorée et les applications se sont aussi beaucoup développées pour les zones côtières pour lesquelles la résolution est mieux adaptée (Lei, 2011). L'amélioration de la résolution spectrale permet aussi de d'estimer avec plus de précision les composants de l'eau, de cartographier le fond ou d'estimer la bathymétrie.

Les capteurs passifs satellitaires ne permettent généralement pas d'acquérir d'images avec une très haute résolution temporelle (période de revisite va de 1 à 3 jours selon la résolution de l'image et en l'absence de nuages). Pour certains processus très dynamiques, comme les malaïques, les inondations, les effets de la marée sur l'environnement côtier, les cycles journaliers du phytoplancton (bloom), les capteurs passifs satellitaires ont une résolution temporelle trop faible (Lei, 2011). L'imagerie optique est de plus fortement limitée par la nécessité de prendre simultanément des mesures in-situ au moment de l'acquisition de l'image (Gao, 2009).

De nombreux algorithmes basés sur la physique du transfert radiatif dans l'eau à partir de l'imagerie optique (multispectrale ou hyperspectrale) relient les grandeurs optiques mesurées à celles des fonds peu profonds (Lyzenga, 1978 ; Bierwirth et al., 1993 ; Maritorena et al., 1994 ; Lee et al., 1998), à celles de la colonne d'eau (Lee et al., 1994 ; Maritorena, 1996 ; Lee et al., 1999) et à la bathymétrie (Philpot, 1989 ; Loubersac et al., 1991 ; Lee et al., 1999). Ces algorithmes permettent donc d'étudier les paramètres physico-chimiques des eaux. L'étude de la nature des fonds immergés, de la bathymétrie, ou des caractéristiques de la colonne d'eau dépend de la profondeur de pénétration du signal incident et de sa réflexion, pour une bande spectrale donnée. Pour des eaux claires, ce sont les canaux situés dans la gamme 400-500 nm, qui pénètrent le plus profondément dans la colonne d'eau, alors que pour des eaux davantage chargées en particules et substances dissoutes, les plus grandes profondeurs sont atteintes dans la gamme 500-600 nm. Ces « grandes » profondeurs restent toutefois limitées à 25-30 m dans les eaux claires (Philpot, 1989). Plusieurs études ont été effectuées pour cartographier les fonds des rivières à partir d'images optiques (Winterbottom and Gilvear, 1997; Hardy et al., 1994; Gilvear et al., 2004; Leckie et al., 2005; Jing et Datt, 2010; Kanno et Tanaka, 2012). La plupart de ces méthodes reposent sur une phase d'apprentissage de terrain qui nécessite un jeu de données de terrain de calage. Morel (1998) a proposé une méthode pour calculer la profondeur d'eau à partir des images de télédétection sans faire des mesures in situ des profondeurs suivant la méthode appelée 4SM (Self-calibrated Spectral Supervised Shallow-water). Cette méthode s'appuie sur un modèle de transfert radiative (Lysenga, 1978) qui utilise l'imagerie multispectrale ou

hyperspectrale pour obtenir une correction de la radiance spectrale dans la colonne d'eau et produire une estimation de la profondeur de l'eau à chaque pixel de l'image. 4SM utilise, sur les zones marines, les coefficients d'atténuation spectrale des eaux marines provenant de la classification de Jerlov (Jerlov, 1976). Tous les pixels à faible bathymétrie de l'image se trouvent entre les pixels les plus clairs et la droite des sols (réflectance des fonds). Cette méthode permet d'estimer la bathymétrie et la réflectance spectrale du fond pour chaque pixel.

De plus, dernièrement Walther et al., (2011) a proposé le modèle HAB (hydraulically assisted bathymetry). Ce modèle utilise une combinaison de données sur les débits (conservation du débit) et les données image pour calculer la profondeur d'eau en tous point (pixel), sans apport de données de calibration terrain(mesures de profondeurs in situ) au moment du vol. Elle peut être réalisée à partir de données images optiques multispectrale ou hyperspectrale.

Étant donné que le paramètre le plus limitant pour de telles approches passives est le coefficient d'atténuation de l'eau, la possibilité de mesurer la profondeur dépend donc fortement des conditions de turbidité (Feurer et al. 2008 ; Gao, 2009). Ce qui affecte fortement la précision de mesure. Qui plus est cette technique de mesure indirecte et basée sur de l'optique passive, n'est opérationnelle que sous bonne conditions atmosphériques.

L'estimation de la bathymétrie à l'aide d'imagerie multispectrale souffre d'un manque de robustesse vis-à-vis du type de fond car l'albédo du fond est un facteur important pour estimer la bathymétrie (Marcus et al., 2003, Gao et al., 2009). L'imagerie hyperspectrale à haute résolution spatiale (< 5 m) permet d'augmenter la précision bathymétrique (Lesser et Mobley, 2007; Kanno et Tanaka, 2012). Cette précision dépend fortement de la calibration de l'image hyperspectrale: le paramétrage de la correction atmosphérique et le paramétrage du modèle adopté pour estimer la bathymétrie. La précision bathymétrique en imagerie hyperspectrale est de l'ordre de 10 cm pour les faibles profondeurs (< 20m) (Brando et al., 2009, Liew et al., 2011; Jay et al., 2012).

2.2.2. Techniques actives : sondeurs acoustiques (SONAR)

Historiquement la bathymétrie est mesurée par la technique de plomb à sonde qui consiste à déterminer la profondeur de l'eau à l'aide d'une sonde à main.

Actuellement, la bathymétrie est le plus souvent mesurée par des sondeurs acoustiques. La profondeur est déduite de la mesure du temps de trajet d'un signal acoustique réfléchi par le fond. Il existe deux types de sondeurs acoustiques : les sondeurs mono-faisceau et les sondeurs multi-faisceaux.

Au début des années 1920 apparaît le premier sondeur mono-faisceau Allemand "German Meteor". Les sondeurs classiques mono-faisceaux émettent un faisceau d'ondes avec un angle de divergence compris entre 15° et 30°. Ils ne mesurent donc la profondeur des fonds qu'à la verticale du navire le long de la route suivie. Le signal acoustique est émis à la verticale du navire. La cartographie est alors réalisée à partir de bandes régulièrement espacées d'une centaine de mètres, obtenues grâce à de nombreux passages du bateau (Stocks, 1937). Connaissant la célérité moyenne du son dans l'eau, la mesure du temps de parcours permet d'accéder à la profondeur minimale entre l'émetteur-récepteur et le fond (Kenny et al., 2000).

En 1977, apparaît le premier sondeur multi-faisceaux « Jean Chalcot » (Renard et Allenou, 1979). Le principe de fonctionnement des sondeurs multi-faisceaux est basé sur des techniques acoustiques qui permettent, non plus de sonder uniquement à la verticale du navire comme le font les sondeurs mono-faisceaux, mais de mesurer les profondeurs sur toute une fauchée perpendiculaire à l'axe du bateau. La largeur de cette fauchée varie de 2 à 7 fois la profondeur. La technique généralement utilisée est dite des "faisceaux croisés" car l'émission du signal sonore et la réception de l'écho réfléchi s'effectuent sur le fond, selon des faisceaux perpendiculaires dont l'intersection représente la surface sondée. Le faisceau d'émission a une ouverture latérale étroite dans la direction longitudinale (typiquement de l'ordre de 1 à 5°) et large transversalement (typiquement 150°). La réception se fait par plusieurs faisceaux (20 à 200) assez larges longitudinalement (de l'ordre de 20°) et étroits dans le plan transversal (1 à 5°) (Lurton, 2000 ; Bisquay, 2001).

Les avantages des sondeurs acoustiques sont nombreux :

(i) il permet une exploration acoustique d'un large couloir, transversalement à la route du navire ;

(ii) la couverture bathymétrique est donc rapidement obtenue et une haute résolution spatiale (jusqu'à plusieurs sondes/m^2).

(iii) Systèmes versatiles, beaucoup plus portatifs, ils peuvent facilement être embarqués sur des petites plateformes à peu de frais (Service hydrographique de Canada, 2006). (Service Hydrographique de Canada, 2006).

En revanche, les limites des sondeurs acoustiques sont les suivantes :

- Les mesures de profondeur par sondeur acoustique nécessitent le déploiement d'un navire hydrographique qui n'est pas capable de mesurer dans l'eau très peu profonde (< 10m) surtout dans les zones côtières et les rivières (Wirth et Bruggeman, 2011 ; Hell, 2011). Ce problème provoque une limitation de couverture et une insuffisance de données.
- La précision bathymétrique au cours du sondage est de l'ordre de 15 cm lorsque tous les composants d'erreur sont inclus (température de l'eau, et les changements de salinité, déplacement du bateau) (Ferrari et Collins, 2006).

2.2.3. Techniques actives : Radar GPR (Ground Penetrating Radar)

Le Ground Penetrating RADAR (GPR) utilise les basses fréquences de 60 à 300 MHz comparativement au radars. Ce système transmet des ondes électromagnétiques de courtes impulsions à partir d'une antenne. Ces ondes sont absorbées et réfléchies par la cible. L'écho réfléchi est reçu et enregistré par l'antenne. La technique GPR a d'abord été développé pour des études géologiques, et son utilisation a ensuite été étendue à des études hydrogéologiques et hydrologiques. Les GPRs ont également été utilisés pour mesurer les profondeurs des lacs ou des rivières, soit lorsque leur surface est gelée ou en cas d'inondation. Les échos de surface et du fond de l'eau peuvent être enregistrées afin de mesurer la profondeur de l'eau.

La méthode GPR monté sur un filin ou depuis un hélicoptère a été expérimentée par l'U.S. Geological Survey (USGS) pour (i) déterminer la bathymétrie sur la rivière Cowlitz River (Etats Unis, Washington) (Spicer et al., 1997), (ii) déterminer la bathymétrie d'une rivière et d'un lac dans le Connecticut (États-Unis) et (iii) pour réaliser le profil du lit d'un lac en Arizona (Beres and Haeni, 1991). Sur l'ensemble de ces expérimentations, les précisions de mesures trouvées sont de l'ordre de 10 cm.

Le principal facteur limitant la pénétration du GPR dans l'eau est la turbidité de l'eau et l'atténuation de l'onde électromagnétique dans la colonne d'eau (Beres and Haeni, 1991). Cette technique est donc surtout adaptée aux faibles profondeurs entre 1 et 20m (Spicer et al., 1997).

2.2.4. Techniques actives : LiDAR Bathymétrique Aéroporté (ALB)

Le LiDAR bathymétrique émet une impulsion laser avec une longueur d'onde qui doit être capable de pénétrer l'eau jusqu'au fond. La longueur d'onde utilisée pour les LiDAR altimétriques se situe dans l'infrarouge qui ne pénètre l'eau que de quelques centimètres. Pour les applications bathymétriques, il est nécessaire d'utiliser des longueurs d'onde capables de traverser la colonne d'eau pour atteindre le fond. La longueur d'onde la plus appropriée est celle du vert (532 nm) car cette longueur d'onde pénètre le mieux l'eau avec un minimum d'atténuation (Guenther et al., 2000) tout en restant réalisable à partir d'un laser Nd-Yag (grenat d'yttrium aluminium dopé au néodyme). Lorsque l'impulsion émise atteint la surface de l'eau, une partie du signal vert est réfléchie par la surface et l'autre pénètre dans l'eau. Dans la colonne d'eau, le signal va s'atténuer exponentiellement du fait de l'absorption et la diffusion. Une fois l'impulsion reçue par le fond de l'eau, elle est réfléchie et traverse à nouveau la colonne d'eau et la surface de l'eau. Enfin, la détection du signal LIDAR réfléchi s'effectue avec un télescope équipé de photo-détecteurs et suivant un certain champ de vue (FOV~Field Of View). (Tulldahl and Steinvall, 1999).

Les principaux avantages offerts par le LiDAR bathymétrique sont :

- sa capacité à cartographier rapidement de grandes zones
- la densité spatiale des mesures
- la possibilité de sonder des zones dangereuses ou inaccessibles par voie maritime
- la rapidité de mise en œuvre du système de sondage.

Actuellement, quatre systèmes LiDAR bathymétriques existent dont les principales caractéristiques sont données en table 1 :

- le système SHOALS 3000T (Scanner Hydrographic Operational Airborne Lidar Survey) de la société Optech, initié dés 1993 (Hilldale and Raff, 2007),

- le système HAWK EYE II (Laser Bathymetry and Topography System, LBTS) qui été développé depuis 2004 par la société SAAB puis Airborne Hydro (Tuldahl et Steinvall, 2004),
- le système EAARL (Experimental Advanced Airborne Research LiDAR) qui a été développé par la NASA et l'USGS et est opérationnel depuis 2001 (Kinzel et al., 2007),
- le système (LADS Laser Airborne Depth Sounder) qui a été développé en 1977 par l'organisation Australienne de défense pour la science et la technologie (DSTO) (Cunningham et Lillycrop, 1998).

Système LiDAR	**SHOALS**	**EAARL**	**HawkEye**	**LADS**
Fabricant	Optech	NASA	Saab	DSTO
Altitude de vol	200 - 400 m	300 m	400 m	400 - 730 m
Angle d'incidence	0 - 40°	0 - 40°	0 - 40°	15 - 20°
Taille de spot au sol	240 cm	15 cm	40 cm	--
Précision verticale	15 cm	15 cm	25 cm	5 cm
Précision horizontale	5 m	1 m	5 m	5 m
Profondeur d'eau maximale atteinte	60 m	25 m	40 - 70m	50 - 80 m
Fréquence des impulsions	400 Hz	1000 Hz	200 Hz	900 Hz
Energie laser vert (532 nm)	5 mJ	0,7 mJ	5 mJ	5 mJ

Table 1 : Caractéristiques des systèmes LiDAR bathymétriques aéroportés (Baltavias, 1999; Chaponniere, 2004)

Les limites des systèmes LiDAR bathymétriques aéroportés ont pour principale limitation mentionnée dans la littérature, la turbidité de l'eau, limite les profondeurs maximales atteignables à la mesure, de l'ordre de 3 fois la profondeur de Secchi (Guenther, 2000). Ces limites sont également liées aux possibilités d''accroitre les puissances laser et les quantités d'énergie reçue au sol du fait de la législation sur la sécurité oculaire (ICNIRP, 2000 ; IEC 2001).

Les données acquises actuellement par les capteurs LiDAR bathymétriques aéroportés ne couvrent pas tous les milieux aquatiques. Suivant une vitesse de vol comprise entre 50 et 120 m/s, il est inenvisageable de couvrir tous les milieux aquatiques de la terre en contrairement aux capteurs satellitaires dont la trace au sol a une vitesse de l'ordre de 7000 m/s.

Le LiDAR est, en comparaison de l'imagerie hyperspecvtrale, moins dépendant de l'éclairage solaire et du bruit atmosphérique. La détection hyperspectrale est cependant reconnue comme performante pour la cartographie bathymétrique des eaux peu profondes du littoral, jusqu'à 20 m de profondeur (Jing et Datt, 2010; Kanno et Tannaka, 2012). Avec une profondeur typique jusqu'à 20 m, l'imagerie hyperspectrale a une capacité de détection beaucoup plus faible que le LiDAR (pénétration à 70 m) (Gao et al., 2009). Par ailleurs, le LiDAR bathymétrique est d'ores et déjà utilisé de manière opérationnelle pour la cartographie marine, tandis que l'imagerie hyperspectrale n'a pas encore atteint le même niveau de maturité. Les résultats en termes de précision ne répondant pas aux normes de la communauté hydrographiques (Bissett, 2005 ; Jay et al., 2012).

	Imageur passif	Radar GPR	Sonar	Lidar aéroporté
Opérationnalité	Instrument simple mais processing complexe et nécessitant des données de calibration	Nécessite l'installation d'un câble suspendu ou survol hélicoptère proche de la surface estime profondeur et vitesse	Navigabilité avec une profondeur d'eau > 5m	Système complexe en traitement de données
Résolution spatiale	Très haute densité spatiale (de 1 à 4 m pour des capteurs a haute résolution) (Liew et al., 2011)	- Spot de 0.5 m - 1000 impulsions/seconde (Beres and Haeni, 1991)	Faible couverture mais haute densité spatiale ((1000 sondes/seconde) (Lurton, 1998)	- Spot de 1 à 5 m - Densité de 200 à 1000 impulsions/seconde (Baltavias, 1999)
Résolution temporelle	Bonne répétitivité temporelle (tous les 3 jours pour des capteurs a haute résolution)	Digitalisation temporelle de quelques ns (Beres and Haeni, 1991)	Digitalisation temporelle d'une dizaine de microsecondes (Bisquay, 1999)	Digitalisation temporelle de 1 ns
Gamme de profondeur	Pénétration à 30 m en eau pure. 1 profondeur de Secchi (Feurer et al., 2008; Jay et al., 2012)	Adapté aux faibles profondeurs (1 à 20m) (Spicer et al., 1997)	Pénétration à 200 m (kenny et al., 2003)	Pénétration entre 25 et 80 m (eau pure). 3 profondeurs de Secchi (Guenther et al., 2000)
Précision	10 - 30 cm	10 - 20 cm	15 cm	5 - 25 cm

Table 2: Synthèse sur les techniques bathymétriques.

Aucune des solutions actuellement disponibles n'est totalement satisfaisante que ce soit pour les raisons de couverture horizontale ou verticale, ou pour des raisons de précision. En première approche, le lidar bathymétrique spatial apporte une haute résolution spatiale (spot < 10 m) associée à une bonne précision et une couverture systématique.

3. Objectif et Plan de la thèse

L'objectif de cette thèse est d'évaluer le potentiel des futurs capteurs LiDAR satellitaires pour estimer l'altimétrie et la bathymétrie des eaux de surfaces continentales et côtières.

Un tel objectif peut être atteint suivant une approche essentiellement expérimentale ou une approche plus théorique basée sur de la simulation de données LiDAR. Pour explorer les performances des signaux LiDAR sur une gamme variée et contrôlée de milieux, seule une approche par simulation est raisonnablement envisageable. Pour autant, confronter les quelques données expérimentales disponibles au simulateur est une étape indispensable à l'extrapolation de celui-ci. Dans ce cadre, cette thèse a pour objectifs spécifiques :

- évaluation de la qualité des données de lidar spatial
- de proposer un modèle et un outil de simulation de trains d'ondes LiDAR pour différentes configurations de capteurs (longueurs d'onde) et pour différents types de milieu-cible et de valider ce simulateur sur des mesures existantes
- d'explorer les performances bathymétriques et altimétriques d'actuels et futurs capteurs LiDAR spatiaux sur les eaux continentales et côtières à partir de signaux observés ou simulés afin de donner une estimation du domaine de fonctionnement d'un instrument spatial.

Dans le premier chapitre de ce mémoire, nous avons évalué la qualité des données altimétriques du capteur satellitaire GLAS/ICESAT pour le suivi des plans d'eau. La méthode consiste en une comparaison de l'élévation GLAS/ICESAT avec les niveaux d'eau mesurés aux stations hydrométriques. Cette étude s'articule en deux articles. Le premier article a étudié la pertinence des données d'élévation GLAS/ICESat sur le lac Léman et les cours d'eaux en France a été publié dans la

revue Remote Sensing: « The relevance of GLAS/ICESat élévation data for the monitoring of river networks ». Le deuxième article a analysé la précision altimétrique du capteur GLAS/ICESat sur les grands lacs américains. Cet article a été publié dans le journal ISPRS (International Society for Photogrammetry and Remote Sensing): “Improving the assessment of ICESat water altimetry accuracy accounting for autocorrelation”.

Dans le premier article, la réponse de GLAS/ICESat lors de la transition terre-eau est analysée. Ensuite la précision altimétrique est évaluée sur le lac Léman. Enfin, la qualité des mesures ICESat est étudiée sur les rivières en France. Dans le deuxième article, appliqué aux grands lacs américains, la méthode d'évaluation de la précision GLAS tient compte de l'autocorrélation temporelle des mesures ICESat. Elle prend également en considération les incertitudes des données de références issues des stations hydrométriques sur les lacs. Un processus de mise à l'échelle probabiliste a été développé. Ce processus est basé sur les shots (tir laser) successifs d'une trace en tenant compte de l'autocorrélation entre les shots successifs.

Dans le deuxième chapitre, un modèle de signaux LiDAR a été développé afin de simuler des formes d'ondes LIDAR mesurées pour différents paramètres instrumentaux (longueur d'onde laser, puissance émise, largeur de pulse...) et pour une collection représentative et simplifiée de paysages ‘cibles’ de surfaces immergées. La validation du modèle a été effectuée par comparaison de trains d’ondes GLAS/ICESat observés sur le lac Léman et à partir de trains d’ondes observés par le capteur HawkEye II sur une zone côtière au nord de la Réunion (données SHOM). Elle a également été validée par comparaison aux résultats de simulations réalisées par EADS-Astrium. Cette étude a été présentée dans un article sous presse dans le journal IEEE Geosciences and Remote Sensing Letters intitulé « Wa-LiD: A new LiDAR simulator for waters »

A ce jour, le seul capteur LiDAR satellitaire en mission, GLAS/ICESat, n’est pas adapté à la bathymétrie du fait de sa longueur d’onde dans l’infrarouge (1064 nm) qui ne permet pas une pénétration dans l’eau et de sa longueur d'onde dans le vert dédiée seulement pour mesurer la distribution verticale des nuages et des aérosols. Par conséquence, des configurations instrumentales de futures missions bathymétriques pour des LiDAR satellitaires doivent être explorées afin de répondre aux questions suivantes: quel est le pourcentage de surfaces immergées qui peuvent

être mesurées par un satellite LIDAR bathymétrique et suivant quelle précision de mesure ? Et dans quelle mesure ces résultats dépendent-ils des paramètres du système LiDAR et des paramètres de l'eau ? Et est-ce que les résultats dépendent des paysages cibles (eaux côtières, eaux continentales) ? Le troisième chapitre tente de répondre à ces questions. La performance bathymétrique des futurs capteurs LiDAR spatiaux est explorée sur les eaux côtières, les rivières, les lacs profonds et les lacs peu profonds. Les performances de deux configurations capteurs émettant dans l'UV (355 nm) ou dans le vert (532 nm) ont été évaluées à partir d'une méthodologie basée sur la simulation de trains d'onde. Une base de données de trains d'onde simulées a été construite à partir du simulateur Wa-LiD en tenant compte des distributions des différents paramètres de l'eau issues de la littérature et présumées être représentative à l'échelle mondiale pour plusieurs types d'eaux. Une analyse de sensibilité est appliquée pour identifier les paramètres environnementaux qui ont une forte influence sur l'écho de fond de l'eau. Ensuite, les probabilités de détection de fond de l'eau sont calculées pour les deux configurations LiDAR et pour les quatre types d'eau. Enfin, après avoir utilisé des fonctions mathématiques adaptées pour approximer les différentes contributions du signal LiDAR (surface, colonne et fond), la précision sur l'estimation de la bathymétrie est estimée pour les signaux permettant la détection du fond de l'eau en se limitant aux erreurs introduite par la seule inversion des trains d'onde. Les résultats de cette étude ont été acceptés (Juillet 2012) pour la publication au journal IEEE JSTARS (Journal of Selected Topics in Applied Earth Observation and Remote Sensing) intitulé « Potential of space-borne LiDAR sensors for global bathymetry in coastal and inland waters ».

Pour finir, des conclusions sur le travail effectué, ses limites et ses perspectives sont données dans le dernier chapitre, ainsi qu'une synthèse des résultats obtenus qui ouvre des pistes pour des développements futurs dans le domaine des capteurs LiDAR satellitaires pour des applications bathymétriques.

Chapitre 1

Évaluation de la qualité des données altimétriques LiDAR satellitaires sur les eaux continentales

Chapitre 1

1. Évaluation de la qualité des données altimétriques LiDAR satellitaires sur les eaux continentales

Depuis la mise en orbite de satellites altimètres RADAR, l'altimétrie spatiale est présentée comme une alternative aux stations limnimétriques de terrain pour le suivi des eaux continentales. L'altimétrie spatiale LiDAR depuis la mise en orbite du satellite lidar GLAS/ICESat-1 (2003-2009), est elle-même pressentie comme une technique d'altimétrie qui permettrait, par la résolution spatiale qu'offre cette technologie, de suivre un ensemble de masses d'eau et cours d'eau beaucoup plus important.

Dans le premier papier, nous avons étudié la pertinence des données altimétriques du capteur GLAS sur le lac Léman et les cours d'eaux en France. Nous nous sommes d'abord intéressés à la précision des données GLAS sur le lac Léman par comparaison des données satellitaires aux données de références mesurées par des stations limnimétriques au sol. Deux stations limnimétriques (Chillon et Saint Prex) ont été utilisées pour évaluer la précision des altitudes des données GLAS.

L'analyse des formes d'onde GLAS a montré un phénomène de saturation qui se produit lorsque le milieu passe d'un milieu faiblement à fortement réfléchissant. Les surfaces en eau peuvent avoir un caractère spéculaire et peuvent être fortement réfléchissantes lorsque la visée du capteur est au nadir. Les altitudes calculées à partir des formes d'onde saturées sont imprécises. Une correction de la saturation est disponible sur les produits de données GLAS. La correction de l'effet de saturation améliore nettement la qualité des estimations du niveau de l'eau. La RMSE sur les altitudes est de 33 cm sans la correction de saturation puis de 14 cm après correction.

Lors de la transition terre-eau, les premières mesures GLAS donnent des altitudes (niveaux d'eau) surestimées de 30 a 150 cm. Une analyse des profils temporels de mesures de niveaux GLAS montre qu'un temps de 0.25 s (soit 8 mesures ou 1,36 km) est nécessaire pour que le gain s'ajuste, limite l'effet de saturation des trains d'onde et annule la surestimation des niveaux. Une fois les mesures en phase de

transition éliminées, la précision sur les niveaux d'eau estimés est d'environ 5 cm. Cette étude montre, du fait des problèmes de transition entre milieu reflétant et peu reflétant (eau/terre), que les masses d'eau étroites (rivières, petits lacs) peuvent difficilement faire l'objet d'une surveillance satellitaire par un capteur de type ICESAT/GLAS (gain adaptatif).

Dans un deuxième temps et pour corroborer le résultat précédent, la précision des données altimétriques GLAS a été évaluée sur le réseau hydrographique français qui présente des cours d'eau moyens à larges jusqu'à quelques centaines de mètres. Seules les données GLAS du laser 3 ont été exploitées puisque la taille du spot de ce laser est de 55 m environ contre 90 m pour le laser 2 et 149 m pour le laser 1. Les spots retenus sont ceux qui ont une intersection avec les rivières d'une largeur supérieure à 50 m, situés dans un rayon de 1 km d'une station hydrologique du réseau de la Banque Hydro Nationale, et éloignés d'un ouvrage particulier (ouvrage de franchissement, retenue, etc). Ainsi, seules 26 traces GLAS et 46 spots ont été sélectionnés pour la comparaison avec des mesures terrain. La RMSE estimée est d'environ 1,15 m. Plusieurs sources d'erreur participent au budget d'erreur : erreur de nivellement des stations, erreur lié à la pente des cours d'eau ou perturbation de la ligne d'eau par présence d'ouvrages intermédiaires, déversoirs, erreur liée aux effets de berge, et surtout l'effet de non correction de la saturation du signal lors des transitions terre-eau évoqué précédemment.

Dans le deuxième papier, nous avons porté un autre regard sur la qualité des données GLAS pour l'altimétrie des surfaces en eau continentales en s'intéressant aux effets et méthodes de moyennage de mesures individuelles (spot) à l'échelle des masses d'eau. Pour ce faire, nous avons analysé la précision altimétrique des données GLAS/ICESat sur les grands lacs américains. Habituellement, on compare la moyenne arithmétique des shots individuels d'une trace sur un plan d'eau à un niveau moyen du lac (Birkett, 1998; Bercher 2008). Les shots individuels sont considérés comme indépendants. Il y a nécessité de vérifier la dépendance temporelle (autocorrélation) entre les shots successifs d'une trace et son effet sur les statistiques de l'erreur de mesure.

La méthode d'évaluation de la précision GLAS s'attache à prendre en compte les effets d'autocorrélation temporelle entre mesures GLAS/ICESat le long de la trace.

Elle prend également en considération les incertitudes des données de références issues des stations limnimétriques sur les lacs et de leur nivellement.

L'autocorrélation entre les spots successifs a été analysée, testée puis modélisée pour chacune des traces ICESat suivant un variogramme. En cas d'autocorrélation significative pour une trace donnée, un processus de krigeage par bloc a été utilisé pour estimer une élévation moyenne de l'eau et son incertitude associée à l'échelle de la trace. Enfin, les distributions des écarts entre mesures des stations limnimétriques et les mesures par GLAS/ICESAT ainsi ont été estimées aux échelles des traces ou des lacs. De ces distributions, les statistiques usuelles métrologiques (biais et écart type d'erreur aléatoire) ont été proposées.

Un ensemble de 237 traces GLAS à proximité des stations hydrométriques pour quatre des Grands Lacs du Nord d'Amérique a été analysée (Superior, Michigan, Erie and Ontario). Une autocorrélation significative entre les valeurs successives des shots a été observée pour 45% des traces. En moyenne, la prise en compte de l'autocorrélation dans l'incertitude des niveaux moyen des lacs donne une incertitude du niveau moyen 8 fois supérieure à ce qu'elle serait sans en tenir compte. Cette autocorrélation à une portée moyenne de 11 shots consécutifs. Une analyse de la présence de cette autocorrélation montre qu'elle pourrait statistiquement être liée à une faible énergie transmise par le capteur GLAS/ICESat et de mauvaises conditions météorologiques. Un biais global de 4,6 cm (sous-estimation de l’élévation par GLAS) et un écart type global de 11,6 cm ont été estimés. Au delà des statistiques sur la qualité des estimations de niveaux de lacs par agrégation de données GLAS/ICESat, les résultats ont démontré la pertinence de prendre en compte l'autocorrélation dans l'évaluation de l'incertitude des données satellitaires.

1.1. The relevance of GLAS/ICESat elevation data for the monitoring of river networks

- Baghdadi N., Lemarquand N., **Abdallah H.,** Bailly J.S., 2011. The relevance of GLAS/ICESat elevation data for the monitoring of river networks. Remote Sensing, 3 (4), 708-720.

The Relevance of GLAS/ICESat Elevation Data for the Monitoring of River Networks

Nicolas Baghdadi [1,*], Nicolas Lemarquand [1], Hani Abdallah [1] and Jean Stéphane Bailly [2]

[1] CEMAGREF, UMR TETIS, 500 rue François Breton, 34093 Montpellier cedex 5, France; E-Mails: nicolas.lemarquand@teledetection.fr (N.L.); hani.abdallah@teledetection.fr (H.A.)

[2] AgroParisTech, UMR TETIS, 500 rue François Breton, 34093 Montpellier cedex 5, France; E-Mail: jean-stephane.bailly@teledetection.fr

* Author to whom correspondence should be addressed; E-Mail: nicolas.baghdadi@teledetection.fr; Tel.: +33-4-67-548-724; Fax: +33-4-67-548-700.

Received: 25 January 2011; in revised form: 23 March 2011 / Accepted: 29 March 2011 / Published: 6 April 2011

Abstract: The Ice, Cloud and Land Elevation Satellite (ICESat) laser altimetry mission from 2003 to 2008 provided an important dataset for elevation measurements. The quality of GLAS/ICESat (Geoscience Laser Altimeter System) data was investigated for Lake Leman in Switzerland and France by comparing laser data to hydrological gauge water levels. The correction of GLAS/ICESat waveform saturation successfully improved the quality of water elevation data. First, the ICESat elevations and waveforms corresponding to water footprints across the transition from the land to water were analyzed. Water elevations (2 to 10 measurements) following the land-water transition are often of lesser quality. The computed accuracy for the ICESat elevation measurements is approximately 5 cm, excluding transitions footprints, and 15 cm, including these footprints. Second, the accuracy of ICESat elevation was studied using data acquired on French rivers with a width greater than the size of the ICESat footprint. The obtained root mean square error (RMSE) for ICESat elevations in regard to French rivers was 1.14 m (bias = 0.07 m; standard deviation = 1.15 m), which indicates that small rivers could not be monitored using ICESat with acceptable accuracy due to land-water transition sensor inertia.

Keywords: lidar; ICESat; rivers; lakes; elevation

---

1. Introduction

Freshwater provisioning will be a major problem in future decades. Currently, 1 billion people depend on lakes for domestic water consumption, which will expand to 5.5 billion in 30 years [1]. Monitoring of continental water resource, particularly lakes and rivers, is necessary because many global regions lack sufficient water for domestic consumption, agriculture, and other uses. Hydrologic networks that are generally organized on a national basis provide monitoring of water resource. These networks measure the temporal variations in the water level of rivers, lakes and reservoirs. However, the spatial distribution of hydrological gauges is insufficient in some parts of the world due to freshwater needs. Moreover, a reduction in the number of stations has been observed in conjunction with a decline in the quality of measurements. A better understanding of the global water cycle and the impact of climate change requires a thorough knowledge of water resources on the continental surface. Therefore, there is a real demand for a global, homogeneous, perennial monitoring system of continental water.

Optical and Synthetic Aperture Radar (SAR) imageries (e.g., LANDSAT, NOAA, MODIS, SPOT, ASTER, ERS, ASAR, RADARSAT, and PALSAR/ALOS) are often used to map the extent of water areas [2,3]. Determination of changes in the associated water level is estimated using radar altimeters and lidar systems [4-6]. The radar altimetry missions demonstrated the potential of continental water observation with three principal advantages suitable to hydrological observations: all-weather operability, global data coverage, and temporal repetivity (10 days for Jason and Topex and 35 days for ENVISAT and ERS). The radar altimeters used for Topex/Poseidon, ERS-2, ENVISAT, and Jason-1/2 have a coarse spatial resolution “footprint size” (a few hundred meters to few kilometers), which means they can monitor only large lakes, rivers, and reservoirs. Typically, altimetric measurements can range in accuracy from a few centimeters (e.g., Great Lakes, USA) [7,8] to tens of centimeters (e.g., Lake Chad, Africa) [8]. Accuracies of 5 cm RMS for Lake Issykkul (Kirgyzstan) and 10 cm RMS for Lake Chardarya (Kazakhstan) were previously determined by Créteaux and Birkett [9]. In all of these studies, the obtained accuracies are directly related to the size of the body of water because the satellite measurement compared to ground reality is usually obtained by averaging individual shot measurement along tracks. Therefore, rivers appear more difficult to study because of their width. The first studies relating to rivers were performed in the Amazonian basin, which contains very large rivers. In studies by Birkett *et al.* [5], RMSE (Root Mean Square Error) values between hydrologic gauges and Topex/Poseidon data for a selection of rivers and floodplains in the Amazon Basin exhibited high variability, with an overall mean of approximately 1.1 m RMS and optimal values of approximately 40 cm. The accuracy for rivers is highly variable, being that these measurements are dependent on the target width.

Satellite laser altimetry, such as the Geoscience Laser Altimeter System (GLAS) on the Ice, Cloud, and Land Elevation Satellite (ICESat), provides elevation data that are very useful to many applications and offer the potential to monitor small water areas due to small associated footprints (50 to 90 m). NASA launched the ICESat satellite in January 2003 [10,11]. ICESat includes two laser altimeters operating at visible (green, 532 nm) and near-infrared (1,064 nm) wavelengths, and each near-infrared laser footprint along the satellite track is 172 m apart, with 40 points (shots) per second (40 Hz). The horizontal geolocation accuracy of the ICESat footprints is 3.7 m. The waveform of each shot is

sampled in 544 or 1,000 bins over land area at a temporal resolution of 1 ns. The vertical resolution of land waveforms is 15 cm. The nominal pointing angle of ICESat is approximately 0.3 ° off nadir, with a potential of up to 5 °. The high pointing angles reduce the specular reflection on waters, and therefore, the waveform saturation will increase the elevation error [12]. However, GLAS laser altimeter cannot be used for routine monitoring because only some tracks are possible with ICESat due to power safety and meteorological conditions, which is in contrast to radar altimeters where study sites are revisited every 10 days.

Chipman and Lillesand [13] assessed the accuracy of the ICESat GLAS laser altimeter on the Toshka lakes west of Lake Nasser in southern Egypt. The standard deviation of GLAS elevation measurements along a single transect was on the order of 3–8 cm. Bhang *et al.* [14] have demonstrated a difference between GLAS elevation and gauging stations between 2 and 35 cm for lakes in Otter Tail County, Minnesota (USA). Other studies have demonstrated that the accuracy of ICESat is greater than 10 cm, compared to gauge data [12,15,16]. However, the quality of ICESat data for rivers has not been thoroughly investigated. Analysis of ICESat measurements (transect of 50 km with 300 footprints/shots) along the Tapajos River, Brazil, provides a RMSE of approximately 3 cm for clear meteorological conditions, 8 to 15 cm for partly cloudy skies, and 25 cm for heavy clouds [12]. These studies are indicative of the performance of ICESat for large-size targets, with high spatial coverage. The accuracy of lidar measurements should be degraded for small targets, with only some measurements by track, as in Birkett *et al.* [5], where a factor of ten was observed with radar altimetry between RMSE obtained from rivers and floodplains. Could the elevation of rivers and lakes that span several hundreds of meters be measured with good accuracy (approximately 10 cm) using ICESat (footprints of 50–90 m)?

Moreover, the number of measurements excluded from each ICESat transect corresponding to footprints with possible disturbances related to the land-water transition is never specified. However, the value of this margin will limit the size of targets that could be analyzed by laser systems, such as ICESat.

The response of GLAS/ICESat to the land-water transition was first analyzed. The accuracy of ICESat for Lake Leman (a flat surface) was then evaluated. Finally, the potential use of ICESat measurements for rivers in France (small targets) was studied.

2. Lake Leman

2.1. Description of Study Site and Dataset

Study Site

The accuracy of ICESat measurements was evaluated across Lake Leman located in Switzerland and France (Lat. 46 °26′N and Long. 6 °33′E). This is one the largest lakes in Western Europe with a surface of 582 km^2. The average level of water is 372 m, which is controlled by the Seujet Dam near Geneva. The maximum length and width of the lake are 73 and 14 km, respectively.

Lake Leman is bordered on the south by the Haute-Savoie massif. The land-water transition in the ascending acquisition mode of ICESat involves a difference in elevation of 550 m for a distance of

5 km (south to north). In the area north of Lausanne, the land-water transition (north to south) in descending mode is softer with a difference in elevation of 260 m for a distance of 5 km.

Dataset

A total of 21 GLAS (Geoscience Laser Altimeter System) transects across Leman Lake were available for comparison with the lake gauge data (Figure 1). ICESat data were acquired between 2 March 2004 and 13 March 2008. The length of transects varied between 8.5 and 10.5 km, with a total number of 774 shots measured. The data used are comprised of GLA01 (waveform) and GLA14 (Land Surface Altimetry) products in the Release 31. The elevation of GLAS laser data was computed using tools developed by the US National Snow and Ice Data Center (NSIDC). Six transects corresponding to cloudy episodes were next excluded from the dataset because the corresponding elevations were strongly disturbed (heights of approximately 3,500 m).

Figure 1. The Ice, Cloud and Land Elevation Satellite (ICESat) tracks through Lake Leman. **(a)** Ascending mode and **(b)** descending mode.

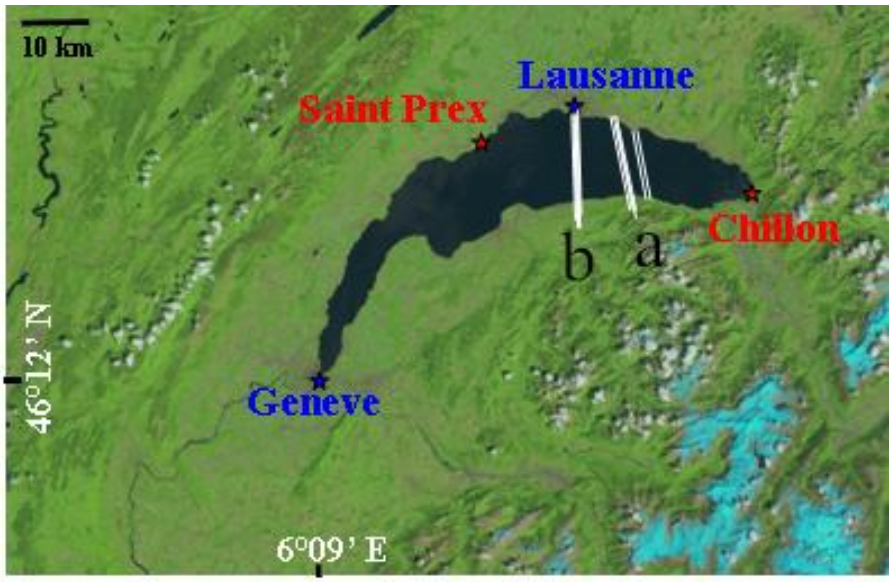

Two hydrological stations, Chillon and Saint Prex (Figure 1), were used to evaluate the accuracy of ICESat elevations. As the difference in water level between the two stations is relatively weak (~1 cm), an average elevation was used. The Swiss Federal Office for the Environment (FOEN) [17] measures water levels at permanent gauging stations for Swiss bodies of water. The water levels of hydrological stations are given in the Swiss height measurement reference system. The reference for all height measurements in Switzerland is the "Repère Pierre du Niton" in the harbor of Geneva (stone). The height of this stone was evaluated in 1902 to be 373.6 m over sea level.

All heights refer to the same vertical datum to conduct a consistent comparison among the two height data sets. In this study, the data comparison was performed in terms of orthometric heights with respect to the WGS84 reference system and the EGM96 geoid model. ICESat elevations available to users correspond to ellipsoidal heights with reference to the Topex ellipsoid. The conversion of the Topex ellipsoid to the WGS84 ellipsoid was approximated by $h_{WGS84} = h_{Topex} - 70.7$ cm. Next,

ellipsoidal elevations (h_{WGS84}) were converted into orthometric elevations (H) by applying the EGM96 geoid value (N): $H = h_{WGS84} - N$.

Shots of water were then extracted individually track by track, and the mean elevation was calculated for each track. This mean was used for comparison with reference elevations (hydrological gauges).

2.2. Results

Analysis of ICESat waveforms demonstrated a saturation phenomenon, which must be corrected. Saturation occurs when the returned energy by a number of 1 ns bins is greater than the threshold function of gain [12,18]. Therefore, elevations calculated from saturated waveforms are incorrect. A saturation correction is available for the produced data and is recommended for use on calm waters because of the associated specular reflection. The correction value varies between 0 and 1.5 m and is added to the GLAS elevation. However, the correction is not available for some shots and the value "–999.00" is given instead (*i.e.*, elevation should be corrected, but the method used to calculate the correction coefficient cannot provide a correct value). Figure 2 shows some GLAS waveforms obtained for Lake Leman in the case of water only. For the saturated waveforms (calm water), the high level of reflected energy involves a clipping of the maximum peak, which shifts this peak several bins to the left. The derived GLAS elevation is thus underestimated.

Figure 3 shows the ICESat elevations across Lake Leman for the 3 June 2005 transect. This example shows the importance of the saturation effect (errors reach 1.41 m) and demonstrates the need to include the saturation correction.

Figure 2. Typical Geoscience Laser Altimeter System (GLAS) waveforms on Lake Leman (water only). (**a**) Unsaturated waveform, (**b**) waveform slightly saturated, and (**c**, **d**) waveforms with high saturation. These examples are extracted from the 03 June 2005 transect. The reference elevation is 372.18 m. Ordinate = energy in volts and abscissa = bin number (bin spacing = 1 ns).

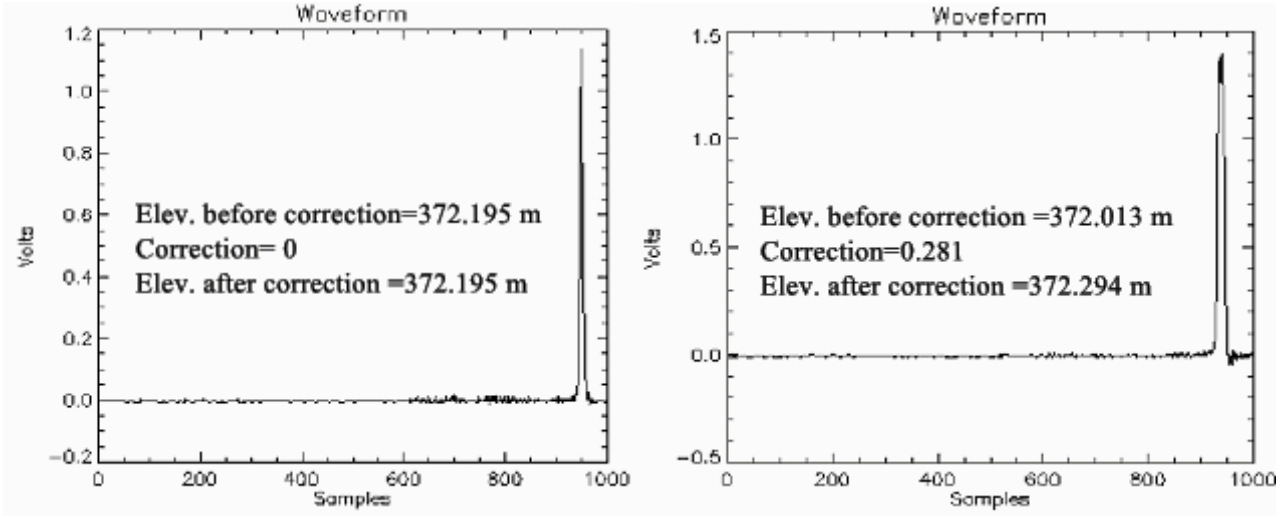

(a) **(b)**

Figure 2. *Cont.*

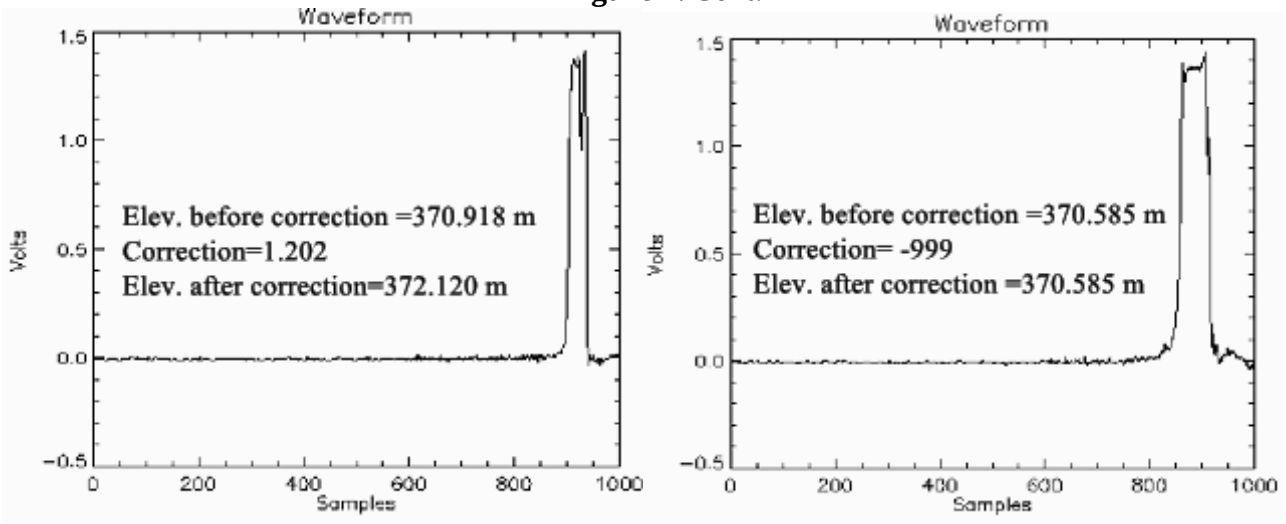

(c) **(d)**

Figure 3. ICESat elevations across Lake Leman extracted from the 3 June 2005 transect. The reference elevation is 372.18 m. Ordinate = energy in volts and abscissa = bin number (bin spacing = 1 ns).

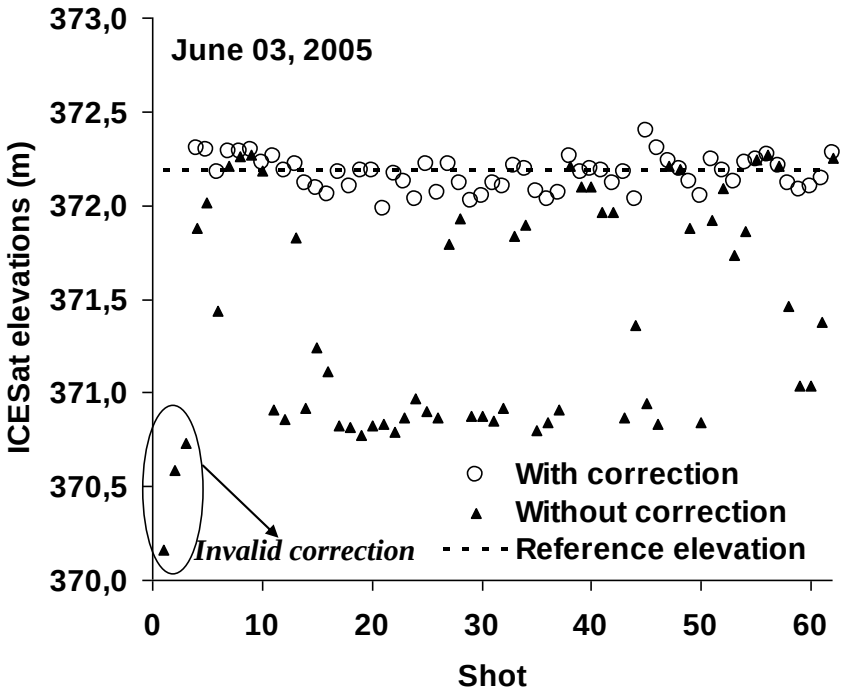

Analysis of ICESat transects across the lake demonstrates that the shots from the land to water could be divided into four categories:

- Category 1: Shots corresponding to land. The saturation correction is valid (between 0 and 1.50 m).
- Category 2: Three to eight shots correspond to "land", "land+water" or "water" with invalid correction.
- Category 3: Two to ten shots correspond to "water" with valid correction, but not adapted (called transition shots).

- Category 4: ICESat shots corresponding to “water” with estimated elevations close to reference elevations. The saturation correction is valid and well adapted.

On the passage of ICESat from land to water, the first laser waveforms corresponding to water exhibit a strong saturation. The elevation of theses shots systematically exhibit a significant variation compared to the reference elevation (Figure 4). Indeed, GLAS elevations of water surfaces without saturation correction are lower than reference elevations from −40 to −90 cm (maximum values). With correction of the saturation effect, elevations are higher than reference elevations from +20 to +50 cm (maximum). The highly saturated elevations without available correction (−999.00) are lower than the reference elevation of approximately one meter (Figure 4(b)). This saturation phenomenon which affects 2 to 10 spots is more important in ascending mode than in descending mode. The instrumental parameters are not different in ascending and descending modes. Shots following the first saturated waveforms provide elevations very close to the reference elevation with weak fluctuations. However, the analysis of the terrain geometry shows that the transition land-lake in ascending mode is very different from the transition land-lake in descending mode. In the South, when the Haute-Savoie massif is thrown into the lake, the transition land-lake in ascending mode is brutal with uneven of 550 m on a distance of 5 km. Conversely, in the Lausanne area in North, the transition land-lake in descending mode is softer with uneven of 260 m on 5 km. The difference in the observations between ascending and descending transects could be related to the laser beam target reflectivity.

Saturation is due to specular reflection of the water that saturates the detector, depending on laser beam target reflectivity. ICESat profiles demonstrate that a certain time is necessary for the gain control to compensate for electronic saturation by a reduction of gain. This could explain the progressive return to normal that can last for 10 measurements (maximum duration of 0.25 seconds and a maximum distance about 1.5 km). Moreover, the time necessary for desaturation of the detector depends on the ICESat pointing angle. Pointing angles larger than nominal will reduce the probability of waveform saturation but will increase the elevation error. The relationship between the pointing angle (θ) and the elevation error (ε) is given by $K.\alpha\ \theta$ [12], where K is a constant = 5cm/⁰⁄arcsecond and α is the pointing knowledge error in arcseconds. For our ICESat dataset, the pointing angle was close to 0.3 °(nominal value). For α for a fully-calibrated laser campaign is = 1.5 arcseconds (L3a laser campaign), the elevation error ε = 2.25 cm.

This slowness in adaptation of gain after the land-water transition phase seriously limits the ICESat for limnimetric monitoring of rivers. With the exception of great rivers, the detector has not enough time after each land-water transition to correctly adjust the saturation correction coefficient. With or without correction, the first estimates of ICESat elevations would have an altimetric error of several tens of centimeters.

The 19 March 2006, transect demonstrates successively the first shots of the transition slightly saturated (valid correction), oversaturated (not valid correction = −999.00), and then slightly saturated (valid correction) (Figure 4(b)). This alternation of “valid correction” and “not valid correction” is surprising. There can be a restitution error for the spot position on the ground related to pointing error. Alternatively, the laser direction can oscillate to approach nadir in certain cases resulting in saturation, whereas the pointing angle is sufficient to avoid saturation in other cases. This second scenario would explain the nonsystematic nature of the phenomenon.

Figure 4. Some examples of ICESat transects in comparison to reference elevation (gauges). Abscissa = shot number (spacing = 0.025 s) and ordinate = elevation (ICESat with/without saturation correction, and hydrological gauges).

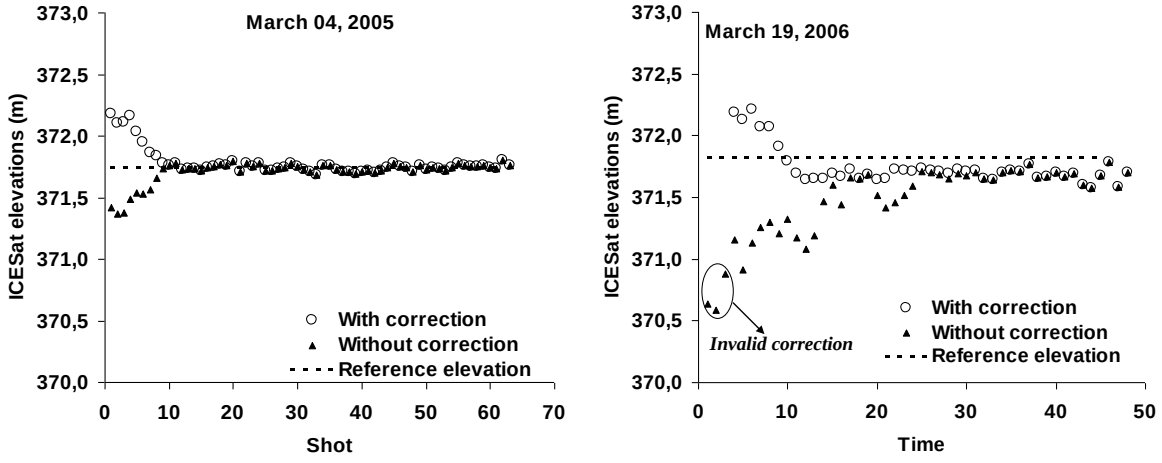

(a) *Descending mode*

(b) *Ascending mode*

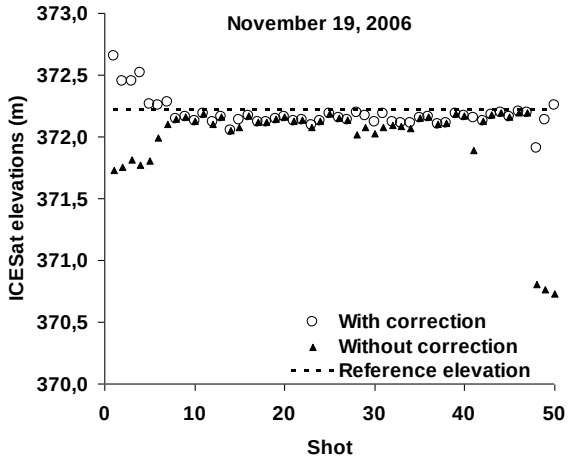

(c) *Ascending mode*

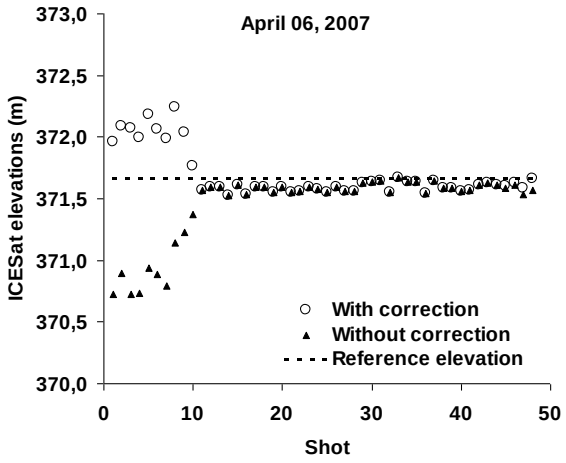

(d) *Ascending mode*

Table 1 summarizes the results of the comparison between GLAS elevations (GLA14 product) and lake level data recorded by hydrological stations. The mean lake height for each ICESat transect is determined from averages of all valid height measurements. The mean value difference between the ICESat and reference elevations varies from 0 to 1.09 m for GLAS data without the correction of saturation effect and from 0 to 22 cm for corrected data. The RMS error ranges from 5 cm to 1.19 m without correction and from 5 cm to 30 cm with correction (Table 1). For nine ICESat tracks, the RMSE is greater than 20 cm when the correction is not applied against 2 tracks (Table 1). The mean RMSE for all tracks is approximately 15 cm with the saturation correction and 5 cm excluding transition footprints (first saturated waveforms). The errors are higher when the saturation correction is not applied (33 cm). Transects acquired on 13 March 2008, and 6 April 2007, had high standard deviations in comparison to other transects, which could result from a lack of sufficient correction for atmospheric effects. For the 13 March 2008 transect, only 22 data were used in the accuracy

calculation. This result from implementing the saturation correction for continental waters corroborates the previous observations of Urban *et al.* [12].

Table 1. Comparison of Geoscience Laser Altimeter System (GLAS) and reference elevations (hydrological gauges) for Lake Leman. The eight dates marked by a star (*) have weak or null saturation corrections.

Date	Hydrological gauges	ICESAT Dataset	ICESat elevation (m) Without correction				ICESat elevation (m) With correction			
dd/mm/yy	Reference elevation (m)	Shot number	mean	std	RMSE	ICESat-Ref	mean	std	RMSE	ICESat-Ref
02/03/04 *	371.72	60	371.72	0.05	0.05	0.00	371.72	0.05	0.05	0.00
12/06/04 *	372.23	47	372.19	0.11	0.11	−0.04	372.24	0.12	0.12	0.01
04/03/05 *	371.74	61	371.78	0.11	0.12	0.04	371.71	0.09	0.09	−0.03
16/03/05	371.68	42	370.59	0.50	1.19	−1.09	371.77	0.16	0.18	0.09
03/06/05	372.18	61	371.49	0.59	0.90	−0.69	372.14	0.09	0.10	−0.04
15/11/05 *	372.25	49	371.99	0.10	0.27	−0.25	372.05	0.13	0.23	−0.19
19/03/06	371.82	43	371.53	0.22	0.36	−0.29	371.74	0.15	0.17	−0,08
07/06/06 *	372.17	63	372.24	0.07	0.10	0.07	372.26	0.08	0.12	0.09
18/06/06	372.26	45	372.19	0.21	0.22	−0.07	372.42	0.11	0.19	0.16
07/11/06 *	372.22	63	372.23	0.13	0.13	0.01	372.29	0.08	0.11	0.07
19/11/06	372.22	50	372.00	0.34	0.40	−0.22	372.18	0.12	0.13	−0.04
25/03/07 *	371.74	61	371.81	0.10	0.12	0.07	371.87	0.07	0.15	0.13
06/04/07	371.66	48	371.45	0.28	0.35	−0.21	371.69	0.19	0.19	0.03
16/10/07	372.21	59	372.02	0.24	0.30	−0.19	372.20	0.07	0.07	−0.01
13/03/08 *	371.53	22	371.31	0.21	0.30	−0.22	371.31	0.21	0.30	−0.22

3. Rivers of Metropolitan France

The accuracy of GLAS elevations was then studied using data acquired for French rivers wider than the size of ICESat footprint (Figure 5(a)). This comparison allows for analysis of the accuracy of GLAS measurements for rivers and to conclude on the use of ICESat for these small bodies of water. Only GLAS data from laser number 3 (campaign L3) were used because this area had the smallest major axis footprint size (approximately 55 m compared with 90 m for L2 and 149 m for L1), which is better adapted to the width of the French river. 10 ICESat data collection campaigns were used (L3A to L3J) (Table 2). All selected ICESat footprints had the following characteristics: (1) intersecting rivers with a width greater than 50 m, (2) radius of 1 km for gauge stations with a well referred limnimetric scale, and 3) distance far enough from hydraulic systems that can disrupt the water level within a small distance. Moreover, optical aerial photos were used to validate the selection of ICESat footprints. For this comparison, 26 ICESat tracks and 46 footprints were obtained (Figure 5(b)). This weak number for ICESat measurements illustrates the difficulty of monitoring small rivers with the ICESat configuration.

Assuming that measurements at gauge stations were of sufficient accuracy regardless of distance in time and space between GLAS shot and gauge station measurement, the elevation of each GLAS shot was then compared with the one from the closest hydrological station at the closest measured time. For

this latter point, the obtained mean deviation between the time of GLAS acquisitions and the stations was 1.8 hours with a standard deviation (std) of 2.25 hours.

Figure 5. (a) ICESat tracks (in gray) and French hydrographic network (in blue), **(b)** GLAS data used in this study (rivers width >50 m, far from any dam or other hydraulic plant, with distance between ICESat shot and hydrological stations <1,000 m).

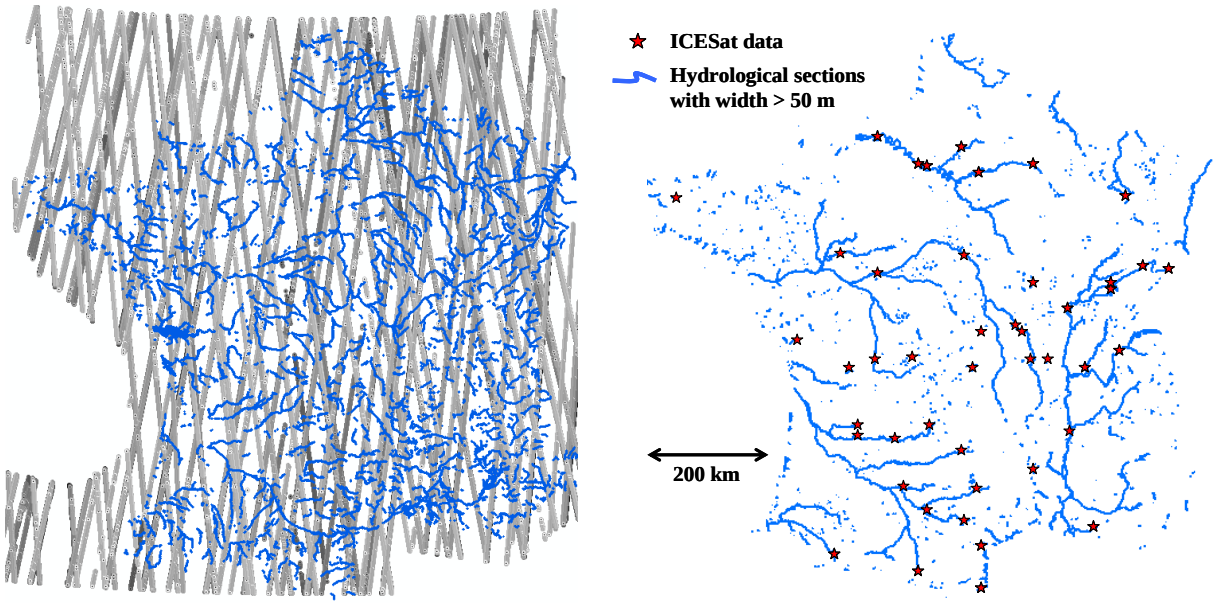

Table 2. Start date and End date of ICESat campaigns L3A to L3J.

Laser campaign	Start date (dd/mm/yyyy)	End date (dd/mm/yyyy)
L3A	10/03/2004	11/08/2004
L3B	02/17/2005	03/24/2005
L3C	05/20/2005	06/23/2005
L3D	10/21/2005	11/24/2005
L3E	02/22/2006	03/28/2006
L3F	05/24/2006	06/26/2006
L3G	10/25/2006	11/27/2006
L3H	03/12/2007	04/14/2007
L3I	10/02/2007	11/05/2007
L3J	02/17/2008	03/21/2008

The RMSE for GLAS elevations obtained on the French rivers is 1.14 m (bias = 0.07 m; std = 1.15 m; 46 footprints) (Figure 6). This corresponds to approximately 10 times the RMSE for wider bodies of water, such as Lake Leman. For concerned ICESat waveforms, 61% were saturated and the correction of this saturation was not possible (correction = −999,000). Moreover, the correction proposed for the first water shots following the passage of ICESat from land to water is not appropriate (data before correction are underestimations, while data after correction are overestimations). The

difference between the errors observed for Lake Leman in comparison to French rivers is close to the results that Birkett obtained with altimetry radar for Lake Chad [8] and rivers in the Amazon basin [5].

Figure 6. Difference between GLAS and hydrological stations elevations (reference) for French rivers. Each point corresponds to one footprint (for a total of 46 footprints).

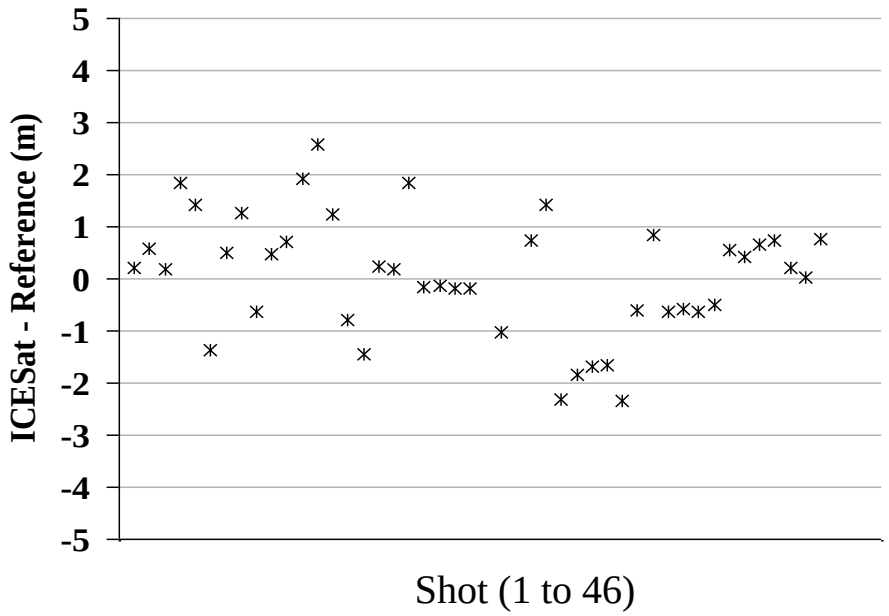

4. Conclusions

GLAS elevation precision for Lake Leman was similar to previously published values in the literature (RMSE between 5 and 30 cm with a mean value of approximately 15 cm). The saturation correction for GLAS elevation was necessary for consequent improvement of error (bias, RMSE). A precision greater than 15 cm for GLAS elevation was possible for bodies of water greater than 1.5 km. Indeed, the first ten footprints for only water after passage of laser from land to water are often saturated with an inappropriate saturation correction. These results demonstrated that several GLAS measurements are necessary to ensure that the GLAS system provides reliable saturation correction. GLAS temporal profiles reveal a slow progressive adaptation of the GLAS sensor before correct elevations can be proposed. This adaptation can reach 0.25 s (10 shots). Therefore, elevation measurements performed for the first hundred meters, which follow the land-water transition, are biased. For example, this adaptation distance is approximately 1.5 km for ten transition shots.

The GLAS precision was then evaluated for data acquired from rivers in France. The determined RMSE was 1.14 m (bias $\pm$ std = 0.07 m $\pm$ 1.15 m). This result demonstrates the difficulty of using GLAS data for rivers that are relatively smaller in width (inappropriate saturation correction).Therefore, a factor of 10 was determined for the GLAS precision between large lakes and small rivers.

The computed accuracy for ICESat water elevation data can make these data inconsistent depending on their hydrological use. When using water levels data to monitor the dynamic of water balance for large reservoirs, assimilation of water levels data with a metric accuracy can reduce errors of estimated water balance by a factor of two [19]. But according to studies on fluvial hydraulic simulation model

performances, the computed accuracy for ICESat water elevation is of poor interest [20]: for flood modeling in Europe occurring typically in low slopes fluvial environments, a decimeter accuracy of observed water levels, consistent with hydraulic output accuracies and fluvial slopes is required [21]. Assimilation of data with only decimeter accuracy adds meaningful value to hydraulic modeling, especially if this data is not frequent in space [22], which is the case of ICESat data.

Moreover, as the accurate ICESat measurements require significant water body width (hundreds of meters), the ICESat water level measurements are only adapted to major rivers and large catchment scales, or flood plains during extreme events.

Acknowledgements

The authors would like to thank the ICESat team and the National Snow and Ice Data Center for providing ICESat data and expertise. The authors would also like to thank the French National Water Observation Service "EauFrance" for providing access to the national gauge database.

References

1. Calmant, S.; Seyler, F. Continental surface waters from satellite altimetry. *Comptes Rendus Geosciences* **2006**, *338*, 1113-1122.
2. Hui, F.; Xu, B.; Huang, H.; Yu, Q.; Gong, P. Modelling spatial-temporal change of Poyang Lake using multitemporal Landsat imagery. *Int. J. Remote. Sens*. **2008**, *29*, 5767-5784.
3. Andreoli, R.; Yesou, H.; Li, J.; Desnos, Y.L. Inland Lake Monitoring Using Low and Medium Resolution ENVISAT ASAR and Optical Data: Case Study of Poyang Lake (Jiangxi, PR China). In *Proceedings of 2007 IEEE International Geoscience and Remote Sensing Symposium*, Barcelona, Spain, 23–28 July 2007; pp. 4578-4581.
4. Koblinsky, C.J.; Clarke, R.T.; Brenner, A.C.; Frey, H. Measurement of river level variations with satellite altimetry. *Water Resour. Res.* **1993**, *29*, 1839-1848.
5. Birkett, C.M.; Mertes, L.A.K.; Dunne, T.; Costa, M.; Jasinski, J. Surface water dynamics in the Amazon Basin: Application of satellite radar altimetry. *J. Geophys. Res*. **2002**, *107*, 1-21.
6. Coe, M.T.; Birkett, C.M. Calculation of river discharge and prediction of lake height from satellite radar altimetry: Example for the Lake Chad basin. *Water Resour. Res.* **2004**, *40*, 1-11.
7. Morris, C.S.; Gil, S.K. Evaluation of the TOPEX/Poseidon altimeter system over the Great lakes. *J. Geophys. Res.* **1994**, *99*, 24527-24539.
8. Birkett, C.M. Synergistic remote sensing of Lake Chad: Variability of basin inundation. *Remote. Sens. Environ.* **2000**, *72*, 218-236.
9. Crétaux, J.F.; Birkett, C. Lake studies from satellite radar altimetry. *Comptes Rendus Geosciences* **2006**, *338*, 1098-1112.
10. Schutz, B.; Zwally, H.; Shuman, C.; Hancock, D.; Dimarzio, J. Overview of the ICESat mission. *Geophys. Res. Lett.* **2005**, *32*, L21S01.
11. Zwally, H.J.; Schutz, B.; Abdalati, W.; Abshire, J.; Bentley, C.; Brenner, A.; Bufton, J.; Dezio, J.; Hancock, D.; Harding, D.; Herring, T.; Minster, B.; Quinn, K.; Palm, S.; Spinhirne, J.; Thomas, R. ICESat's laser measurements of Polar ice, atmosphere, ocean and land. *J. Geodynamics* **2002**, *34*, 405-445.

12. Urban, T.J.; Schutz, B.E.; Neuenschwander, A.L. A survey of ICESat coastal altimetry applications: Continental coast, open ocean island, and inland river. *Terr. Atmos. Ocean. Sci.* **2008**, *19*, 1-19.
13. Chipman, J.W.; Lillesand, T.M. Satellite-based assessment of the dynamics of new lakes in southern Egypt. *Int. J. Remote. Sens.* **2007**, *28*, 4365-4379.
14. Bhang, K.J.; Schwartz, F.W.; Braun, A. Verification of the vertical error in C-band SRTM DEM using ICESat and Landsat-7, Otter Tail County, MN. *IEEE Trans. Geosci. Remote Sens.* **2007**, *45*, 36-44.
15. Martin, C.F.; Thomas, R.H.; Krabill, W.B.; Manizade, S.S. ICESat range and mounting bias estimation over precisely-surveyed terrain. *Geophys. Res. Lett*. **2005**, *32*, L21S07.
16. Braun, A.; Cheng, K.; Csatho, B.; Shum, C.K. ICESat Laser Altimetry in the Great Lakes. In *Proceedings of the 60th Annual Meeting of the Institute of Navigation*, Dayton, OH, USA, 7–9 June 2004.
17. Federal Office for the Environment (FOEN). Hydrological Data. Available online: http://www.hydrodaten.admin.ch/e/index.htm (accessed on 1 April 2011).
18. Abshire, J.B.; Sun, X.L.; Riris, H.; Sirota, J.M.; McGarry, J.F.; Palm, S.; Yi, D.; Liiva, P. Geoscience Laser Altimeter System (GLAS) on the ICESat mission: On-orbit measurement performance. *Geophys. Res. Lett.* **2005**, *32*, L21S07.
19. Pereira-Cardenal, S.J.; Riegels, N.D.; Berry, P.A.M.; Smith, R.G.; Yakovlev, A.; Siegfried, T.U.; Bauer-Gottwein, P. Real-time remote sensing driven river basin modeling using radar altimetry. *Hydrol. Earth Syst. Sci.* **2011**, *15*, 241-254.
20. Schumann, G.; Bates, P.; Horritt, M.; Matgen, P.; Pappenberger, F. Progress in integration of remote sensing-derived flood extent and stage data and hydraulic models. *Rev. Geophys*. **2009**, *47*, RG4001.
21. Straatsma, M.; Huthoff, F. The Effect of Uncertain Floodplain Roughness in Hydrodynamic Flood Simulations. In *Proceedings of the 10th International Symposium on Stochastic Hydraulics*, Quebec City, QC, Canada, 1–10 July 2010.
22. Alsdorf, D.E.; Rodrguez, E.; Lettenmaier D.P. Measuring surface water from space. *Rev. Geophys.* **2007**, *45*, RG2002.

1.2. Improving the assessment of ICESat water altimetry accuracy accounting for autocorrelation

- **Abdallah H**., Bailly J.S., Baghdadi N., and Lemarquand N., 2011. Improving the assessment of ICESat water altimetry accuracy accounting for autocorrelation. ISPRS Journal of Photogrammetry and Remote Sensing, 66 (6), 833-844.

Improving the assessment of ICESat water altimetry accuracy accounting for autocorrelation

Hani Abdallah[a,*], Jean-Stéphane Bailly[b], Nicolas Baghdadi[a], Nicolas Lemarquand[a]

[a] *CEMAGREF, UMR TETIS, 500 rue François Breton, F-34093 Montpellier, France*
[b] *AgroParisTech, UMR TETIS, 500 rue François Breton, F-34093 Montpellier, France*

Abstract

[1] Given that water resources are scarce and are strained by competing demands, it has become crucial to develop and improve techniques to observe the temporal and spatial variations in the inland water volume. Due to the lack of data and the heterogeneity of water level stations, remote sensing, and especially altimetry from space, appear as complementary techniques for water level monitoring. In addition to spatial resolution and sampling rates in space or time, one of the most relevant criteria for satellite altimetry on inland water is the accuracy of the elevation data. Here, the accuracy of ICESat LIDAR altimetry product is assessed over the Great Lakes in North America. The accuracy assessment method used in this paper emphasizes on autocorrelation in high temporal frequency ICESat measurements. It also considers uncertainties resulting from both in situ lake level reference data. A prob-

*Phone: +33 467548719, Fax: +33 467548700
Email address: hani.abdallah@teledetection.fr (Hani Abdallah)

[1] **ABBREVIATIONS:**
ICESat: Ice Cloud and land Elevation Satellite
GLAS: Geoscience Laser Altimeter System
RMSE: Root Mean Square Error
SDOM: Standard Deviation Of the Mean

abilistic upscaling process was developed. This process is based on several successive ICESat shots averaged in a spatial transect accounting for autocorrelation between successive shots. The method also applies pre-processing of the ICESat data with saturation correction of ICESat waveforms, spatial filtering to avoid measurement disturbance from the land-water transition effects on waveform saturation and data selection to avoid trends in water elevations across space. Initially this paper analyzes 237 collected ICESat transects, consistent with the available hydrometric ground stations for four of the Great Lakes. By adapting a geostatistical framework, a high frequency autocorrelation between successive shot elevation values was observed and then modeled for 45% of the 237 transects. The modeled autocorrelation was therefore used to estimate water elevations at the transect scale and the resulting uncertainty for the 117 transects without trend. This uncertainty was 8 times greater than the usual computed uncertainty, when no temporal correlation is taken into account. This temporal correlation, corresponding to approximately 11 consecutive ICESat shots, could be linked to low transmitted ICESat GLAS energy and to poor weather conditions. Assuming Gaussian uncertainties for both reference data and ICESat data upscaled at the transect scale, we derived GLAS deviations statistics by averaging the results at station and lake scales. An overall bias of -4.6 cm (underestimation) and an overall standard deviation of 11.6 cm were computed for all lakes. Results demonstrated the relevance of taking autocorrelation into account in satellite data uncertainty assesment.

Keywords: GLAS, LIDAR, accuracy, temporal correlation, block kriging, Great Lakes

1. Introduction

Although lakes and rivers correspond to only 0.27% of the global fresh water and 0.007% of the Earth's water budget, they constitute the most accessible inland water resources available for ecosystems and human consumption.

Given that these resources are scarce and are strained by competing demands, it has become crucial to develop and improve techniques to observe the temporal and spatial variations in the water volume of lakes, rivers and wetlands to meet human needs and assess the ongoing impacts of climate change.

For this reason, most countries operate a national network of inland water level stations to collect information for water resource development. The installation and maintenance of such networks are expensive tasks that only international cooperation programs can initiate and sustain in many countries. The availability and access to data from water level stations are therefore severely limited due to a decline in the number of stations, inadequate monitoring networks, gaps in records, differences in processing and quality control, differences in datum level and differences in data policies (Harvey and Grabs, 2003; Chen and Chang, 2009). As a consequence, water resource sampling is neither spatially nor temporally homogeneous.

Due to the lack of data and the heterogeneity of water level stations, remote sensing, and especially altimetry from space, appear as complementary techniques for water level monitoring (Calmant and Seyler, 2006).

Satellite radar altimetry first appeared in 1974 with Skylab. In 1975, the GEOS-3 radar altimeter was designed to monitor ocean surfaces, followed by the SEASAT (1978) and GEOSAT (1985-1989) missions. Radar altimetry

entered a pre-operational phase in 1992 with the satellites ERS and Topex-Poseidon, followed by Envisat and Jason in 2001. All these missions were originally designed for measuring the level of the ocean through a combination of a radar technique determining the distance from the satellite to the reflecting surface and a satellite positioning technology identifying the precise location (within centimeters) of the satellite. Since 1990, the radar elevation measurements have demonstrated their relevance for inland water observation (Bercher, 2008). The application of this technique in the literature has allowed monitoring of the inland seas (Aladin et al., 2005), lakes (Birkett, 1995, 2000; Birkett et al., 2002; Crétaux and Birkett, 2006) and large rivers (Birkett, 1998; Mercier, 2001; Maheu et al., 2003).

In addition to spatial resolution and sampling rates in space or time, the most relevant criterion for satellite altimetry on inland water is the accuracy of the elevation data; therefore, many studies aimed to quantify these accuracies. Morris and Gill (1994) found a Topex-Poseidon data RMSE (Root Mean Square Error) of a few centimeters on the Great Lakes of North America. Studies over other world lakes indicated the following RMSE values: i) greater than 10 cm for Lake Chad (Birkett, 2000); ii) approximately 5 cm for Issyk Kul Lake, Kyrgyzstan; and iii) 10 cm for Chardarya Lake, Kazakhstan (Crétaux and Birkett, 2006). The accuracy of radar altimetry was also studied for a selection of rivers and floodplains in the Amazon Basin. Substantial errors were observed with RMSE values between 40 cm and 1.1 m (Birkett et al., 2002; Bercher, 2008).

In recent years, LIDAR onboard satellite also appears as a promising tool for accurate, high resolution altimetry. The Geoscience Laser Altimeter System (GLAS) ranging instrument onboard the ICESat (Ice Cloud and land Elevation Satellite) provides elevation data over all Earth surfaces. Its main

strength is its small footprint diameter averaged over 70 m (Zwally et al., 2002) compared to the larger radar footprint size of 250 m to a few km. This relative small footprint size is promising for inland water monitoring, especially in rivers. ICESat was launched on the 13 January 2003 and the mission stopped at 14 august 2010. It included three lasers that transmitted short pulses (4-6 ns) of infrared light (1064 nm) and visible green light (532 nm). GLAS used 1064-nm laser pulses to measure the heights of the surface and dense cloud and 532 nm pulses to measure the vertical distribution of clouds and aerosols. The 1064-nm signal was also separately filtered and digitized at 2 MHz for detection of dense clouds and aerosols at 76.8-m vertical resolution. The three lasers have been operated one at a time, sequentially throughout the mission. To extend mission life, the operational mode included 33-day to 56-day campaigns, several times per year. Each period has been assigned a campaign or operations period identifier, such as Laser 2a, to denote the operating laser (2) and the operations period (a) (Schutz et al., 2005). Laser pulses or shots at 40 Hz illuminated sites spaced at 170-meter intervals along track over Earth's surface. The primary mission of GLAS was to measure changes in ice sheet elevation, and secondary objectives included the measurement of cloud and aerosol height profiles, land elevation, vegetation cover and sea ice thickness (Zwally et al., 2002; Schutz et al., 2005). Although less devoted to water monitoring compared to radar altimetry, these LIDAR data could also be used to observe the inland water altimetry (Urban et al., 2008).

To date, few studies assessed GLAS elevation data accuracy for inland waters. The estimated standard deviation of GLAS elevation data computed on Lake Nasser in southern Egypt range from 3 to 8 cm (Chipman and Lillesand, 2007). On Otter Tail County lakes (USA), Bhang et al. (2007)

indicates differences between GLAS elevation and hydrologic station elevation ranging from 2 to 35 cm. Urban et al. (2008) reports GLAS elevation RMSE of approximately 3 cm under clear conditions, 8-15 cm under cloudy skies and 25 cm under very cloudy skies on the Tapajos Rivers (Brazil).

Several problems were revealed in previous satellite altimetry accuracy studies. First, detailed descriptions of the assumptions and accuracy statistics computation are lacking. Second, most of the studies compute errors between satellite and ground data considering ground data as 'truth', or exact and free from uncertainty. Consequently, in terms of error distribution estimation, most studies only compute RMSE as an accuracy statistic, but despite its common use, RMSE is inadequate because it mixes the bias (exactness) and dispersion (standard deviation) of satellite measurements, which can have very different consequences on their final utility. Moreover, no study compares a single shot elevation value to the ground reference data; rather, studies compare reference data to an average of successive shots, consistent with the bodies of water under consideration, such as a river section or a continuous lake transect. Therefore, before accuracy statistics computation, an implicit aggregating or upscaling process, which is typically an average based on the arithmetic mean, involves successive shot elevation values that occurs at the scale of the studied water body. As a result from this aggregating process, the satellite 'measurement' is thus compared to the corresponding ground data. The use of an arithmetic average assumes that successive shots are considered as independent (Morris and Gill, 1994) and identically distributed, allowing the usual statistics computation on measurement uncertainties, such as the SDOM (Standard Deviation of the Mean).

The centimeter differences observed between satellite measurements and ground measurements and the uncertainty of both measurements can make

the error word inappropriate to qualify the observed deviations between satellite and ground measurements. If not, how to estimate the bias (mean) and dispersion of these deviations ? To answer this question, we need to first consider the satellite and ground measurements as random variables and to verify their significant deviations by computing the uncertainty of each measurement, ground measurements and satellite measurements, at water body scale. The uncertainty of satellite measurements at water body scale can be estimated using the SDOM only if the shot elevation values are, for high frequencies, independent in time and space. If not, the correlation between successive shot altimetrical values, denoted further as autocorrelation, must be modeled and estimated. Uncertainty at the water body scale must be computed accordingly. Although infrequent in satellite elevation data, the support effect accounts for the dependence between sequential measurements in upscaling and is a typical practice used on spatial data (Chiles and Delfiner, 1999) (Atkinson and Tate, 2000). It has already been used for remote sensing data accuracy assessments (Crosson et al., 2010) and even on LIDAR data (Bailly et al., 2010).

This paper aims to i) explore the high frequencies autocorrelation in GLAS-ICESat water elevation shot data, ii) assess the consequences of this autocorrelation in the uncertainty statistics on water level estimates and iii) assess the consequences of this autocorrelation in deviations to ground station elevation data from the Great Lakes. To ensure a proper comparison, ICESat data pre-processing was first performed. It consisted of i) the exclusion of shots with waveform saturation corresponding to data near land (Baghdadi et al., 2011), ii) the exclusion of shot outliers from atmospheric disturbance, iii) the application of saturation corrections to initial elevations (Urban et al., 2008) and iiii) the exclusion of data when lake water surface

can not be considered as flat for accuracy and deviations estimates. The autocorrelation between successive shot elevation values was first tested and modeled for each of the considered sets of shots. A set of shots consist of a GLAS transect within a Great Lake, spatially coherent with a given ground water-level station (a water body) and temporally located in the same satellite track. We thus proposed an explicative model of the autocorrelation presence. In cases of significant autocorrelation and absence of trend in transect shot data, a block kriging process (Wackernagel, 1995) was used to estimate a mean water elevation at the transect scale and its uncertainty, Finally, the ground measurements and satellite measurements and their relative uncertainties at the transect scale were estimated. By considering these two water elevation estimates as random variables, according deviations statistics (bias and standard deviations) were proposed.

2. Study site and data set description

2.1. Study site

Due to the lack of data on one of the five Great Lakes in North America, the assessment of GLAS-ICESat elevation data accuracy was assessed for the following lakes: Superior, Michigan, Erie and Ontario. One of the youngest natural features on the North American continent, the Great Lakes make up the largest surface freshwater system on Earth. Covering more than 94,000 square miles and draining more than twice as much land, these freshwater seas hold an estimated 22.7 trilliards cubic meters of water, approximately one-fifth of the world's surface freshwater and nine-tenths of the U.S. supply. A network of 52 hydrometric stations monitor the Great Lakes (25 Canadian MEDS station and 27 US NOAA stations) for level measurement (Fig. 1).

The Great Lakes have from 1 to 4 cm tides but no prevalent ocean tides. Thus, the Great Lakes are an excellent site for accuracy studies.

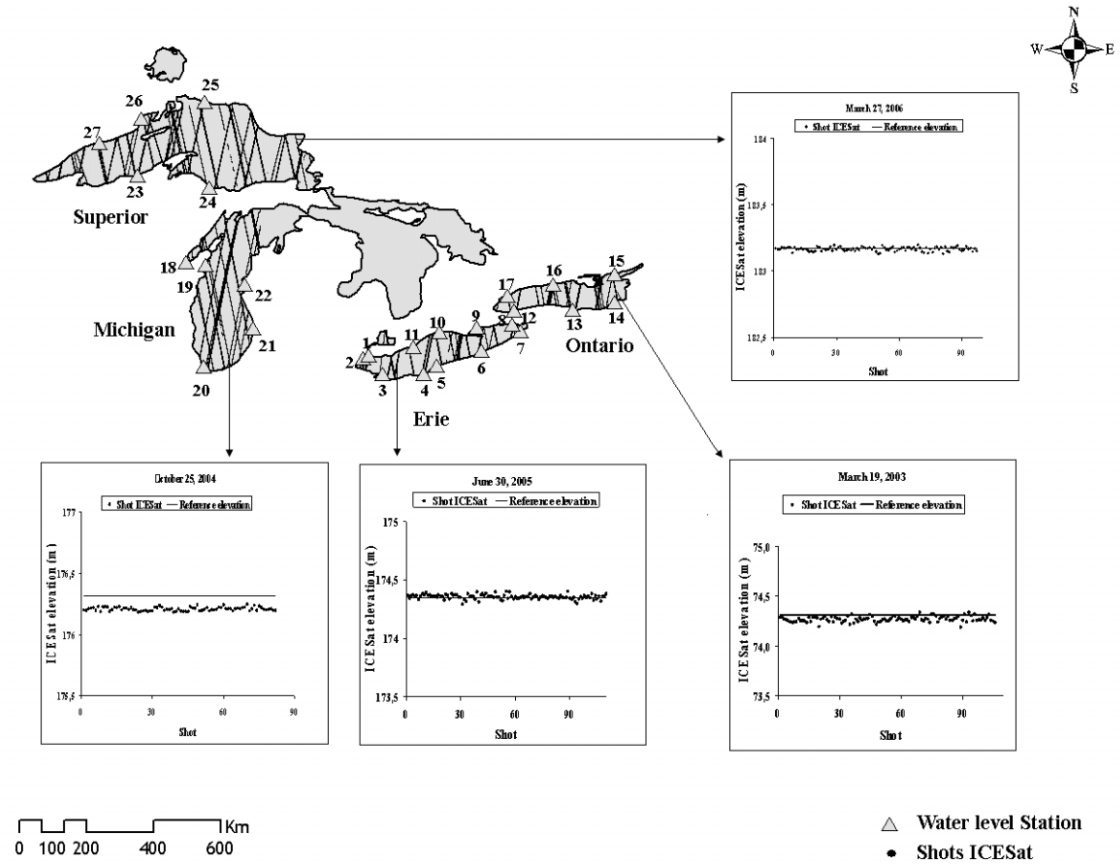

Fig 1: GLAS-ICESat shots forming transects over the Great Lakes and the location of the 27 hydrometric stations.

2.2. Data set

2.2.1. ICESat data

The GLAS elevation data used in this study are the Level-2 altimetry products GLA14 and GLA01 (Release 31) that provide surface elevation measurements (land, water, etc.) and corresponding waveforms. GLA14 data also include the laser footprint geolocation with a precision smaller than 4 m (Duong et al., 2006). GLA01 data include waveforms that have been decomposed into multiple Gaussian distributions (Wagner et al., 2006; Jutzi and Stilla, 2006; Chen, 2010) corresponding to 544 or 1000 samples of received power in volts at 1 ns sampling rate (see Zwally et al. (2002) for a detailed description of ICESat full waveform data). These data record the period between 20 February 2003 and 11 October 2009. In this study, 237 ICESat transects, with lengths ranging from 5 to 20 km, containing 20,224 shots have been used (Table 1). These 237 selected transects are the set of continuous tracks of shots that are i) in a radius of 20 km from an available hydrometric station to avoid the influence of natural spatial lake level variations and ii) at least 2 km from the shore to avoid measurement disturbance from land-water transition effects on waveform saturation (Baghdadi et al., 2011).

Next we developed a two step GLA14 data cleaning procedure, close to the one proposed by Zhang et al. (2011). In step 1, each of the 237 GLAS ICESat transects was first visualy inspected on time-elevation bivariate plots (Figs. 5-a and 5-b) in order to remove obvious outliers and to verify that the water level was almost constant. Some parts of the transects were accordingly excluded when the mean water level varied or when observations were 'constant' due to i) cloudy episodes with outlier elevations in transect (in-

dicating a difference in elevation of approximately 1000 m) (Wesche et al., 2009), ii) the proximity of river outlets. Fig. 2 shows the only example of this phenomenon: the extended transect of 14 June 2005 for Station 21 (Holland station) on Lake Michigan is located near an important river outlet (Fig. 2-a). The transect profile shows the 85 km elevation profile track that increases in the middle near the outlet, producing an upper water level of approximately 70 cm. In Step 2, for each transect, the median elevation value of the remaining shots was calculated and the shots which were at least 4 meters far from this median value were removed.

2.2.2. Water level reference data

The reference lake level data in this study were obtained from 27 of the 52 water level stations located throughout the Great Lakes basin. The selected stations are near (less than 20 km) the transect of the GLAS footprints. Eleven stations are operated by the Marine and Environmental Data Service (MEDS) of Canada's Department of Fisheries and Oceans, and 16 stations are operated by the U.S. National Oceanic and Atmospheric Administration (NOAA). Both NOAA and MEDS stations continuously monitor the surface levels of the four lakes at 6 minutes intervals (Braun et al., 2004) with a standard deviation of 2 cm (Hovis et al., 2004).

North American Great Lakes are known to have low tides but are sensitive to short-term water-level fluctuations, such as up to 2.44 m in approximately 2 hours, caused by wind or storm surges, which are known as seiches (Touchart, 2002). Considering this phenomenon and because the ICESat transect lasts very few seconds and a hydrometric station may have a timing bias of a few minutes, this study analyzed the dispersion of recorded ground

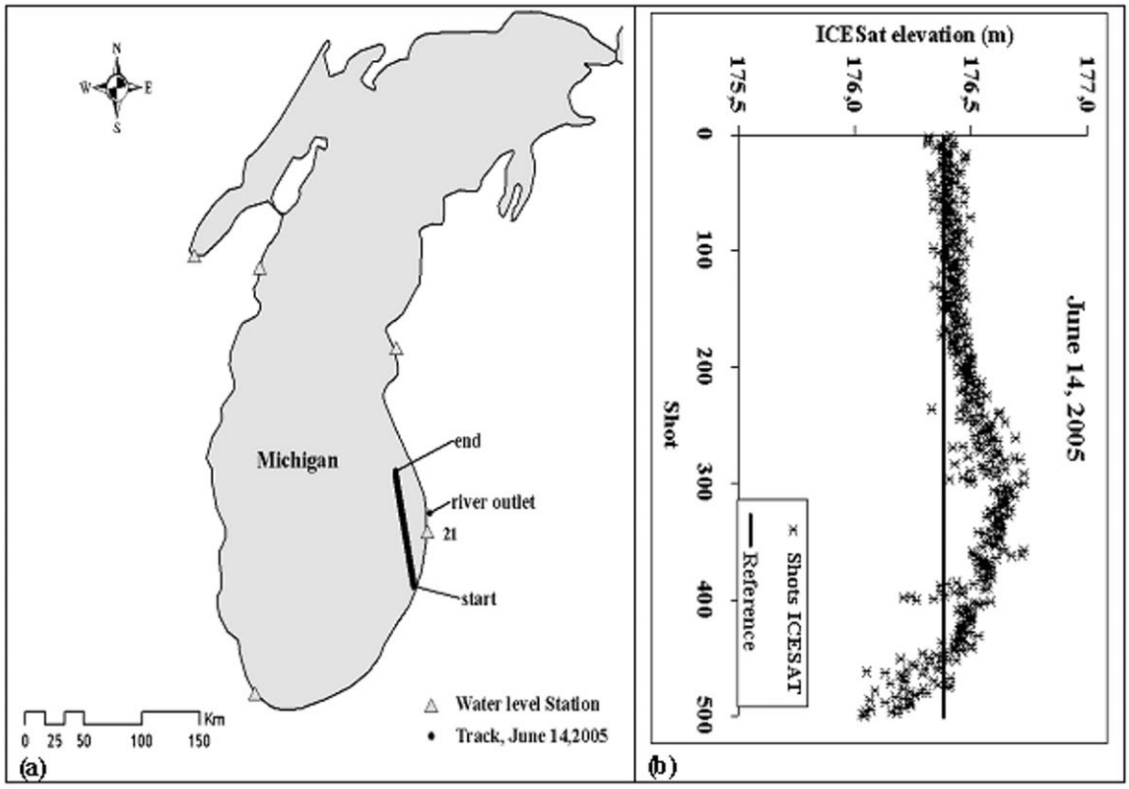

Fig 2: (a) GLAS transect of 14 June 2005 at Holland station (Number 21) on Lake Michigan; (b) the corresponding ICESat elevation profile (with abscissae = shot number) in comparison to hydrometric station data (reference elevation).

measurement (hydrometric station data) in a 6-minute range around transect ICESat times for all stations. This analysis exhibits a constant dispersion for each station of 7 mm for one standard deviation.

In addition, the geoid model G99SSS used in this study to convert the reference data from ellipsoidal height (WGS84) to orthometric height (NAVD88) has a mean error of approximately 2.5 cm (Smith and Roman, 2001).

Given that these different sources of uncertainty are independent, they can be summed (in variance). As a result, the computed uncertainty on

reference ground data was estimated to 3.3 cm for one standard deviation (σ_R).

2.2.3. Data consistency

GLA14 products provide original elevation data with ellipsoidal heights based on the same ellipsoid used by the Topex satellite. The lake level data collected from hydrometric stations are in the International Great Lakes Datum of 1985 (IGLD85). Consequently, data transformations are required in order to conduct a consistent comparison in the same reference frame. GLAS heights and lake level heights were therefore converted to the same vertical datum NAVD88. Two successive transformations are required for GLAS heights: the first converts the Topex ellipsoidal heights to WGS84 ellipsoidal heigts using the geoid model EGM96; the second transforms the WGS84 ellipsoidal heights to NAVD88 orthometric heights using the geodic model G99SSS. For hydrometric station elevation data, the IGLD85 lake level datum converts to orthometric height NAVD88.

3. Methods

3.1. GLAS water elevation saturation correction

Some ICESat waveforms exhibit distortions, or saturation events, when the high energy emitted by the laser returns, passes the inadequate automatic gain controls and overloads the detector (Sun et al., 2005). This occurs when the amplitude of the energy returned by a number of 1-ns bins is greater than the threshold function of gain (Urban et al., 2008; Abshire et al., 2005), producing an incorrect elevation. The ICESat science team has developed an analytical saturation correction, also available on the data products. Adding this correction to the elevation is recommended for ice

and calm water data, but not over oceans (Urban et al., 2008). Corrections vary between 0 and 1.5 m. For some waveforms, the saturation should be corrected but the method used to calculate the correction coefficient cannot provide a correct value and is marked by '-999.00' flags. Fig. 3 shows some ICESat waveforms obtained across Lake Superior; the saturated waveform is clipped and widened artificially by the returning high energy.

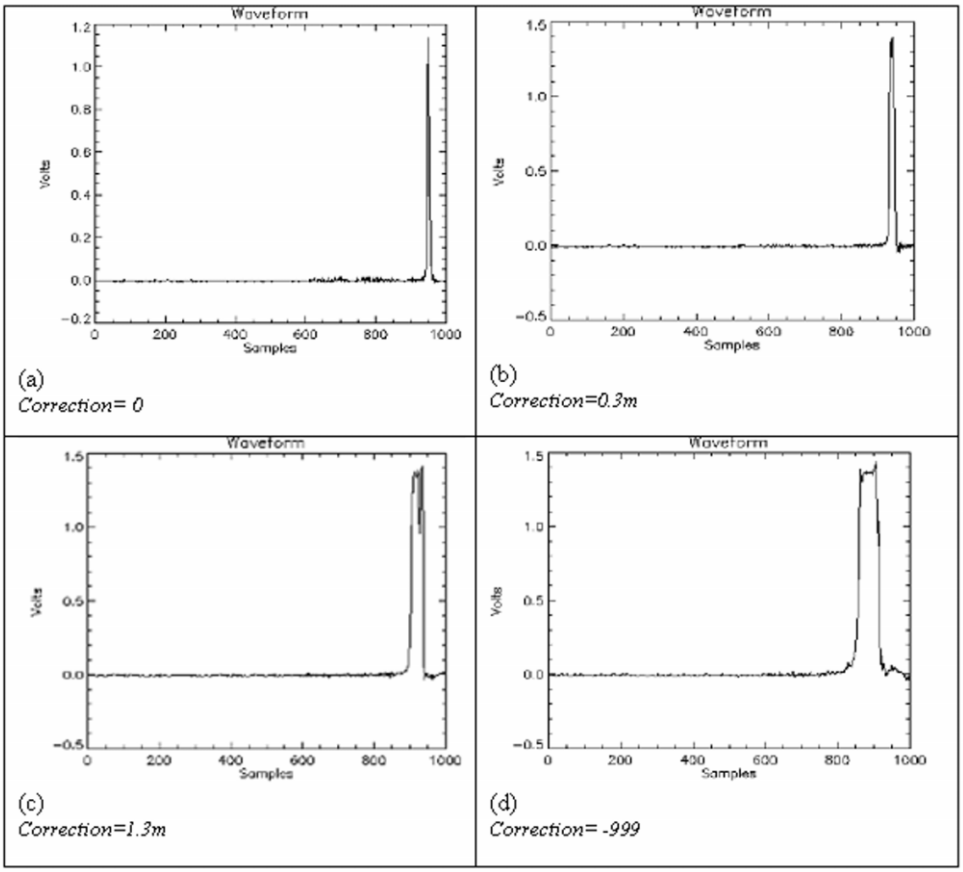

Fig 3: Example of GLAS waveforms on Lake Superior: (a) Unsaturated waveform ; (b) Waveform with low saturation ; (c) and (d) waveforms with high saturation. Ordinate = energy in volts and abscissae = bins number (bins spacing = 1 ns).

Fig. 4 illustrates an example of elevation transects before and after application of the saturation correction. The saturation correction allows a reduction of error bias but does not reduce the error dispersion in the figure.

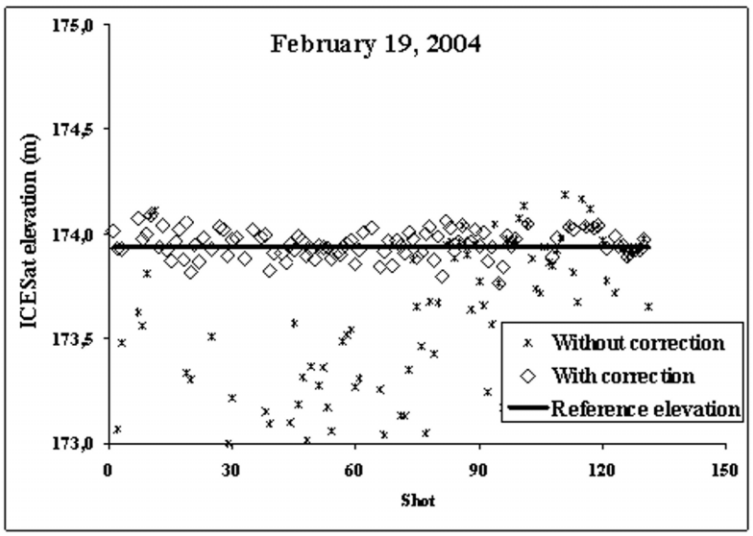

Fig 4: Example of a GLAS-ICESat transect compared to reference elevation. Abscissae = shot number and ordinate = elevation (ICESat with and without saturation correction and hydrometric station).

3.2. GLAS water elevation estimation at transect scale

To compute the GLAS water elevation estimate $\hat{Z}_G$ and uncertainty σ_G at the transect scale and considering autocorrelation, we used a statistical framework based on the regional variable and random field theories (Cressie, 1993). In this framework, a GLAS transect is viewed as a temporal block, or a delimited part of a temporal random field ($z(t)$). For each GLAS transect, we

developed the usual block kriging process (Wackernagel, 1995, p.77) based on an autocorrelation model, allowing both the estimation of the water elevation $\hat{Z}_G$ and its corresponding uncertainty σ_G, at the transect scale.

3.2.1. Autocorrelation test and modeling

A GLAS transect is composed from $(t_1 \dots t_n)$ and $(z_1 \dots z_n)$ series, respectively, where t refers to the laser shot (pulse) time, z to the elevation in the NAVD88 altimetrical system and n is the number of shots in the transect. These series are denoted as $z(t)$ and are considered to be a realization of a stationary temporal random function. We want to infer the main property of $z(t)$, its temporal correlation (autocorrelation), especially the high frequency autocorrelation. When $z(t)$ is stationary, with constant expectation and homogeneous temporal covariance, this inference is possible using the variogram modeling of the field $z(t)$, equivalent to the covariance.

Elevation trend test at transect scale. To ensure a stationary process and reenforce the high frequency autocorrelation test power (Armstrong, 1984), a linear trend test is first performed. A linear model $z(t) = m(t)+y(t)$, where $m(t) = at + b$ is the linear regression of z by t, and $y(t)$ are the residuals of this linear regression, is fitted. Using the usual T-test on the coefficient a it is tested if a linear trend is significant.

Next, when the trend tests positively, the initial $z(t)$ field is decomposed in two additive term $m(t) + y(t)$, with $m(t)$ a deterministic trend term and $y(t)$ a term consisting of random residuals. When the trend is negative, the $m(t)$ term disappears and we write $z(t) = y(t)$ for the sake of simplicity. To enable a valid comparison between ground station and GLAS measurements and to avoid natural spatial variations of lake water levels at high spatial frequencies, only transects without linear trends were kept further to compute

the GLAS deviations and accuracy.

Autocorrelation significance test. Next, to estimate the autocorrelation of $z(t)$ transect data, an experimental variogram $\gamma(\hat{h})$, with h equal to lag time, is computed on the $y(t)$ data (see Wackernagel (1995, p.35) for the usual experimental variogram formulation). This variogram was computed on 16 regular lag times each 62.5 ms ranging from 0 to 1 s, chosen to obtain numerous shot pairs for an accurate variogram estimation for each lag time h. An autocorrelation is considered significant when the experimental variogram graph shows a clear increasing shape from small time differences to large time differences. When the corresponding experimental variogram graph shows a flat variogram, no autocorrelation for this GLAS transect exists. To test the significance of the autocorrelation calculated from the experimental variogram, we used the standard empirical Mantel test (Legendre and Fortin, 1989), which simulates data corresponding to the null hypothesis H_0 through data permutations, where H_0 corresponds to the absence of autocorrelation (Fig. 5-c). At each permutation of the z data, a corresponding experimental variogram is computed. For numerous replications of the permutations, we obtained a quintile distribution of variograms representing H_0 for each lag time h. The H_0 acceptance area is thus represented in the variogram graph through a 95% confidence band of H_0. In the case of significant autocorrelation, the actual experimental variogram for small values of h is below the 2.5% quintile of H_0 (the lower line of the band). Here, we chose to reject H_0 only when the first variogram point was below the 2.5% quintile of H_0.

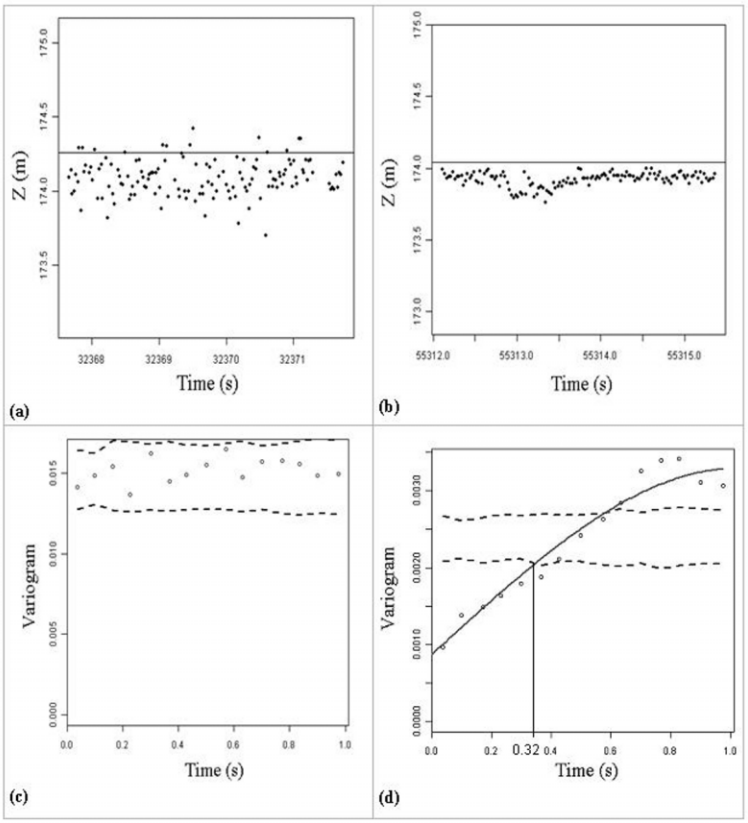

Fig 5: (a) and (b): temporal series $z(t)$, and (c) and (d): corresponding experimental variograms obtained on the transect at Port Colborne station from 2 February 2005 (a, c) and Bar Point station from 10 May 2007 (b, d). The dashed lines in (c, d) represent the two H_0 envelopes, the straight lines in (a, b) represent the reference elevation, and the curve lines in (c, d) are the spherical model function fitted to the experimental variogram (points on c, d). (a, c): absence of autocorrelation. (b, d): significant autocorrelation. (d) Variogram range = 0.32 s.

Autocorrelation modeling. In the case of a significant experimental variogram (Fig. 5-d), we chose to model it with a single spherical model function given

by:

$$\gamma(h) = \begin{cases} nu + (si - nu)(\frac{3h}{2r} - \frac{h^3}{2r^3}) & \text{if } h < r \\ (nu + si) & \text{if } h \geq r \end{cases} \quad (1)$$

Using a weighted least-square estimation (Pebesma and Wesseling, 1998), the model parameters nugget (nu), range (r) and sill (si) were fitted. This was done automatically for all GLAS transects from initial fitting parameters corresponding to a nugget equal to the experimental variogram at a smaller lag time, a sill equal to the maximum value of the experimental variogram and a range equal to the time duration at which the variogram reaches its maxium. After the fitting process, a variogram model $\gamma(h)$ was obtained as shown in the example by the fitted line in Fig. 5-d.

3.2.2. Transect water elevation estimation with autocorrelation: block kriging

For a GLAS transect, when autocorrelation is significant and modeled, a mean value $\hat{Z_G}$ for the transect is estimated from transect data $z(t)$ from $\hat{Y}$. The $\hat{Y}$ estimate is computed through a block kriging process of $y(t)$ (Wackernagel, 1995, p.77) using the variogram model $\gamma(h)$. $\hat{Y}$ is therefore a linear combination of $y(t)$ data with kriging weights β_i:

$$\hat{Y} = \sum_{i=1}^{n} \beta_i y_i \quad (2)$$

Uncertainty on $\hat{Z_G}$ is represented in the block kriging estimation standard deviation σ_G given by (Wackernagel, 1995, p.77):

$$\sigma_G = \sqrt{\mu_{BK} + \bar{\gamma} + 2\sum_{i=1}^{n} \beta_i \bar{\gamma}(t_i, T)} \quad (3)$$

In this equation, μ_{BK} is the Lagrange multiplier deduced from the block kriging system, $\bar{\gamma}(t_i, T)$ is the average variogram computed between the sample point t_i and all points of the transect T (block) and $\bar{\gamma}$ is the variance within the transect. In practice, both $\hat{Z_G}$ and σ_G are approximated through the average of gridded points within the considered GLAS transect. We chose a gridding step of $10ms$ here corresponding to 1/4 of the time lag between pulses. Note that σ_G only depends on the data temporal sampling scheme, not on the elevation values z. Consequently, given that the temporal sampling scheme of ICESat data is almost regular, except when outliers are excluded from the initial transect data, σ_G primarily depends on the transect total duration.

When no autocorrelation is observed for a given GLAS transect (H_0 is accepted), $\gamma(h)$ is a pure nugget effect variogram. In this particular case, kriging weights β_i in equation 2 are all equal and equation 3 is simplified to the common SDOM formulation. Consequently $\hat{Z_G}$ equals the arithmetic mean $\bar{z}$ of the values z_i.

3.3. GLAS deviations to reference water elevation at transect scale

For each transect j where no linear trend has been observed, a GLAS estimated value $\hat{Z_G}$ having σ_G Gaussian uncertainty was compared to a reference value Z_R having σ_R Gaussian uncertainty. As GLAS and reference elevations can be considered independent Gaussian random variables, the distribution of the deviations between GLAS and reference water elevations can be assumed also to be of Gaussian distribution $N(\mu_j, \sigma_j)$, with $\mu_j = \hat{Z_G} - Z_R$ and standard deviation $\sigma_j = \sqrt{\sigma_G^2 + \sigma_R^2}$.

From these Gaussian deviation distributions obtained for a transect, GLAS deviation statistics (accuracy) were computed at station, lake or Great

Lakes scales, by simply averaging the cumulative probability functions of the Gaussian laws $N(\mu_j, \sigma_j)$ and computing the resulting empirical deviation distribution (not necessarily Gaussian).

From this empirical distribution, the first (bias) and second (standard deviation) moments were estimated to propose GLAS accuracy statistics.

4. Results and discussion

4.1. Autocorrelation between GLAS shot measurments

A significant high frequency autocorrelation is observed for 107 transects, i.e. 45% of the initial 237 transects. No direct explanation is known to the authors for the occurrence of the autocorrelation as shown in Fig. 6, although corrrelated and non-correlated transects look randomly distributed in space (Fig. 6-a), or in time (Fig. 6-b). It does not depend on the overall water level (low or high) in the lake (Fig. 6-b). For the transects that do experience significant correlation the 107 fitted variogram models show:

- a $\frac{nugget}{nugget+sill}$ ratio ranging from 0.24 to 0.52 with a mean value of 0.4. This value means that there is in average 40 % of randomness between two consecutive, i.e. very close, shots.

- a range ranging from 0.27 s to 0.34 s with a mean value of 0.3 s (time the variogram model becomes flat at sill value). This range corresponds to the duration of 11 pulses and a distance along the transect of approximately 1.9 km.

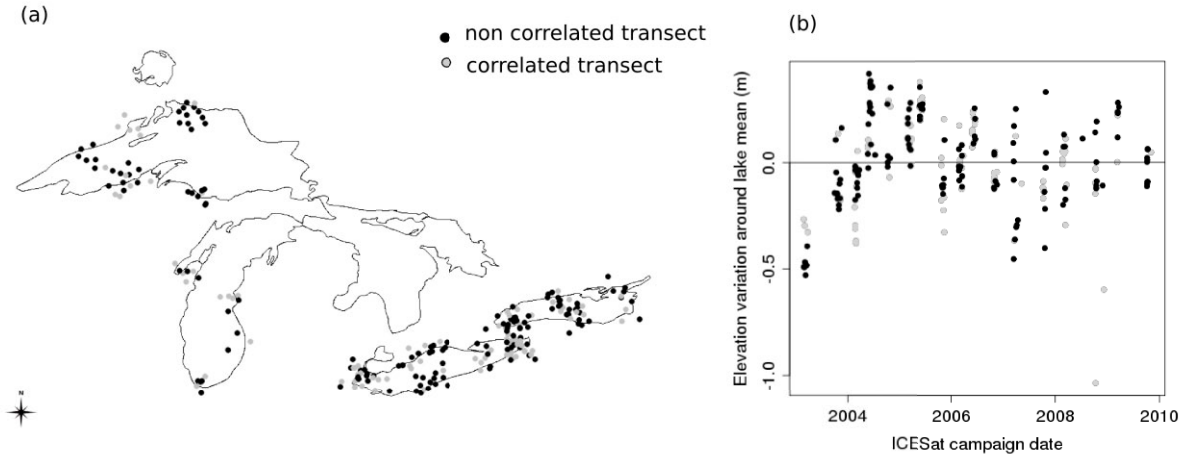

Fig 6: (a) Correlated and non-correlated GLAS transects on the Great Lakes - exact locations of transects have been slightly translated to depict overlapping transects; (b) correlated and non-correlated GLAS transects along the ICESat mission dates - the ordinate is the deviation between the reference elevation of a given lake at each transect date and the mean elevation of the lake calculated using reference elevations for all dates.

4.2. Autocorrelation explanation

To explore the physical explanation of the significant autocorrelation observed for 45% of the GLAS transects, we attributed to each one of the 237 transects i) the environmental parameters from the ICESat data at the transect time (surface temperature, surface humidity and pressure) and ii) the GLA14 instrument parameters (transmitted energy, received energy, gain, incidence angle, laser campaign, transect direction and transect dates according to the beginning and end of each laser campaign (Schutz et al., 2005, table 1, p.2)). To explore relationships between the presence of autocorrelation and these available system or environmental parameters, they were all first considered as potential temporal autocorrelation predictors. We used the multivariate classification tree (CART) method of Breiman et al.

(1984) that computes predictor importance that explains autocorrelation by using indifferrently quantitative or qualitative predictors. The obtained classification tree in Fig. 7 shows separation between the autocorrelated (1) and non-autocorrelated (0) transects based respectively on the transmitted energy (TE), temperature (temp) and pressure (pressure). This tree explain 68% of the autocorrelation. These results show that the transmitted energy plays a major role in autocorrelation among all parameters. We thus draw from this analysis that significant autocorrelation occurs when the GLAS instrument transmits low energy which notably occurs at the end of each of three lasers life times, and when bad weather conditions are marked by either lower temperature or lower pressure. These results are consistent with no systematic autocorrelation observed in space or time that could have come from satellite system behaviour.

4.3. Autocorrelation effect on GLAS water elevation uncertainties at transect scale

Z_G estimates and corresponding σ_G uncertainty parameters were computed for the 117 transects where no significant trend has been observed. When no autocorrelation is observed for the transect, we used the block kriging process (Equation 2), and if not, we used the Standard Deviation Of the Mean (SDOM). Fig. 8 depicts the distribution of the σ_G uncertainty parameters for transects as a function of the pulse number composing the transect and the presence or absence of autocorrelation. It appears clearly on this figure that the presence of autocorrelation multiplies the σ_G uncertainty by 8 on average. As expected, accounting for autocorrelation drastically changes the σ_G estimation, even if the $\hat{Z_G}$ values differ only slightly (due to

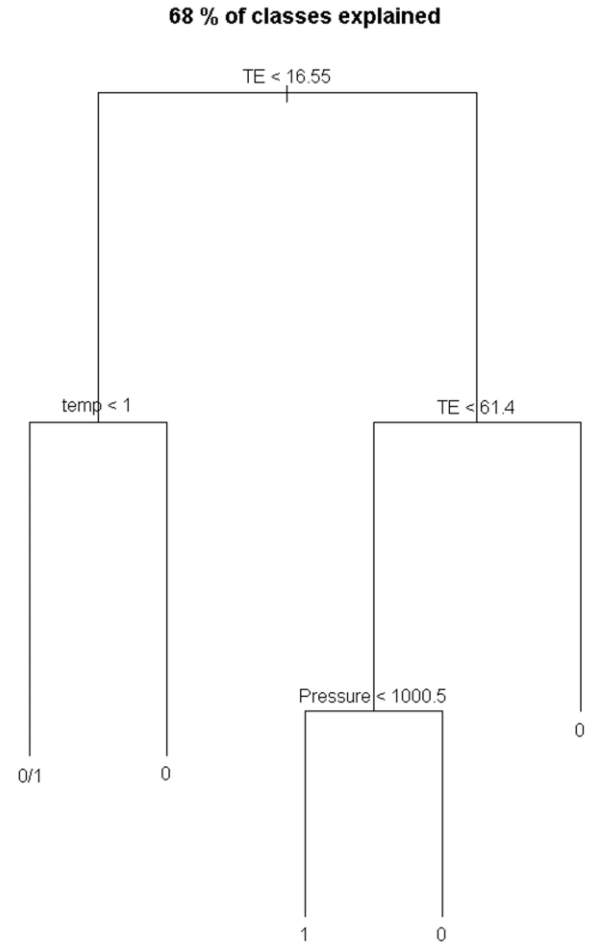

Fig 7: Classification tree explaining the autocorrelation of the transects. A value of 0 on leaves denotes the absence of autocorrelation, and a value of 1 on leaves denotes autocorrelation. The 0/1 value on a leaf means that it mixes correlated and non-correlated transects in equal proportions.

the regular time sampling of GLAS measurements). This usual geostatistical result comes from autocorelation that acts as diminishing the number of data.

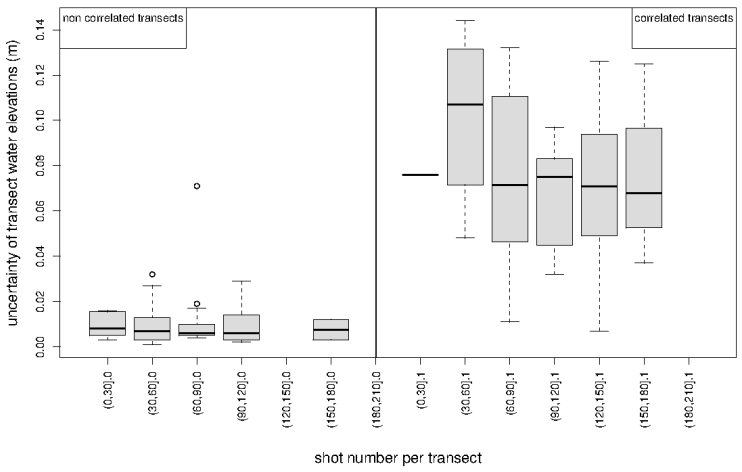

Fig 8: Distribution of the standard deviation σ_G characterizing the uncertainty of estimated water elevations at the transect scale from GLAS data. This distribution is shown as a function of the shot number composing the transect and presence (right) or absence (left) of autocorrelation.

4.4. GLAS water elevation deviation distribution

The GLAS deviation, the difference between the GLAS and reference elevation, is considered as a random variable. The distributions of these deviations were computed for all Great Lakes together, for individual lakes and at station scale. For all Great Lakes, the probability of a GLAS water elevation deviation to be lower than 1 cm, 10 cm and 20 cm in absolute values is 7.5%, 66.8% and 91.9%, respectively, which seems close to a $N(0, 10cm)$ value. The 2.5% and 97.5% quantiles are 29 cm and 16 cm, respectively. The expectation of this distribution is -4.6 cm.

Examples of distributions are depicted in Fig. 9, for all Great Lakes, at lake scale (for lake Erie and lake Ontario), at station scale (for station Erie, Fermi Power, Rochester and Toronto) and at transect scale (transect

number 5,8,26,24,88,85,92,90). The mix of deviation distributions at the lake scale gives the overall Great Lakes deviation distribution. Normality of deviation distributions is clearly low when downscaling. At station scale, there are various shapes of deviation distribution, non-symetric, with positive or negative pseudo-biases. The mix of these deviation distributions at the station scale, with weights equal to transect numbers for each station of a lake, provides the lake deviation distribution.

However, these results show that when aggregating numerous data, i.e. transects at the Great Lakes scale, and due to the general Law of Large Numbers, the obtained shapes of deviation distribution become nearly Gaussian. This is not true at the station scale where shapes are asymmetrical and complex. In this latter case, attention must be paid in using common accuracy statistics, especially for dispersion parameters.

4.5. GLAS accuracy parameters

The right part of Table 1 summarizes the results of the biases and standard deviations statistics at the Great Lakes, lake and station scales. At the Great Lakes scale, the GLAS deviation bias is -4.6 cm. In other words, GLAS is slightly underestimating the water elevation on average. The bias values range from -11.4 cm to -2.1 cm at the lake scale and from -14.5 cm to 3.8 cm at the station scale. The bias found on the stations of the Michigan Lake is the higher in magnitude, reaching up to -14.5 cm for Station Kewaunee. A standard deviation of 11.6 cm was computed at the Great Lakes scale. It varies from 7.9 cm to 12.9 cm at the lake scale and from 3.3 cm to 13.7 cm at the station scale. The highest standard deviation was found at Station Ludington on Lake Michigan. Bias and standard deviation

statistics clearly differ from one lake, or one station, to the next. All these standard deviations must be compared in magnitude with the reference data uncertainties (3.3 cm for one standard deviation) and GLAS water elevation estimate uncertainty at the transect scale (Fig. 8). They are clearly of higher magnitude than the reference data uncertainties but are of the same order as the GLAS water elevation estimate uncertainty when autocorrelation is significant.

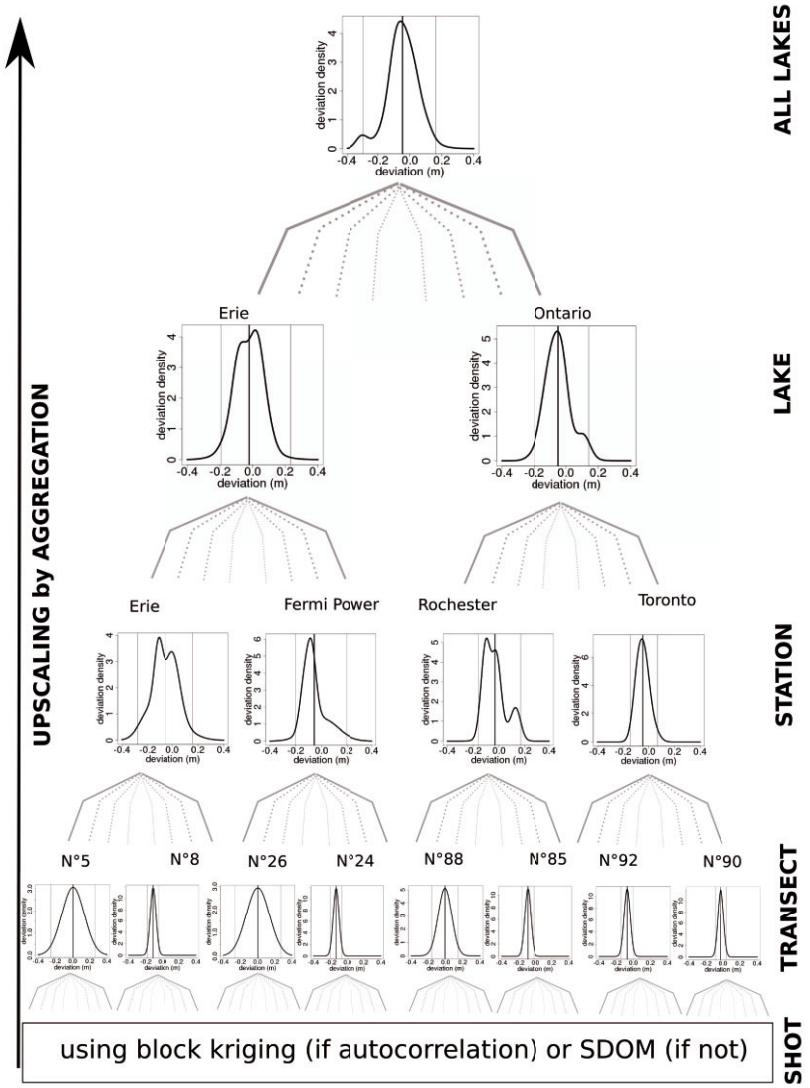

Fig 9: GLAS water elevation deviation distribution and upscaling: For transect scale (down), for station scale, for lake scale and all lake scale (up). Not all distributions for lake, station and transect scales are depicted but only examples. The black wide central line on density plots denote the biases values and the thin lines denotes the 2.5 % and 95.5 % quantiles respectively. The two examples of deviation distribution selected at transect scale for each lake are for a correlated transect (wide on the left) and a not-correlated transect (thin on the right).

5. Conclusions

This study explored the accuracy of GLAS-ICESat inland water elevation data at various spatial scales with a specific emphasis on uncertainties originating from in situ measurements and impacts of autocorrelation between successive ICESat shots, i.e. at temporal high frequencies. This study also benefited from the pre-processing of the GLAS data with the saturation correction of the GLAS waveforms and spatial filtering to avoid measurement disturbance from land-water transition effects on waveform saturation as previously observed. A set of 237 GLAS transects near the available hydrometric ground stations for four of the Great Lakes of North America was analyzed. A significant autocorrelation between successive shot elevation values was observed for 45% of the transects. This autocorrelation of an approximately 11 pulses duration seems to occur when a combination of a low transmitted energy from the GLAS instrument and bad weather with low temperature and low pressure occurs. The main consequence of this

autocorrelation is a drastic increased uncertainty (by 8 times) of the GLAS water elevation at the transect scale.

After removing the 120 transects where a linear trend was observed and assuming Gaussian uncertainties for both reference data and GLAS data upscaled at the transect scale, we derived empirical distributions on GLAS deviations at the Great Lakes, lake and station scales. At the Great Lakes scale, a bias of -4.6 cm (underestimation) and a standard deviation of 11.6 cm were computed on the various shapes of GLAS deviation distributions. However, these statistics were highly variable among the stations.

This study indicates that accuracy statistics computation is highly dependent to the assumptions made on satellite data and reference data as well. These assumptions can highly affect the computed accuracy statistics and conclusion. Even if the impact of the temporal correlation in GLAS raw data was partially smoothed by the reference data uncertainty, this can be crucial when reasoning with few data, such as a small number of transects, at the station scale.

The accuracy results of this study confirm that satellite ranging LIDAR provides data with a decimeter accuracy to monitor water level in inland water for the Great Lakes or a wide river section.

Acknowledgements

The authors would like to thank the ICESat team and the National Snow and Ice Data Centre for providing ICESat data and expertise. The authors are very grateful to EADS-Astrium and CNES, which supported this study, and especially to Frederic Fabre from EADS Astrium for his useful advices. The authors also want to thank Carmen Games-Puertas who built several useful tools for ICESat waveforms data extraction during the training period.

References

Abshire, J., Sun, X., Riris, H., Sirota, J., McGarry, J., Palm, S., Yi, D., Liiva, P., 2005. Geoscience Laser Altimeter System (GLAS) on the ICE-Sat mission: On-orbit measurement performance. Geophysical Research Letters 32(21) (21), 1–4.

Aladin, N., Crétaux, J., Plotnikov, I. S., Kouraev, A. V., Smurov, A. O., Cazenave, A., Egorov, A. N., Papa, F., 2005. Modern hydro-biological state of the Small Aral sea. Environmetrics 16 (4), 375–392.

Armstrong, M., 1984. Problems with universal kriging. Mathematical geology 16 (1), 101–108.

Atkinson, P. M., Tate, N. J., 2000. Spatial scale problems and geostatistical solutions: A review. The Professional Geographer 52 (4), 607 – 623.

Baghdadi, N., Lemarquand, N., Abdallah, H., Bailly, J. S., 2011. The relevance of GLAS/ICESat elevation data for the monitoring of river networks. Remote Sensing 3 (4), 708–720.

Bailly, J., LeCoarer, Y., Languille, P., Stigermark, C., Allouis, T., 2010. Geostatistical estimation of bathymetric LIDAR errors on rivers. Earth Surface Processes and Landforms 35 (10), 1199–1210.

Bercher, N., 2008. Précision de l'altimetrie satelittaire radar sur les cours d'eau. Ph.D. thesis, AgroParisTech.

Bhang, K. J., Schwartz, F. W., Braun, A., 2007. Verification of the vertical error in C-band SRTM DEM using ICESat and Landsat-7, Otter Tail County, MN. IEEE Transactions on Geoscience and Remote Sensing 45 (1), 36–44.

Birkett, C. M., 1995. The contribution of TOPEX/POSEIDON to the global monitoring of climatically sensitive lakes. Journal of Geophysical Research 100 (C12), 25,179–25,204.

Birkett, C. M., 1998. Contribution of the TOPEX NASA radar altimeter to the global monitoring of large rivers and wetlands. Water Resources Research 34 (5), 1223–1239.

Birkett, C. M., 2000. Synergistic remote sensing of Lake Chad: Variability of basin inundation. Remote Sensing of Environment 72 (2), 218–236.

Birkett, C. M., Mertes, L. A. K., Dunne, T., Costa, M. H., Jasinski, M. J., 2002. Surface water dynamics in the Amazon Basin: Application of satellite radar altimetry. Journal of Geophysical Research - Atmospheres 107 (D20).

Braun, A., Cheng, K. ., Csatho, B., Shum, C. K., June 2004. ICESat laser altimetry in the Great Lakes. In: Proceedings of the 60th Institute of Navigation Annual Meeting. Dayton-OH, USA, pp. 409–416.

Breiman, L., Friedman, J., Olshen, R., Stone, C., 1984. Classification And Regression Tree. London: Chapman and Hall.

Calmant, S., Seyler, F., 2006. Continental surface waters from satellite altimetry. Comptes Rendus - Geoscience 338 (14-15), 1113–1122.

Chen, Q., 2010. Assessment of terrain elevation derived from satellite laser altimetry over mountainous forest areas using airborne LIDAR data. ISPRS Journal of Photogrammetry and Remote Sensing 65 (1), 111–122.

Chen, Y., Chang, F., 2009. Evolutionary artificial neural networks for hydrological systems forecasting. Journal of Hydrology 367 (1-2), 125–137.

Chiles, J., Delfiner, P., 1999. Geostatistics: modeling spatial uncertainty. New York: John Wiley and Sons.

Chipman, J. W., Lillesand, T. M., 2007. Satellite-based assessment of the dynamics of new lakes in southern Egypt. International Journal of Remote Sensing 28 (19), 4365–4379.

Cressie, N., 1993. Statistics for spatial data. John Wiley and Sons, Inc., New York.

Crosson, W., Limaye, A., Laymon, C., 2010. Impacts of spatial scaling errors on soil moisture retrieval accuracy at L-band. IEEE Transactions on Geoscience and Remote Sensing 3 (1), 67 – 80.

Crétaux, J., Birkett, C., 2006. Lake studies from satellite radar altimetry. Comptes Rendus - Geoscience 338 (14-15), 1098–1112.

Duong, H., Pfeifer, N., Lindenbergh, R., 2006. Full waveform analysis: Icesat laser data for land cover classification. International Archives of Photogrammetry, Remote Sensing and Spatial Information Sciences 36 (Part 7), 30–35.

Harvey, K., Grabs, W., 2003. Expert meeting on hydrological data for global studies, Toronto, Canada. Tech. rep., GCOS/GTOS/HWRP.

Hovis, J., Popovich, W., Zervas, C., Hubbard, J., Shih, H. H., Stone, P., 2004. Effects of hurricane Isabel on water levels. Tech. rep., NOAA / NOS CO-OPS 040.

Jutzi, B., Stilla, U., 2006. Range determination with waveform recording laser systems using a Wiener Filter. ISPRS Journal of Photogrammetry and Remote Sensing 61 (2), 95 – 107.

Legendre, P., Fortin, M.-J., 1989. Spatial pattern and ecological analysis. Vegetatio 80 (2), 107–138.

Maheu, C., Cazenave, A., Mechoso, C. R., 2003. Water level fluctuations in the Plata Basin (South America) from Topex/Poseidon satellite altimetry. Geophysical Research Letters 30 (3), 43–1.

Mercier, F., 2001. Alimétrie spatiale sur les eaux continentales: apport des missions TOPEX/POSEIDON et ERS1&2 à l'étude des lacs, mers intérieurs et basins fluviaux. Ph.D. thesis, University Toulouse III, Paul Sabatier.

Morris, C. S., Gill, S. K., 1994. Evaluation of the TOPEX/POSEIDON altimeter system over the Great Lakes. Journal of Geophysical Research 99 (C12), 24,527–24,539.

Pebesma, E. J., Wesseling, C. G., 1998. Gstat: A program for geostatistical modelling, prediction and simulation. Computers and Geosciences 24 (1), 17–31.

Schutz, B. E., Zwally, H. J., Shuman, C. A., Hancock, D., DiMarzio, J. P., 2005. Overview of the ICESat mission. Geophysical Research Letters 32 (21), 1–4.

Smith, D. A., Roman, D. R., 2001. GEOID99 and G99SSS: 1-arc-minute geoid models for the United States. Journal of Geodesy 75 (9-10), 469–490.

Sun, X., Abshire, J. B., Yi, D., Fricker, H. A., december 2005. ICESat receiver signal dynamic range assessment and correction of range bias due

to saturation. In: EOS Trans. AGU. Vol. 86 of Fall Meet. Suppl. Abstract G21C-1288.

Touchart, L., 2002. Limnologie physique et dynamique : Une géographie des lacs et des étangs. L'Harmattan, Paris.

Urban, T. J., Schutz, B. E., Neuenschwander, A. L., 2008. A survey of ICESat coastal altimetry applications: continental coast, open ocean island, and inland river. Terrestrial, Atmospheric and Oceanic Sciences 19 (1-2), 1–19.

Wackernagel, H., 1995. Multivariate Geostatistics. Springer Verlag, Berlin.

Wagner, W., Ullrich, A., Ducic, V., Melzer, T., Studnicka, N., 2006. Gaussian decomposition and calibration of a novel small-footprint full-waveform digitising airborne laser scanner. ISPRS Journal of Photogrammetry and Remote Sensing 60 (2), 100–112.

Wesche, C., Riedel, S., Steinhage, D., 2009. Precise surface topography of the grounded ice ridges at the Ekströmisen, Antarctica, based on several geophysical data sets. ISPRS Journal of Photogrammetry and Remote Sensing 64 (4), 381 – 386.

Zhang, G., Xie, H., Kang, S., Yi, D., Ackley, S., 2011. Monitoring lake level changes on the Tibetan Plateau using ICESat altimetry data (2003-2009). Remote sensing of Envrionment 115 (7), 1733–1742.

Zwally, H. J., Schutz, B., Abdalati, W., Abshire, J., Bentley, C., Brenner, A., Bufton, J., Dezio, J., Hancock, D., Harding, D., Herring, T., Minster, B., Quinn, K., Palm, S., Spinhirne, J., Thomas, R., 2002. ICESat's

laser measurements of polar ice, atmosphere, ocean, and land. Journal of Geodynamics 34 (3-4), 405–445.

Lake	Id	Station	Number of shots used	Number of transects used	Bias (m)	Standard Deviation (m)
Erie	1	Bar Point	975	8	0.008	0.035
Erie	2	Fermi Power	1634	16	-0.057	0.102
Erie	3	Marblehead	198	2	-0.012	0.034
Erie	4	Cleveland	607	8	0.006	0.055
Erie	5	Fair Port	240	6	0.038	0.054
Erie	6	Erie	711	10	-0.058	0.112
Erie	7	Sturgeon	2148	18	-0.051	0.089
Erie	8	Port Colborne	2034	16	-0.012	0.093
Erie	9	Port Dover	287	5	-0.044	0.051
Erie	10	Port Stanley	782	9	0.028	0.061
Erie	11	Erieau	651	18	-0.038	0.059
Erie				**Mean**	**-0.021**	**0.109**
Ontario	12	Port Weller	1220	14	-0.097	0.092
Ontario	13	Rochester	979	14	-0.031	0.084
Ontario	14	Oswego	253	5	-0.140	0.034
Ontario	15	Kingston	221	5	-0.033	0.038
Ontario	16	Cobourg	1631	17	-0.028	0.074
Ontario	17	Toronto	743	8	-0.022	0.084
Ontario				**Mean**	**-0.048**	**0.087**
Michigan	18	Green bay	213	3	-0.088	0.124
Michigan	19	Kewaunee	384	4	-0.145	0.056
Michigan	20	Calumet	571	7	-0.143	0.128
Michigan	21	Holland	264	4	-0.022	0.084
Michigan	22	Ludington	425	6	-0.120	0.137
Michigan				**Mean**	**-0.114**	**0.129**
Superior	23	Ontanagon	213	15	-0.048	0.093
Superior	24	Marquette	384	8	-0.091	0.042
Superior	25	Ross Port	571	12	-0.042	0.062
Superior	26	Thunder Bay	264	5	-0.004	0.087
Superior	27	Grand Marais	425	6	0.010	0.033
Superior				**Mean**	**-0.042**	**0.079**
ALL LAKES				**Mean**	**-0.046**	**0.116**

Table 1: Left : Number of GLAS shots and transects used across each hydrometric station of the four Great Lakes; Right: biases and standard deviation of deviations (GLAS-reference) resulting from comparison between ICESat elevations and reference elevations on the Great Lakes of North America at lake and hydrometric station scales.

Chapitre 2

Modélisation des trains d’onde LiDAR sur les eaux

Chapitre 2

1. Modélisation des trains d'onde LiDAR sur les eaux

Pour évaluer le potentiel et l'analyse des performances bathymétriques des systèmes LiDAR satellitaires sur les eaux continentales et côtières, il est nécessaire de disposer d'une large base de données de formes d'onde LiDAR, représentative des différents milieux qui peuvent être rencontrés. Un modèle à base physique qui simule des formes d'ondes LiDAR a été développé dans le but et de construire une base de signaux simulés à partir de paramètres du milieu représentatives des conditions physiques de l'eau, et de différentes configurations de systèmes LiDAR. Un tel modèle-simulateur, validé par confrontation à des données observées, permettrait aussi d'explorer le gain et les limites de différentes configurations de capteurs (longueur d'onde, puissance d'émission, divergence laser, etc) dans des conditions contrôlées.

Jusqu'à ce jour, peu d'études ont été publiées sur la modélisation des formes d'onde LiDAR sur ou à travers l'eau. Dans ce chapitre, un simulateur (Wa-LiD: Water LiDAR) a été développé pour simuler les formes d'ondes LiDAR dans l'eau pour des longueurs d'onde dans le spectre visible à partir de 300nm (ultra violer) jusqu'a 1500nm (proche infra rouge). Les caractéristiques spécifiques du simulateur développé portent sur (i) la possibilité de simuler des trains ou formes d'ondes rétrodiffusées pour une longueur d'onde comprise entre 300 nm et 1500 nm, (ii) une représentation géométrique explicite des propriétés de la surface de l'eau, (iii) l'utilisation des lois de transfert radiatif dans l'eau en fonction des longueur d'ondes et de propriétés physico-chimiques de l'eau mesurées usuellement, et (iv) la modélisation du bruit issu de deux sources : le bruit interne de détecteur et le bruit dû au rayonnement solaire. Un ensemble de formes d'onde simulées a été comparé à des formes d'onde LiDAR acquises par le capteur GLAS/ICESat sur le lac Léman et par le capteur HawkEye II sur une zone côtière au nord de La Réunion (données SHOM). Les distributions des rapports signal à bruit (SNR) pour les pics de surface de l'eau et les pics de fond sont comparées pour les formes d'onde simulées et observées. Les résultats montrent que les distributions des SNR simulés par Wa-LiD

sont conformes avec les distributions des SNR observées par les deux systèmes GLAS et HawkEye.

1.1. Wa-LiD: A new LiDAR simulator for waters

Abdallah H., Baghdadi N., Bailly J.S., Pastol Y. and Fabre F., 2012. Wa-LiD: A new LiDAR simulator for waters, *IEEE Geoscience and Remote Sensing Letters,* 9 (4), 744-748.

Wa-LiD: A new LiDAR simulator for waters

Hani Abdallah[1], Nicolas Baghdadi[1], Jean-Stéphane Bailly[2], Yves Pastol[3], Frédéric Fabre[4]

[1] CEMAGREF, UMR TETIS, 500 rue François Breton, 34093 Montpellier Cedex 5, France.
[2] AgroParisTech, UMR TETIS, 500 rue François Breton, 34093 Montpellier Cedex 5, France.
[3] SHOM, CS 92803, 29228 Brest Cedex 2, France
[4] EADS – Astrium, 31 rue des cosmonautes, 31402 Toulouse Cedex 4, France
Email : hani.abdallah@teledetection.fr
Phone: +33 467548719, Fax: +33 467548700

A simulator (Wa-LiD) was developed to simulate the reflection of LiDAR waveforms from water across visible wavelengths. The specific features of the simulator include (i) a geometrical representation of the water surface properties, (ii) the use of laws of radiative transfer in water adjusted for wavelength and the water's physical properties, and (iii) modelling of detection noise and signal level due to solar radiation. A set of simulated waveforms was compared with observed LiDAR waveforms acquired by the HawkEye airborne and GLAS satellite systems in the near-infra red or green wavelengths and across inland or coastal waters. Signal-to-noise ratio (SNR) distributions for the water surface and bottom waveform peaks are compared with simulated and observed waveforms. For both systems (GLAS and HawkEye), Wa-LiD simulated SNR conform to the observed SNR distributions. Moreover, Wa-LiD showed a good ability to reproduce observed waveforms according to some realistic water parameters fitting.

***Index Terms*— Waveform model, altimetry, bathymetry, SNR, GLAS, ICESat, HawkEye**

I. INTRODUCTION

Water surface altimetry and bathymetry are key variables for many applications in hydrology, geomorphology and meteorology (e.g., [1], [2]). Several techniques for measuring water altimetry and bathymetry have been developed through the use of sonar, radar and optical imaging. Each of these techniques has drawbacks when used on inland or coastal waters [3], including (i) limited spatial coverage and use on navigable rivers (sonar), (ii) a large radar footprint when used for inland water, especially rivers and (iii) the lack of the use of optical imaging in unclear waters.

Airborne hydrographic LiDAR has proved to be a suitable sensor because of its accuracy and high spatial density features [4]. The potential for airborne hydrographic LiDAR is that it can be used for both altimetry and bathymetry because of the ability of LiDAR detectors to register returned signals from (i) the water surface for altimetry [5], (ii) the water bottom for bathymetry ([6], [7]), and (iii) the water column that allows some optical properties of water to be deduced [8]. The Airborne Hydrographic LiDAR technique is limited in terms of spatial coverage and because the data is expensive to gather.

ICESat has been the only altimeter LiDAR satellite up to now. The Geoscience Laser Altimeter System (GLAS) from ICESat provides accurate high resolution elevations for altimetry. The GLAS is promising for inland areas with widths greater than 1.5 km, even though the footprint is small (50 to 90 m), because of the time needed for detector gain adaptation when transitioning from land to water (0.25 s, approximately 1.5 km). The transition phase from land to water limits the use of GLAS in small, inland water areas [9].

To improve the prospective and the performance analysis in satellite LiDAR systems designed for water altimetry and bathymetry, a LiDAR signal database representative of the possible physical conditions of water using different LiDAR configurations is needed. The common procedure to obtain a database involves the development of a physical model simulating the signals. Such a model would allow the reproduction of the LiDAR signal regardless of the water and instrumental parameters.

Most hydrographic applications that use LiDAR signals are derived from the work of Guenther [5]. Before now, few studies have been published that model LiDAR waveforms on water; these studies include (i) the simulation model of Mclean [10], which generates LiDAR returned waveforms from a wind-roughened ocean, (ii) the work of Feigels [6] on the optimisation of airborne LiDAR's parameters through modelling and analysing waveforms and (iii) work on modelling sea surface return and laser bathymetry from airborne LiDAR [7].

The objective of this study is to develop a new waveform simulation model available for any laser wavelength in the optical spectrum domain from 300 (Ultra Violet, UV) to 1500 nm (Near Infra Red, NIR). This model is similar to other Hydrographic LiDAR models (e.g., [5], [6], [7]) except it integrates radiative transfer laws governed by the physical properties of water for any wavelength. This simulation model uses a geometrical representation of the water surface with the geometric model of Cook and Torrance [11] and integrates both the characteristics of detection noise and signal level due to solar radiation. However, this model does not take into account the pulse spreading due to multiple scattering from suspended organic and inorganic particulates in the water column; but it integrates the modelling for pulse stretching due to the surfaces geometry.

The aim of this paper is (i) to present the water LiDAR waveform model (Wa-LiD) formulae regardless of LiDAR system parameters and water parameters, (ii) to exhibit a selection of simulated waveforms for certain wavelengths and the same water characteristics (iii) to compare the SNR of simulated waveforms to observed LiDAR waveforms from the satellite GLAS sensor and the airborne HawkEye sensor and (iv) to present a qualitative comparison between observed and fitted simulated waveforms.

II. LIDAR MODELLING

A. The Water LiDAR (Wa-LiD) Simulation Model

1) Model description

The Wa-LiD model is able to simulate waveforms for any laser wavelength in the optical spectrum domain from 300 to 1500 nm regardless of the optical properties of water. These optical properties are determined by the attenuation (absorption + scattering) of optical

light by pure water, yellow substances, phytoplankton and sediment (e.g., [12], [13]). In addition, this Wa-LiD model (i) takes into account any Bragg-scattering from the water surface using the geometric (facets) model of Cook and Torrance [11] and (ii) integrates the effects of detector noise and noise due to solar radiation.

The waveforms received by the LiDAR system (power as a function of time) are written as the sum of the echoes of multiple waves [7]:

$$P_T(t) = P_s(t) + P_c(t) + P_b(t) + P_{bg}(t) + P_N(t) \quad (1)$$

Where $P_T(t)$ is the total power received, $P_s(t)$ is the power returned by the water surface, $P_c(t)$ is the power returned by the water column, $P_b(t)$ is the power returned by the bottom, $P_{bg}(t)$ is the background power returned by the air column, $P_N(t)$ is the detector noise power and t is the time scale.

The emitted laser pulse from the LiDAR system is considered to be a Gaussian distribution [14]:

$$w(t_x) = \frac{2}{T_0}\sqrt{\frac{ln2}{\pi}}\, exp\left(-4ln2\frac{(t-t_x)^2}{T_0{}^2}\right) \quad (2)$$

Where t_x is the two-way time delay of the emitted Gaussian pulse between the detector and the water surface t_s, water column t_c or bottom t_b. The returned waveforms from the water surface, water column and bottom correspond to the convolution of the Gaussian emitted pulse and the instant echoes from the water surface P_s, water column P_c and bottom P_b.

Returned waveform from water surface:

The returned waveform from the water surface received by the LiDAR detector $P_s(t)$ is given by: $P_s(t) = w(t_s) * P_s$, with:

$$P_S = \frac{P_e T_{atm}^2 A_R \eta_e \eta_R L_S \cos^2(\theta)}{\pi H^2} \quad (3)$$

P_e is the emitted power by laser = E_0/T_0, E_0 is the emitted energy of the LiDAR system, T_0 is the Gaussian FWHM (Full Width at Half Maximum), T_{atm}^2 is the two way atmospheric loss, A_R is the receiver area, η_e and η_R are the optical efficiencies of emission and reception, L_S is the loss of transmission through the surface (surface albedo), θ is the local incidence angle, H is the sensor altitude, $t_s = \frac{2H}{c\cos(\theta)}$, and c is the velocity of light in air.

The loss factor through the surface L_S is calculated by the BRDF (Bidirectional Reflectance Distribution Function) of the water surface represented by specular microfacets using the geometric model of Cook and Torrance:

$$L_S = \frac{k_d}{\pi} + \frac{k_s DOF_r}{\pi \cos^2\theta} \quad (4)$$

k_d and k_s ($k_d = 1 - k_s$) determine the fraction of diffuse and specular components, respectively. D is the microfacet distribution function that models the surface as geometric facets and is described by the distribution function of Beckmann [15].

$$D = \frac{1}{r^2 \cos^4\theta} e^{(tan\theta/r)^2} \quad (5)$$

r is the *rms* (root mean square) slope of the facets, which determines the surface roughness. Small values of r signify gentle facet slopes and give a distribution that is highly directional around the specular component while large values of r imply steep facet slopes and give a distribution that is spread out [11].

O is the geometric attenuation factor of the BRDF that takes into account the phenomenon of masking between facets (auto-shadowing). F_r is the function that describes the Fresnel reflection of light on each microfacet.

Returned waveform from water column

The returned waveform from the water column $P_C(t)$ at a depth z is given by: $P_c(t) = w(t_c) * P_c(z)$, with:

$$P_c(z) = \frac{P_e T_{atm}^2 A_R \eta_e \eta_R F(1-L_s)^2 \beta(\varphi) exp\left(\frac{-2kz}{\cos\theta_w}\right)}{\left(\frac{n_w H + z}{\cos\theta}\right)^2} \quad (6)$$

θ_w is the local incidence angle in the water, F is a loss factor due to the field of view of the telescope, n_w is the water refractive index, $\beta(\varphi)$ is the volume scattering function, z is the column layer, $t_c = t_s + \frac{2z}{c_w \cos\theta_w}$ with c_w as the velocity of light in water, and k is the diffuse attenuation coefficient and is defined by the degradation rate of light with depth. An empirical relationship was established by Guenther [5] between the diffuse attenuation and the optical properties of water in using experimental data:

$$k = c(\lambda)[0.19(1-\omega_0)]^{\frac{\omega_0}{2}} \quad (7)$$

Where $\omega_0 = b(\lambda)/c(\lambda)$ is the single scattering albedo, $b(\lambda)$ is the scattering coefficient, $c(\lambda)=a(\lambda)+b(\lambda)$ is the attenuation coefficient and $a(\lambda)$ is the absorption coefficient.

The optical properties ($a(\lambda)$,$b(\lambda)$) of turbid water are then expressed as the sum of contribution from different substances in water, such as yellow substances, phytoplankton and sediment [13], where:

$$a(\lambda) = a_w(\lambda) + a_y(\lambda) + a_{ph}(\lambda) + a_s(\lambda) \quad (8)$$

$$b(\lambda) = b_w(\lambda) + b_{ph}(\lambda) + b_s(\lambda) \quad (9)$$

Where w, y, ph and S are the indices of pure water, yellow substances, phytoplankton and sediments, respectively.

Returned waveform from water bottom

The returned waveform from the water bottom received by the LiDAR detector $P_b(t)$ is defined as: $P_b(t) = w(t_b) * P_b$, with:

$$P_b = \frac{P_e T_{atm}^2 A_R \eta_e \eta_R F(1-L_s)^2 R_b\, exp\left(\frac{-2kZ}{\cos\theta_w}\right)}{\pi\left(\frac{n_w H + Z}{\cos\theta}\right)^2} \quad (10)$$

Where Z is the bathymetry, R_b is the bottom albedo (or bottom reflectance) and $t_b = t_s + \frac{2Z}{c_w \cos\theta_w}$

Signal level due to solar radiation

The signal level due to solar radiation is defined as a Gaussian white noise with a mean of zero and a standard deviation equal to 1 convolved by the instant echo, P_{bg}:

$$P_{bg} = I_S A_R T_{atm}^2 (1-\gamma_r^2)\frac{\pi\theta^2}{4}\Delta_\lambda \eta_R \quad (11)$$

Where I_s is the solar radiance reflected from the water column, Δ_λ is the bandwidth of the optical filter in the receiver and γ_r is the receiver obscuration ratio.

Receiver internal noise

The detector internal noise is defined as a normal distribution with a zero mean and a standard deviation $\sigma_N(t)$ that varies according to the signal level:

$$\sigma_N(t) = \frac{\sqrt{2eB(P_{ext}(t)G + I_d)}}{R_\lambda} \quad (12)$$

Where $P_{ext}(t) = P_{bg}(t) + P_s(t) + P_c(t) + P_b(t)$, e is the electron charge (1.6 x 10^{-19} C), B is electrical bandwidth of the detector, G is the excess noise factor, I_d is the dark current and R_λ is the responsivity.

Geometric pulse stretching modelling

The laser pulse stretching caused by the geometric effects between the laser beam and the target requires a modelling procedure. This modelling is applied for each LiDAR return components (P_c, P_s, and P_b). Indeed, the emitted laser pulse is reflected first from the portion of the target closest to the sensor (short path) and then from the portion farther (long path). For the surface return, t he time delay difference (Δt) between the long and the short path is given by Guenther [5]:

$$\Delta t = \frac{2H}{c}\left[\frac{1}{\cos(\theta+\gamma/2)} - \frac{1}{\cos(\theta-\gamma/2)}\right] \quad (13)$$

Where γ, is the beam divergence angle. The time difference Δt modifies the pulse width by stretching it with a τ value. For $\Delta t<2T_0$, $\tau=0.1\Delta t$ and for $\Delta t > 2T_0$, $\tau = T_0\left(\frac{0.5\Delta t}{T_0} - 0.4\right)$. The returned pulse width from water bottom will be equal to $T_0 + \tau$.

For the bottom, equation (13) is applied in replacing θ by θ_w, and H by $H+Z$.

2) Wa-LiD simulation examples

Figure 1 shows simulated waveforms in the case of a satellite LiDAR sensor at an altitude of 500 km, emitting NIR (1064 nm), green (532 nm), and UV (350 nm) wavelengths. Water characteristics used in this simulation correspond to river water conditions with an average turbidity (average concentration of yellow substances a_{y0} = 0.86 m^{-1}, phytoplankton C_{ph} = 4 mg/m3 and sediment S = 2.8 mg/l) and a 2 m depth. The NIR signal has the highest amplitude from the surface and penetrates a few cm into the water column. The green signal penetrates deeper into the water column and, depending on the water properties, is reflected from the bottom. The UV wavelength penetrates considerably through the water column and can reach the bottom, but the response is very low.

III. COMPARISON OF SIMULATED TO OBSERVED WAVEFORMS

Simulated waveforms are compared with observed LiDAR waveforms to identify the Wa-LiD model behaviour. The available observed data were provided from the satellite GLAS sensor and the airborne HawkEye sensor (© SHOM). As the water properties at survey time are unknown (surface roughness, water depth, sediment concentration, bottom slope, etc), the signal to noise ratios distribution for observed and simulated waveforms and few demonstrative observed and simulated waveforms will be presented to illustrate the performance of the Wa-LID simulator.

A. Observed waveforms Datasets

Two datasets were available. The first dataset contains waveforms acquired by the Geosciences Laser Altimeter System (GLAS) across the Lake Leman located in Switzerland and France (Lat. 46°26'N and Long. 6°33'E, Figure 2a). Lake Leman is one of the largest lakes in Western Europe with a surface area of 582 km². The maximum length and width of the lake are 73 km and 14 km, respectively. The relatively flat surfaces and the fact that the lake is not affected by tides make this a good location for validation studies. The GLAS data used in this study are GLA01. The GLA01 data include waveforms echoed from the water surface in NIR (1064 nm). Each waveform was sampled in 544 or 1000 bins of received power in volts at a sampling rate of 1 ns over land area [16]. In this study, two GLAS transects (set of successive shots or footprints) were selected. Waveforms from these two transects do not have saturation problems and are longer than other transects. The first transect was taken on March 4th 2005 with a length of 11.5 km and corresponds to 69 shots; the second transect was taken on June 7th 2006 with a length of 10.5 km and a corresponding 61 shots.

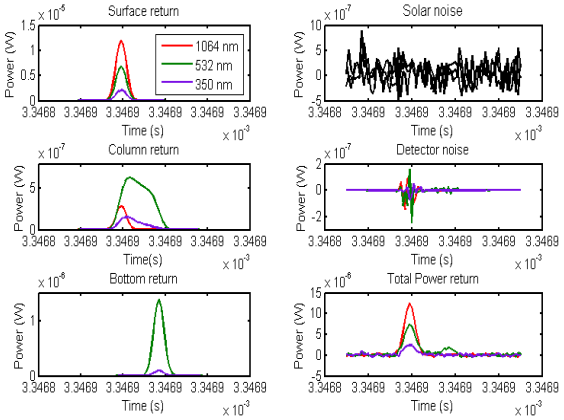

Fig. 1. Simulated LiDAR Waveforms in NIR (1064 nm), green (532 nm), and UV (350 nm). E_e=20 mJ, T_0=5 ns, θ=0.3°. Water is of average turbidity (a_{y0}=0.86 m-1, C_{ph}=4 mg/m3, S=2.8 mg/l) with a depth of 2 m.

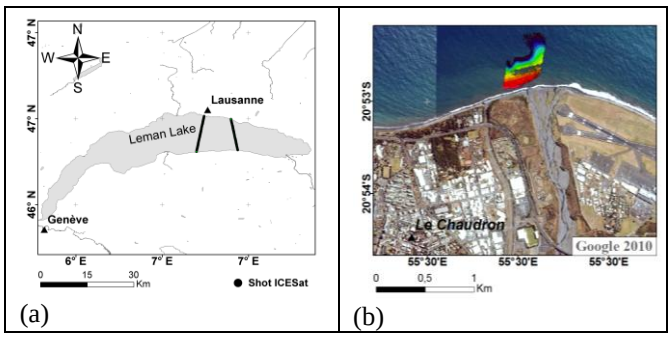

Fig. 2. (a) GLAS transects over Leman Lake, (b) HawkEye points across a coastal area in the northern part of Reunion Island.

The second dataset contains waveforms registered by the airborne HawkEye system across a coastal area in the northern part of Reunion Island near le Chaudron (Lat. 20°52'S and Long. 55°30'E, Figure 2b). The HawkEye LiDAR consists of two laser scanners, one green (532 nm) and one infrared (1064 nm) [17]. The infrared laser light is reflected at the water surface whereas the green laser light continues into the water column. The green laser light is reflected at the seabed, and a portion of the reflected light is collected by the receiver.

Table 1 shows the characteristics of the two LiDAR systems, GLAS [16] and HawkEye [7].

B. Simulated waveforms datasets

Table 2 shows the range of water parameters used for these simulations. A range of probable values of water parameters is used for the simulation because the exact water properties were not precisely

known at the time of the survey; in some cases, it was impossible to measure some of the properties, such as water surface roughness. The range of roughness, *r*, values used are from Beckman and Spizzochino [15]. The range of sediment concentration for coastal areas varies from 2.6 for clear water to 200 mg/l for very turbid water [18]. Here, we used a smaller range (2.6–10 mg/l) corresponding to clear water. In the same way, as sand in this area is black and formed as a result of volcanic activity [19], the selected range of values for bottom reflectance (Table 2) is the same used by Jun et al. [20].

TABLE 1: THE GLAS AND HAWKEYE SYSTEMS PARAMETERS USED IN SIMULATIONS

Parameters	GLAS	HawkEye	Parameters	GLAS	HawkEye
λ (nm)	1064	532-1064	η_e	0.8	0.9
H	600 km	200 m	η_R	0.5	0.5
E_0 (mJ)	75	3	F	1	1
T_0 (ns)	5	7	Δ_λ (nm)	1.2	1
θ (°)	0,3	20	γ_r	0.1	0.35
A_R (m²)	0,8	0,025	B (MHZ)	100	142
FOV (mrad)	5	30	G	3	3
R_λ (A/W)	0.25	0.3	Id (A)	10^{-10}	10^{-8}
γ (mrad)	0.11	15			

TABLE 2: RANGE OF ENVIRONMENTAL PARAMETERS USED IN SIMULATIONS

Parameters	Range	Parameters	GLAS	HawkEye
r	[0.1–0.5]	T^2_{atm}	0.64	0.9
S (mg/l)	[2.6–10]	$\beta(\varphi)$ ($m^{-1}sr^{-1}$)	0.0014	0.0014
R_b	[0.05–0.2]	I_s (w/m²srnm)	0.025	0.025
k_s	0.9	n_w	1.33	1.33
		τ (ns)	0.2	0.8

C. Simulated-observed waveforms comparison

The amplitude of GLAS waveforms is in volts whereas the units for HawkEye are not known because of industrial trade secrets. For the Wa-LiD simulations, the waveforms are expressed in watts. For these reasons as well as the invariant shapes of waveforms and the fact that peaks in waveforms are the main information retrieved, the chosen method to compare simulated and observed waveforms was 1) the signal-to-noise ratio (*SNR)* distribution and 2) the fitting of simulated waveforms to some observed ones according to unknown parameters adjustments. Here, *SNR* is defined by the ratio between the waveform peak amplitude (water surface, bottom) and the standard deviation of detection noise (includes also the photon noise of the useful signal). The distributions of SNR for simulated and observed waveforms were computed. The 95%, 90%, 75% and 50% confidence intervals were thus calculated from SNR quantiles for both observed waveforms (GLAS and HawkEye) and simulated ones. Next, the probabilities for an observed SNR to belong to a given simulated SNR confidence interval were computed and conversely.

D. Results and discussion

1) Simulated-observed GLAS SNR Comparison

Waveforms were simulated from Wa-LiD using the GLAS system parameters (Table 1) and the range of values for roughness *r* (Table 2). In the infrared, the waveforms are influenced mainly by the water surface roughness because the penetration of this wavelength is very low in the water column and the LiDAR return comes primarily from the water surface. In all, 260 waveforms were generated by random, and water surface properties were uniformly selected within the ranges given in Table 2. From the two GLAS transects selected, 130 GLAS waveforms across Leman Lake were used. Next, GLAS and simulated SNR distributions were computed and assigned confidence intervals. The probability of a GLAS SNR (SNR_{GLAS}) value belonging to the simulated SNR (SNR_{walid}) confidence intervals is high (Figure 3) (approximately 0.99 at a 95% confidence interval). In the Wa-LiD model, the water surface albedo (L_s) is influenced by two water surface properties: the specular reflection coefficient and the surface roughness. The underestimation of the simulated SNR is probably due to the distribution of unknown water properties compared with simulations from distributions of uniform water properties.

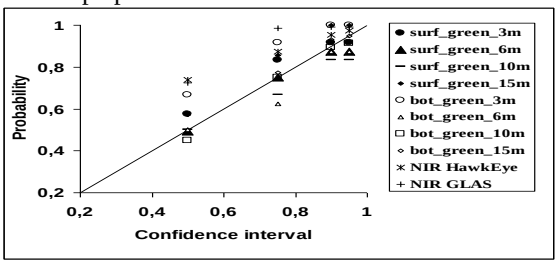

Fig. 3. Probability of an observed SNR to belong to a simulated SNR interval.

2) Simulated-observed GLAS HawkEye Comparison

NIR channel

In all, 400 waveforms were simulated from Wa-LiD using the HawkEye system characteristics (Table 1) and a wide range of values for water surface roughness (Table 2). They were compared to 200 observed HawkEye waveforms. The probability of HawkEye SNR (SNR_{Hawk}) belonging to SNR_{walid} confidence intervals is high (Figure 3). The weak underestimation of simulated SNR may result for the same reason as the underestimation for GLAS (i.e., unknown values of properties for actual surface water distribution), which may demonstrate the limitations of this comparison exercise. This result confirms the capability of the Wa-LiD model to simulate realistic LiDAR waveforms in the NIR.

Green channel

The simulated waveforms in the green were carried out using the same system parameters as those for the infrared, except for the wavelength value (532 nm). The water parameters (Table 2) were randomly selected as inputs for the simulator. The water surface roughness *r* has a higher impact on the surface echo, and the sediment concentration *S* has the higher impact on the water column echo for coastal areas [18]. In contrast, the bottom reflectance R_b has the higher impact on the bottom echo. The remaining water parameters were fixed for values that belong to clear coastal water (**a_{y0}=0.1 m^{-1}, C_{ph}=1 mg/m^3). The comparison between HawkEye and simulated waveforms were carried out for 4 water depths: 3, 6, 10, and 15 m. For each depth, 400 simulations were generated. For comparison, 94 HawkEye waveforms were used: 21 at 3 m, 20 at 6 m, 20 at 10 m, and 18 at 15 m depths.

HawkEye and simulated data were compared using the SNR for both the surface and bottom returns. The same confidence intervals were calculated for each considered bathymetry. There is a high probability (higher than 0.8) that the HawkEye surface SNR (SNR_{Hawk}) belong to the simulated surface SNR 95% confidence interval for all water depths (Figure 3). At the bottom, the probabilities of HawkEye SNR (SNRHawk) to belong to the simulated bottom SNR confidence intervals were slightly high (Figure 3). This weak underestimation of simulated SNR (surface and bottom) is thought to

be a result of the unknown actual distribution of 95% at the surface (k_s, r), the column (S) and the bottom (R_b), which does not fully match the distribution of uniform water properties for the simulation.

3) Qualitative comparison of simulated waveform fitted to observed waveforms.

As the waveforms amplitude units are different, the simulated waveforms are scaled to match the observed waveforms using a homothetic transformation. First, the exhibited HawkEye waveform in Figure 4a corresponds to a water depth about 10 m (calculated from time delay between surface peak and bottom peak). For comparison, three waveforms were simulated in the 532 nm using the HawkEye system characteristics, with different water depths and bottom slopes in order to fit the observed waveform. The observed waveform is well fitted with a depth and bottom slope of 10 m and 14°, respectively. Secondly, waveforms were simulated in the Infrared (1064 nm), using the GLAS system characteristics and compared to an observed waveform acquired across the Leman Lake (Figure 4b). In the infrared, the waveforms are influenced by the water surface roughness (r) and three waveforms were simulated with different values for roughness r. The observed waveform is well fitted with an r-value of 0.1. The comparison between observed and simulated waveforms shows the ability of the Wa-LID simulator to reproduce observed waveforms and the potential to use this simulator to retrieve unknown water parameters (Figure 4).

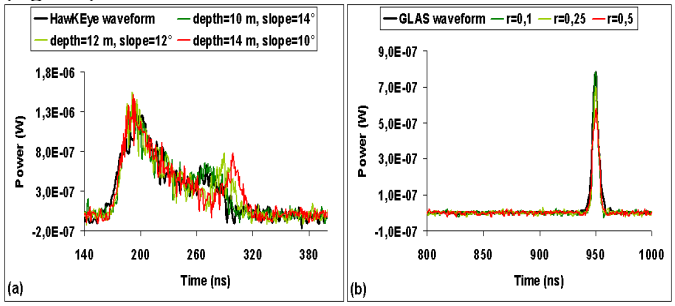

Fig.4. Comparison between observed waveforms (Hawkeye and GLAS) and three simulated waveforms. (a): Hawkeye for different water depths and bottom slopes, (b): GLAS for different roughness values.

IV. CONCLUSION

A simulation model and code was built in order to simulate LiDAR waveforms on waters for any emitted wavelength in the optical domain and for different systems characteristics and water properties. The behaviour of the simulator was explored using datasets of observed waveforms collected from the GLAS satellite sensor over Leman Lake in the NIR channel and from the HawkEye airborne sensor in a coastal area across the northern part of Reunion Island in the NIR and the green channels. The observed and simulated waveforms were analysed by comparing conformed the SNR distribution of their peaks and their confidence intervals, for surface and bottom peaks. In addition, the Wa-LiD model showed a good ability to simulate correctly the observed waveforms in using unknown adjusted water parameters. In future works, experiments and research are necessary for a proper characterisation of water surface roughness. Moreover, an analysis of the model sensitivity to different media characteristics and sensor parameters will be carried out to analyse the influential parameters and to assess the performance of future LiDAR systems for the water surface altimetry and bathymetry especially for what concerns the optimisation of the ground processing algorithms.

ACKNOWLEDGMENT

The authors would like to thank the NSIDC (National Snow and Ice Data Centre) and the SHOM (Service Hydrographique et Océanographique de la Marine) for providing GLAS and HawkEye data respectively. The authors are very grateful to EADS (European Aeronautic Defence and Space company) and CNES (Centre National d'Etudes Spatiales) which both supported this study.

REFERENCES

[1] J. K. Willis, Fu. Lee-Lueng, E. Lindstrom, and M. Srinivasan, "17 years and counting: Satellite altimetry from research to operations," *Geoscience and Remote Sensing Symposium (IGARSS), 2010 IEEE International*, pp.777-780, 2010.

[2] J. L. Irish, and W. J. Lillycrop, "Scanning laser mapping of the coastal zone: the SHOALS system," ISPRS Journal of Photogrammetry and Remote Sensing, vol. 54, no. 2-3, pp. 123-129, 1999.

[3] D. Feurer, J. S. Bailly, C. Puech, Y. LeCoarer, and A. Viau, "Very high resolution mapping of river immersed topography by remote sensing," *Progress in Physical Geography*, vol. 32, no. 4, pp. 1–17, 2008.

[4] J. S. Bailly, Y. Le Coarer, P. Languille, C. J. Stigermark, and T. Allouis, "Geostatistical Estimations of bathymetric LIDAR errors on rivers," *Earth Surface Process and Landforms*, vol. 35, pp. 1199-1210, 2010.

[5] G.C. Guenther, "Airborne Laser Hydrography, system design and performance factors," *NOAA Professional Paper Ser. NOS1* (National Oceanic and Atmospheric Administration, Rockville, Md.), 1985.

[6] J. Feigels, "LIDARs for oceanological research: criteria for comparison, main limitations, perspectives," *Ocean Optics XI*, vol. 1750, pp. 473–484, 1992.

[7] H. M. Tulldahl and K. O. Steinvall, "Simulation of sea surface wave influence on small target detection with airborne laser depth sounding," *Applied Optics*, vol. 42, no. 12, pp. 2462 – 2483, 2004.

[8] A. Collin, P. Archambault and B. Long, "Mapping the shallow water seabed habitat with the shoals," *IEEE Transactions on Geoscience and Remote Sensing*, vol. 46, no. 10, pp. 2947-2955, 2010.

[9] N. Baghdadi, N. Lemarquand, H. Abdallah, and J. S. Bailly, "The relevance of GLAS/ ICESat elevation data for the monitoring of river networks," *Remote Sensing*, vol. 3, pp. 708–720, 2011.

[10] J. W. McLean, "Modeling of ocean wave effects for lidar remote sensing," *Ocean Optics X, R. W. Spinrad, ed., Proc*, vol. 1302, pp. 480–491, 1990.

[11] R. L. Cook, and K. E. Torrance, "A Reflectance Model for Computer Graphics," *ACM Transactions on Graphics*, vol.1, pp. 7 – 24, 1982.

[12] A. Bricaud, A. Morel and L. Prieur, "Absorption by dissolved organic matter of the sea (yellow substance) in the UV and visible domains," *Limnology and Oceanography*, vol. 26, no. 1, pp. 43-53, 1981.

[13] C. D. Mobley, *Light and Water: Radiative Transfer in Natural Waters*, Academic, San Diego, Calif, 1994.

[14] B. Jutzi, and U. Stilla, "Range determination with waveform recording laser systems using a Wiener Filter," *ISPRS Journal of Photogrammetry and Remote Sensing*, vol. 61, no. 2, pp. 95–107, 2006.

[15] P. Beckmann, and A. Spizzochino, *The scatter of electromagnetic waves from rough Surfaces*, Norwood, MA: Artech House, 1987.

[16] H. J. Zwally, B. Schutz, W. Abdalati, J. Abshire, C. Bentley, A. Brenner, J. Bufton, J. Dezio, D. Hancock, D. Harding, T. Herring, B. Minster, K. Quinn, S. Palm, J. Spinhirne, and R. Thomas, "ICESat's laser measurements of polar ice, atmosphere, ocean, and land," Journal of Geodynamics, vol. 34, no. 3-4, pp. 405-445, 2002.

[17] A. Wehr and U. Lohr, "Airborne laser scanning-an introduction and overview," ISPRS Journal of Photogrammetry and Remote Sensing, vol. 54, no. 1-2, pp. 68–82, 1999.

[18] J. A. Warrick, L. A. K. Mertes, D. A. Siegel, and C. Mackenzie, "Estimating suspended sediment concentrations in turbid coastal waters of the Santa Barbara Channel with SeaWiFS" International Journal of Remote Sensing, vol. 25, pp. 1995-2002, 2004.

[19] D. Lorion, "Endiguements et risques d'inondation en milieu tropical. L'exemple de l'île de la Réunion," Norois, vol. 201, no. 4, pp. 45-66, 2006.

[20] B. Jun, K. Gotoh, H., Kitamura, and H. Koh, "Influence of phytoplankton pigments and bottom features for water quality and depth estimation," Geoscience and Remote Sensing Symposium, vol. 2, pp. 488-490, 1993.

Chapitre 3

Potentiel des futurs capteurs spatiaux LiDAR pour la bathymétrie dans les eaux continentales et côtières

Chapitre 3

1. Potentiel des futurs capteurs spatiaux LiDAR pour la bathymétrie dans les eaux continentales et côtières

L'objectif de ce chapitre est de répondre à la question suivante: Quel serait le potentiel de futurs capteurs LiDAR satellitaires pour la bathymétrie des eaux de surfaces continentales et côtières?

Pour atteindre l'objectif, la capacité des configurations de LiDAR spatiaux a été évaluée pour estimer la bathymétrie à l'échelle mondiale sur les eaux continentales et côtières. Cette évaluation est fondée sur une méthodologie basée sur un plan d'expérience de trains d'onde simulés utilisant le simulateur de forme d'onde Wa-LID présenté dans le chapitre précédent. Ce plan d'expérience est aléatoire (quasi-Monte Carlo). Il utilise des distributions statistiques de paramètres de l'eau considérées comme représentatives à l'échelle mondiale et suivant une diversité de profondeurs d'eau testées. Un processus d'identification simple de la faisabilité de la mesure de la bathymétrie (détection de pics) est développé. Puis, une méthode d'inversion (approximation par des fonctions mathématiques des contributions surface, colonne et fond du signal LiDAR) est appliquée à chaque forme d'onde pour estimer la bathymétrie. Les probabilités de mesure de bathymétrie ont ainsi été estimées pour les eaux côtières, les lacs peu profonds, les lacs profonds et les rivières qui présentent des distributions différentes pour certains paramètres des eaux. Suite à une analyse de sensibilité qui permet d'identifier les paramètres de l'eau qui ont influent le plus sur l'écho provenant du fond de l'eau (les paramètres de la colonne d'eau et la pente du fond), une cartographie de la probabilité de détection bi-paramètre est proposée au croisement des paramètres les plus influents. Cette cartographie permet aussi d'identifier les valeurs seuils des paramètres au delà desquels la bathymétrie n'est plus possible. Ensuite pour les trains d'onde ou la bathymétrie est possible, la précision d'estimation par inversion des formes d'onde est calculée.

Seules, deux configurations de capteurs LiDAR spatiaux ont été explorées ici : un LiDAR dans l'ultraviolet (355 nm) à faible énergie émise (15 mJ) et petite empreinte (8 m) et un autre dans le vert (532 nm) à faible énergie émise (5 mJ) et grande

empreinte (30 m), étant tous deux conformes aux réglementations sur la sécurité oculaire. Les configurations ont été testées pour 5 types d'eaux (eaux côtières, lacs peu profonds, lacs profonds, rivières) et 6 profondeurs (1, 2, 5, 10 et 15 m).
Les résultats des analyses de sensibilité montrent que trois paramètres dominent la contribution du fond dans les trains d'onde enregistrés. Ces paramètres sont tous liés à des propriétés de la colonne d'eau: concentration en sédiments, concentration en substances jaunes (matières organique dissoutes et colorées ainsi que des particules détritiques) et concentration en phytoplanctons. La pente du fond est un autre paramètre qui joue fortement sur les formes d'ondes et sur l'estimation de la bathymétrie : Pour des pentes importantes, l'écho de fond est fortement étiré et sa largeur devient plus grande (environ 70 ns pour une pente de 35 °).

Les probabilités de réaliser une mesure de bathymétrie ont été estimées. Par exemple, en eaux côtières, en moyenne 26 % des trains d'ondes permettent la mesure de bathymétrie pour le LiDAR vert. Tandis que pour l'UV le pourcentage diminue à 10 %. Avec le LiDAR UV. Les probabilités de détection pour le LiDAR UV sont bien sûr toujours inférieures à ceux du LiDAR vert. Les seuils des paramètres limitant la bathymétrie sont aussi identifiés. Par exemple, à une profondeur de 1 m sur les eaux côtières et pour un LiDAR vert, la bathymétrie ne peut pas être effectuée lorsque la concentration de sédiments est supérieure à 76 mg/l. Cependant à 10 m, il est impossible de mesurer la bathymétrie pour une concentration en sédiment supérieure à 3,1 mg/l.
La précision sur la bathymétrie estimée pour les deux capteurs LiDAR est de l'ordre de 2,8 cm (écart type) avec un faible biais (sous-estimation d'environ 0.5 cm) pour tous les types d'eau. Les résultats de précision sont liés seulement aux erreurs d'estimation provenant de la méthode d'inversion des trains d'onde. D'autres sources d'erreur ont été négligées. Ces erreurs proviennent en général du positionnement GPS du satellite, de la géométrie du faisceau laser et des conditions atmosphériques.

Contrainte: sûreté oculaire

La sûreté oculaire contre les rayonnements laser présente une limite principale définie par l'Exposition Maximale Permise (EMP) exprimée en Joules par m². L'EMP a été définie à partir de la norme européenne NF EN 60825-1/A2 de la Commission

Electrotechnique Internationale (CEI) (ICNIRP, 1997 ; ICNIRP, 2000 ; IEC, 2001) et représente le niveau maximal de rayonnement laser auquel les personnes peuvent être exposées sans subir de dommage immédiat ou à long terme. Cette exposition maximale permise est établie à partir des valeurs limites de densité d'énergie ou de puissance surfacique. Ainsi, les niveaux d'EMP ont été calculés en fonction de la longueur d'onde du rayonnement et du largueur du pulse. Le calcul de l'EMP est détaillé comme suit pour les longueurs d'onde allant de l'UV (315 nm) au rouge (700 nm)

1. $EMP\ (J/m^2) = 5600\ T_0^{0,25}$ pour des longueurs d'onde entre 315 et 400 nm et pour des pulses lasers ayant un largueur T_0 (en seconde) entre 10^{-9} et $10^{=7}$ secondes.
2. $EMP\ (J/m^2) = 5.10^{-3}\ C$ pour des longueurs d'ondes entre 400 et 700 nm. *C* est un facteur de correction qui vaut 1 pour des pulses lasers ayant une largueur entre 10^{-7} et 10^{-9} s.

Si on prend comme exemple les deux configurations explorées dans le chapitre suivant, i.e. dans l'UV (355 nm, T_0 =3 ns) et dans le vert (532 nm, T_0 =3.5 ns), on obtient une EMP= 41.4 mJ/m^2 pour l'UV et EMP= 5 mJ/m^2 pour le vert.

L'énergie maximale autorisée (E en Joules) qui respecte les normes de sûreté oculaire en fonction de l'EMP et de la taille du spot laser s'écrit comme suit (NF EN 60825-1/A2):

$$E \leq \frac{EMP}{T_{atm.} M_{scint} M_{gauss} \frac{4}{\pi D^2} G^2} \quad (1)$$

Tel que:

$T_{atm.}$ est la transmitance atmosphérique

M_{scint} = 2 est la marge pour scintillation atmosphérique

M_{gauss} = 4.6 est la marge pour faisceau gaussien (facteur de surintensité au centre d'un faisceau gaussien)

D est le diamètre du spot calculer à partir de l'angle de divergence γ (rad) et de l'altitude de capteur H, avec D=H.tan(γ)

G = 13,34 est le grossissement des jumelles utilisées par l'observateur au sol (pupille des jumelles de 80 mm pour un œil de pupille 6 mm selon la norme de sureté oculaire)

Sachant que les largeurs des pulses (T_0) de la plupart des capteurs LiDAR sont entre 3 et 12 ns (Baltavias, 1999). Pour ces valeurs de T_0 l'EMP est invariable dans le vert (5 mJ/m^2) mais présente des variations considérables dans l'UV (Pour T_0=3ns EMP=41.4 mJ/m^2 et pour T_0=12ns EMP=56.8 mJ/m^2). La figure 1 représente l'énergie maximale autorisée (E) en fonction du diamètre du spot (*D*) pour le vert (EMP 5 mJ/m^2) et l'UV (dans l'UV on prend les deux cas extrêmes d'EMP 41.4 et 56.8 mJ/m^2). Pour les deux longueurs d'ondes du vert et de l'UV. L'énergie autorisée augmente proportionnellement avec le diamètre du spot. Pour l'UV on peut utiliser des niveaux d'énergie plus élevées que dans le vert. L'énergie maximale autorisée en fonction de la taille du spot pour l'UV et le vert est présentée dans le tableau 3 (entre 5 et 60 m).

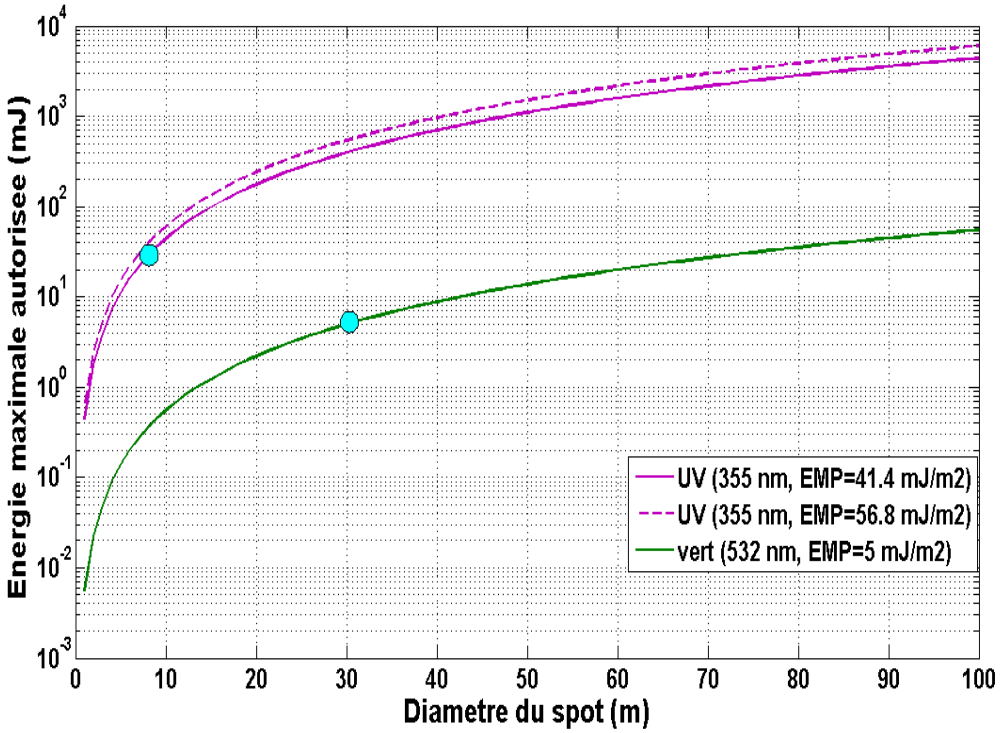

Fig.1. Énergie maximale autorisée (E) en fonction du diamètre du spot pour l'UV et le vert (échelle logarithmique). Dans le vert, EMP= 5mJ/m² et $T_{atm.}$=0.5. Dans l'UV, deux valeurs d'EMP (41.4 et 56.8mJ/m²) et $T_{atm.}$=0.34. Les points en bleu correspondent a

l'énergie maximale permise pour les spots des configurations étudiées : vert (spot de 30 m, 5 mJ), UV (spot de 8 m, 28 mJ)

Diamètre du spot (m)	**E pour le vert (EMP=5**mJ/m^2) **(mJ)**	**E pour l'UV (EMP=41.4**mJ/m^2) **(mJ)**	**E pour l'UV (EMP=56.8** mJ/m^2) **(mJ)**
5	0.13	11	15.1
8	0.50	28.1	38.5
16	1.41	112.4	154.2
20	2,20	175.6	240.9
30	5.0	395.1	542.1
40	8.78	702.4	963.7
50	13.81	1097.5	1505.8
60	19.79	1580.4	2168.3

Table 3: Énergie maximale autorisée (E) en fonction du diamètre du spot (empreinte) pour le vert et l'UV.

Si on considère nos deux configurations capteur à 500 km d'altitude dans l'UV (355nm, E_0 = 15mJ, T_0 =3 ns, $T_{atm.}$ =0,34 et γ=16 µrad et D=8m) et dans le vert (532nm, E_0= 5mJ T_0 =3.5 ns, $T_{atm.}$ =0.5, γ =60 µrad et D= 30m), l'énergie émise E_0 est bien inferieure ou égale l'énergie maximale autorisée (E) : l'énergie maximale autorisée (E) dans le vert pour un spot de 30m est de 5 mJ tandis que pour un spot de 8 m dans l'UV l'énergie autorisée est de 28 mJ. Ainsi, pour notre configuration LiDAR vert testée, il n'est pas possible de dépasser l'énergie testé sauf pour des tailles de spots supérieures à 30 m (Table 3). En revanche, pour la configuration dans l'UV, l'énergie émise testée est de l'ordre de 15 mJ (taille de spot=8m) tandis que l'énergie optimale autorisée pour un spot de 8 m tout en respectant la sécurité oculaire est de l'ordre de 28 mJ. Ainsi, pour notre configuration dans l'UV nous pourrions tester une énergie plus élevée, ce qui permettrait a priori d'accroitre les performances bathymétriques.

1.1. Potential of space-borne LiDAR sensors for global bathymetry in coastal and inland waters.

Abdallah H., Bailly J.S., Baghdadi N., Saint Geours N. and Fabre F., 2012. Potential of space-borne LiDAR sensors for global bathymetry in coastal and inland waters. IEEE JSTARS (Journal of Selected Topics in Applied Earth Observation and Remote Sensing) (in press).

Potential of space-borne LiDAR sensors for global bathymetry in coastal and inland waters

H. Abdallah, J.-S. Bailly, N. Baghdadi, N. Saint-Geours, F. Fabre

Abstract— This work aimed to prospect future space-borne LiDAR sensor capacities for global bathymetry over inland and coastal waters. The sensor performances were assessed using a methodology based on waveform simulation. A global representative simulated waveform database is first built from the Wa-LiD (Water LiDAR) waveform simulator and from distributions of water parameters assumed to be representative at the global scale. A bathymetry detection and estimation process is thus applied to each waveform to determine the bathymetric measurement probabilities in coastal waters, shallow lakes, deep lakes and rivers for a range of water depths. Finally, with a sensitivity analysis of waveforms, the accuracy and some limiting factors of the bathymetry are identified for the dominant water parameters.

Two future space-borne LiDAR sensors were explored: an ultraviolet (UV) LiDAR and a green LiDAR. The results show that the bathymetric measurement probabilities at a 1 m depth is 63%, 54%, 24% and 19% with the green LiDAR for deep lakes, coastal waters, rivers and shallow lakes, respectively, and 10%, 22%, 1% and 0% with the UV LiDAR, respectively.

The threshold values of dominant water parameters (sediment, yellow substance and phytoplankton concentrations) above which bathymetry detection fails were identified and mapped. The accuracy on the bathymetry estimates for both LiDAR sensors is 2.8 cm for one standard deviation with negligible bias (approximately -0.5 cm). However, these accuracy statistics only include the errors coming from the digitizing resolution and the inversion algorithm.

Index Terms— Satellite, LiDAR, Waveform model, Bathymetry, Accuracy

I. Introduction

Bathymetry is the measurement of underwater depth. Bathymetry on coastal and inland waters is important for a wide range of research topics and for a variety of societal needs. In coastal waters, these needs correspond to maritime navigation, ocean circulation modelling [1], ecosystem monitoring [2], tsunami or hurricane risk prevention [3], and marine archaeology [4]. In inland waters, bathymetry mapping is important for navigation and can help efforts to manage and sustain natural resources financially and ecologically [5], [6]. Moreover, monitoring the changes in bathymetry in time can be used to identify patterns of fluvial or coastal erosion or deposition to support a process of sustainable management [7], [8].

Water depth can be measured directly with conventional methods by dropping a weighted line into the water, or either indirectly with remote sensing methods [9]. Bathymetric remote sensors mainly include single-beam and Doppler echo sounders [10], [11] or multi-beam SONAR (Sound Navigation And Ranging) (e.g., [12], [13]). Because echo sounder systems are not capable of measuring depth in very shallow water, bathymetry coverage is usually incomplete in coastal and inland waters [14]. As an alternative, optical imagery has been used to estimate water depth, but only in clear water conditions [9], [15], [16].

Despite the use of optical signals, Airborne LiDAR Bathymetry (ALB) systems have proved to be suitable for mapping bathymetry because of their accuracy and high spatial density features [17]-[19], and they can penetrate waters up to three times deeper than can passive systems [20]. Currently, the operational ALB systems are (i) the Scanning Hydrographic Operational Airborne LiDAR Survey system (SHOALS) manufactured by Optech Inc. and under contract to the U.S. Army Corps of Engineers [21], (ii) the HawkEye system from the Swedish Navy and Hydrographic Department [18], (iii) the Australian Laser Airborne Depth Sounder (LADS) [22], and (iv) the Experimental Advanced Airborne Research LiDAR (EAARL) [8]. Most of these ALB detectors use a green laser pulse in their emissions (532 nm) and can register returned waveforms with contributions from the water surface, column and bottom [23]-[25]. A way to estimate water depth from LiDAR waveforms is thus to multiply the half time difference between the water surface and the bottom peaks by the speed of light in the inherent water column [26], [27].

Many studies aimed to quantify bathymetry accuracies from airborne bathymetric LiDAR systems in coastal waters, lakes or rivers. The computed accuracy on the bathymetry estimates ranged between 7 cm and 32 cm for one standard deviation [8], [17], [19], [28], [29], with a maximal depth penetration ranging from 15 to 50 m [19], [29], [30].

However, compared to other remote sensing bathymetric techniques, LiDAR systems have some disadvantages. First,

Manuscript received March x, 2012. This work was supported in part by the CNES (French Space Agency) and EADS (European Aeronautic Defense and Space Company).

H. Abdallah is with the IRSTEA, UMR TETIS, BP 5095, Montpellier, France (+33-467-548-719; fax: +33-467-548-700; e-mail: hani.abdallah@teledetection.fr)

J.-S. Bailly is with AgroParisTech, UMR LISAH, F-34060, Montpellier , France (e-mail: jean-stephane.bailly@teledetection.fr)

N. Baghdadi is with the IRSTEA, UMR TETIS, BP 5095, Montpellier, France (e-mail: nicolas.baghdadi@teledetection.fr)

N. Saint-Geours is with AgroParisTech, UMR TETIS, BP 5095, Montpellier, France (e-mail: nathalie.saint-geours@teledetection.fr)

F. Fabre is with EADS – Astrium, F-31402 Toulouse , France (e-mail: frederic.fabre@astrium.eads.net)

the feasibility of measurements is dependent on water clarity. Some surveys may need to be repeated if water clarity is too low. Secondly, surface waves can generate surface foams which can make bathymetry more difficult. Conversely, specular reflexion of laser beams in the case of flat water surfaces can cause distortion or saturation events and can overload the detector [31]. Consequently, most of ALB sensors use a constant off nadir scan angle that also makes the refraction corrections constant. Finally, ALB techniques have limitations to map global near shore bathymetry with regard to reduced spatial coverage and costs. This latter disadvantage leads to the consideration of space-borne bathymetric LiDAR systems.

To date, one space-borne LiDAR sensor has been launched: the Geoscience Laser Altimeter System (GLAS) from ICESat (Ice Cloud and Elevation Satellite). The first objective of this system was to determine the mass balance of the polar ice sheets and their contributions to global sea level change. The second objective was to measure the cloud heights and aerosols in the atmosphere and to map the topography of land surfaces. The second generation of the ICESat orbiting laser altimeter is scheduled for launch in late 2015. The European Space Agency (ESA) plans to launch the Atmospheric Dynamics Mission Aeolus (ADM-Aeolus), based on a Doppler Ultraviolet Lidar system, in 2013 to perform global wind-component-profile observations [32]. These space-borne LiDAR missions are not dedicated to bathymetric uses.

Consequently, future bathymetric satellite LiDAR mission configurations need to be explored to answer the following questions: What percentage of shallow immersed Earth surfaces can be viewed by a bathymetric satellite LiDAR and at what accuracy? How much does it depend on LiDAR parameters?

One way to investigate these questions is to analyse the performance of satellite LiDAR configurations for bathymetric applications from a database of LiDAR waveforms representative of the physical conditions of the water encountered all over the Earth. However, to produce a database that is representative of all possible physical conditions of the water using different LiDAR configurations would require a huge investment in time, manpower, and money. For these reasons, the use of simulated waveforms provided from LiDAR signal models is an interesting alternative.

Recently, a Water LiDAR simulator (Wa-LiD) was developed to generate LiDAR waveforms for any wavelength in the optical spectrum domain between 300 and 1500 nm [33]. This simulator is based on equations from previous hydrographic LiDAR models [23]-[25], [34] but it integrates radiative transfer laws governed by the physical properties of water for any wavelength. In addition, this simulation model uses a geometrical representation of the water surface with the geometric model of Cook and Torrance [35], and it takes into account both the characteristics of detection noise and the signal level due to solar radiation.

The main objective of this study is to propose a framework that permits estimation of the overall bathymetric performance of satellite LiDAR sensors. Within the proposed framework, the performances of sensors on inland and coastal water types (coastal, river, shallow lake and deep lake waters) are also analysed separately. This framework mainly relies on the exploitation of a representative database of water parameters that is used to simulate LiDAR waveforms according to the distributions of water parameter values that are most encountered at the global scale and for each water type.

In this study, two bathymetric LiDAR sensor configurations were investigated. The first emits laser beams in the usual green wavelength (532 nm) and the second uses the UV wavelength (355 nm). From the usual Nd-YAG lasers (Neodymium-doped Yttrium Aluminium Garnet), the green wavelength is known to offer the highest penetration performance and is therefore the most often used wavelength in airborne LiDAR bathymetry [17], [36]. The UV wavelength can also penetrate clear water despite being more absorbed than the green wavelength [37]. UV has been used to measure ozone and aerosols in the atmosphere, such as the Differential Absorption LiDAR (DIAL) of NASA [38], [39], and forest canopy geometry [40]. An other example of UV LiDAR sensor is the ATLID sensor (ESA's Satellite-borne Atmospheric LiDAR sensor), designed to provide satellite measurements of cloud-top height both at day and night times [41].

The overall proposed framework is divided into four steps corresponding to the main parts of this paper.

First, the input parameters of the Wa-LiD model are selected and used to generate a simulated LiDAR waveforms database. These parameters are (i) system parameters depending on the two system configurations (e.g., emitted power, pulse width, receiver area, field of view) and (ii) water parameters (e.g., surface and bottom slope, surface rugosity, sediment concentration).

Second, due to the large number of water parameters used in the Wa-LiD model and because of a recently proposed methodology [42], a Global Sensitivity Analysis (GSA) of the Wa-LiD waveforms to water parameters is performed to identify the dominant water parameters that highly influence backscattered waveforms for each type of water.

Third, the waveforms that permit detection of the water bottom are identified through a peak detection method. Therefore, the detection probabilities of the water bottom are computed for the two LiDAR configurations, all water types, and different water depths.

Finally, after using adapted mathematical functions to fit the different contributions of the LiDAR signal (surface, column and bottom), the accuracy of the bathymetry estimates for waveforms with a detectable water bottom is estimated. The signal to noise ratio (SNR) and the threshold values of dominant water parameters for bathymetry are also identified.

II. Materials and Methods

A. Waveform simulation

The simulated waveforms used in this study were generated by the Wa-LiD model [33]. The Wa-LiD model integrates both noise due to solar radiation and detector noise, making

this model especially suitable for satellite LiDAR mission exploratory studies.

In the Wa-LiD model, the outputs are simulated waveforms received by the LiDAR sensor corresponding to photonic power as a function of time *t*. These waveforms are assumed to be the sum of the echo waveforms backscattered from the successive media encountered by the laser beam [24]:

$$P_T(t) = P_s(t) + P_c(t) + P_b(t) + P_{bg}(t) + P_N(t) \quad (1)$$

where $P_T(t)$ denotes the waveform recorded by the detector, $P_s(t)$ denotes the water surface contribution waveform, $P_c(t)$ denotes the water column contribution waveform, and $P_b(t)$ denotes the bottom contribution waveform. The noise was divided into two sources:

(i) the shot noise contribution $P_{bg}(t)$ coming from solar radiations is defined as a Gaussian white noise with parameters depending on the solar irradiance and the Field Of View (FOV) [34], [43]. The solar irradiance was fixed to 0.025 W/m²sr (value for daytime operation [25], [34]).

(ii) the detector noise contribution $P_N(t)$ which is co-linear to all other waveform contributions [33].

However, Wa-LiD does not take into account the atmospheric noise which depends on the attenuation and volume scattering by particles and molecules constituting the atmosphere such as aerosols, water vapor, etc [44], [45].

The equations and parameters interacting in these different power components can be found in detail in Abdallah et al. [33]. The Wa-LiD model simulates each waveform contribution, such as the bottom waveform contribution which is the key information to estimate bathymetry from LiDAR waveforms [26]. Wa-LiD was validated by comparing the simulations to actual airborne or satellite data in the 532 nm and 1064 nm spectra (HawkEye and GLAS): the Wa-LiD model showed a good ability to simulate the observed waveforms by fitting unknown water parameters [33]. However, the Wa-LiD simulations depend on many sensor and water parameters.

1) Sensor parameters of the Wa-LiD model

Two bathymetric satellite LiDAR configurations were investigated in this study. The first emits laser beams in the usual 532 nm wavelength (green). The second uses the UV wavelength (355 nm).

The values of the instrumental parameters acting in the Wa-LiD equations may or may not depend on the LiDAR wavelength. The retained values of these parameters were chosen with the EADS-Astrium company (European Aeronautic Defense and Space Company) and listed in Table 1. The lowest FOV angle used in simulation reduce highly the solar radiation noise. Consequently our simulated waveforms are slightly noised compared to actual waveforms coming from sensors with higher FOV angles (Fig. 1).

2) Water parameters of the Wa-LiD model

Four types of inland and coastal waters were distinguished in this study: coastal, river, shallow lake and deep lake waters. The optical properties of water are different in shallow and deep lakes because shallow waters are richer in suspended sediments and dissolved organic matter (yellow substances) [46]. Table 2 presents the range values and distribution laws for water parameters that do not depend on water types. These parameters are connected to the water surface or bottom characteristics. Most of shallow waters in coastal areas have a small bottom slope [47], the steep slope was founded in special case of water bottom for example around the Arctic and can reach 39° [48]. Moreover, it has been shown that slope distribution in rivers usually follows an exponential decrease from upstream to downstream [49]. For these reasons, we used the log-normal distribution of S_b (Table 2) for all water types centred on a value of 3° that generates little number of high slope values.

Table 3 shows the range values and the related distribution laws for the water column parameters depending on each water type. The distribution laws and range values of yellow substances a_{y0}, phytoplankton C_{ph} and sediment S came from existing databases collected on water bodies around the world (from USGS data collected between 1977 and 1999 and from the SeaWiFS Project of NASA/GSFC (Goddard Space Flight Centre, 1997). The k_s parameter, which corresponds to the coefficient of specular light backscattered from the water surface, can theoretically vary between 0 and 1, corresponding to totally diffuse or totally specular surfaces, respectively [35]. In this study, a uniform distribution [0.6 – 0.9] of k_s was chosen arbitrarily in regard to the geometrical representation of the water surface, such as small specular facets in the Cook-Torrance model. For the r parameter, corresponding to the root mean square error of the surface facet slopes in the Cook-Torrance model, a range of 0.1-0.5 was chosen. This range was given by the unique literature of Beckman and Spizzochino [50]. The values of the R_b parameter corresponding to the bottom albedo were given by the literature for different types of bottoms: gravel, sand, limestone, periphyton, debris, cobble, algae and mud [15], [20], [51], [52].

Fig. 2 shows the collected distributions for all Wa-LiD water parameters and for the four types of waters. The sediment concentration varies from 0 to 250 mg/l in the river waters, but only from 0 to 15 mg/l in the deep lake water. Similarly, the a_{y0} histograms come from data collected worldwide [53]. The empirical histograms of S and a_{y0} were thus fitted with log-normal density functions (Fig. 2). The fitting process gives the μ and σ log-normal law parameter estimates. The phytoplankton concentrations C_{ph} and log-normal distribution parameters (μ and σ) were more directly given by [61], [62].

The water parameters including all the scene parameters are assumed to be homogeneous within the footprint or FOV area.

3) Wa-LiD simulation examples

Fig. 3 shows examples of simulated waveforms for the two studied satellite LiDAR sensors with the sensor parameter values given in Table 1. We used in our simulations a simplified theoretical case: the temporal origin of our waveforms was fixed arbitrary. It does not simulate the sensor

orbit. Here, the water surface was considered smooth (k_s = 0.9, r=0.1) and the water bottom was sandy (R_b=0.12). The water column parameters used in these simulations correspond to the mean coastal water conditions: i) a yellow substances concentration a_{y0} equal to 0.1 m^{-1}, ii) a phytoplankton concentration C_{ph} equal to 8 mg/m^3 and iii) a sediment concentration S equal to 9 mg/l. Waveforms were generated for water depths equal to 1, 2, 3 and 5 m. As shown in Fig. 3, the bottom peak magnitude in the received waveforms decreases with water depth due to laser beam attenuation along the water column. The green signal penetrates deeper into the water column depending on the water properties and is reflected from the bottom, showing a significant bottom waveform contribution. The UV signal is attenuated in the water column, and the bottom waveform contribution is low for shallow water and disappears for deep water.

Fig. 4 shows the effects of the bottom slope on waveforms. For highest slopes, the bottom echo is highly stretched and its width becomes larger than the width of other echoes (approximately 70 ns for a slope of 35°).

B. Sensitivity analysis of LiDAR bottom contribution waveforms

A sensitivity analysis will be performed to determine the dominant water parameters on the bottom contribution waveforms that result from the interaction between the laser beam passing through the water surface, the water column and the water bottom. Because an analytical analysis of the Wa-LiD model sensitivity would be difficult, we preferred to use a variance-based method using a quasi Monte-Carlo experimental design of model parameters and producing synthetic and easily interpretable sensitivity indices: the Sobol sensitivity indices [63].

1) Experimental design

To perform a Sobol sensitivity analysis of all water parameters on the bottom contribution waveform (except water depth), we used the quasi-random Sobol sampling in the water parameter distributions (Tables 2 and 3), and known to be one of the best random sampling designs for the Sobol sensitivity analysis framework [64], [65]. The design was also stratified among the two sensor configurations (532 and 355 nm) and the four water types (coastal, river, shallow lake and deep lake) for six different depths (1, 2, 3, 5, 10 and 15 m). Forty-eight strata were thus obtained having a set of 10 000 simulated waveforms for each. We thus produced a database of 480 000 Wa-LiD simulated waveforms.

2) Sensitivity indices: Sobol indices

To determine the dominant water parameters, two Sobol sensitivity indices were calculated: the first-order sensitivity index (*SI*) and the total sensitivity index (*TS*). We retained *TS* as a unique sensitivity indicator because it integrates interactions of parameters in the Wa-LiD model. For given water parameter X_i and a scalar model output Y, the generic formulation of *TS* is:

$$TSi = \frac{1 - V(E(Y \mid X_{-i}))}{V(Y)} \quad (2)$$

where $V(Y)$ is the variance of Y and $E(Y)$ is its expectation. X_{-i} denotes all other parameters but X_i. $V(E(Y|X_{-i}))$ is the variance of the conditional expectation of Y, having frozen all sources of variation but X_i. Consequently, TS_i usually ranges from 0 to 1, and the higher the TS_i, the more sensitive the model to X_i.

Here, the Y model output is $P_b(t)$, which is multidimensional. Therefore, a multivariate global sensitivity analysis method [42] proposed initially by Campbell et al. [66] is used. The principle of this multidimensional Sobol method is i) to decompose the model outputs (waveforms) upon a complete orthogonal basis computed by Principal Component Analysis (PCA) and ii) to compute Sobol indices on each component of the decomposition. Then, a unique Sobol index attached to a water parameter result from the scalar product between the first-order Sobol indices and related eigenvalues from PCA [42].

C. Water bottom echo detection from Wa-LiD waveforms

The registered LiDAR waveforms $P(t)$ allowing bathymetry are usually composed of two main peaks representing the surface and the bottom echoes [17]. To detect the water bottom echo, i.e., the peak from Wa-LiD waveforms, a Wiener filtering was used in a denoising step [67] to smooth the waveform and to facilitate a search of the two peaks (Fig. 5). Second, a peak detection method is applied on the smoothed waveform $\tilde{P}(t)$, and it searches the amplitude and the time position of the first maximum (the instant where $\tilde{P}(t_i) > \tilde{P}(t_{i+1})$). This maximum should be greater than the maximum of $\tilde{P}(t_i)$ between t_1 and t_{begin} (Fig. 5), where t_{begin} is fixed according to a constant distance between the sensor and the water surface. The search for the first maximum proceeds in two ways:

- Forward, from the beginning of the time series (t_{begin}) to the end of the time series (t_n). The peak found is thus considered to be the surface peak, with amplitude A_s and a time position t_s.
- Backward, from t_n to t_{begin} to find the bottom peak, giving the bottom amplitude A_b and the time position t_b.

When the two peaks are found, the waveform is declared to have a detectable bottom. This process permits the identification of waveforms with a detectable water bottom from the simulated waveform database.

To analyse the bathymetric performances of each of the studied sensors, the percentage of waveforms with a detectable bottom were calculated for each water type and for different water depths (1, 2, 3, 5, 10 and 15 m).

D. Bathymetry estimation from Wa-LiD waveforms

Waveforms presenting a detectable bottom are fitted by mathematical functions. Several functions have been

performed in the literature to fit the waveform components, such as two Gaussian curves to approximate both the surface and the bottom returns [26] or three Gaussian curves used [68] to fit the water surface, the water column and the bottom return. Other functions are also used, such as the Weibull distribution and the Burr function, to approximate asymmetric waveforms [69]. Moreover, several combinations of functions were tested by the work of Ceccaldi (Master thesis, 2011) to fit the waveform contributions, but the combination of a Gaussian function, a triangle function and a Weibull function to fit the surface, the column and the bottom echoes, respectively, showed the best fit.

Our algorithm uses the same mixture of functions as follows:

$$\hat{P}(t) = G(t; A_s, \mu_s, \sigma_s) + T(t; A_c, a, b, c) + W(t; A_b, k_b, \lambda_b) \quad (3)$$

where $G(t; A_s, \mu_s, \sigma_s)$ is the Gaussian function defined as:

$$G(t; A_s, \mu_s, \sigma_s) = A_s \exp\left(\frac{-(t-\mu_s)^2}{2\sigma_s^2}\right) \quad (4)$$

where A_s is the scale factor (amplitude) of the Gaussian, μ_s is the time position of the surface (ns), and σ_s is the standard deviation.

$T(t; A_c, a, b, c)$ is the triangle function [70] multiplied by an amplitude A_c and defined as:

$$T(t; A_c, a, b, c) = A_c \times \begin{cases} 0 & when\ t \le a \\ \frac{t-a}{b-a} & when\ a \le t \le b \\ \frac{c-t}{c-b} & when\ b \le t \le c \\ 0 & when\ c \le t \end{cases} \quad (5)$$

(a, b, c) denote the time positions of triangle vertices.

$W(t; A_b, k_b, \lambda_b)$ is the Weibull function multiplied by an amplitude A_b [71]:

$$W(t; A_b, k_b, \lambda_b) = A_b.(k_b / \lambda_b)(t/\lambda_b)^{(k_b-1)} \exp(-t/\lambda_b)^{k_b} \quad (6)$$

λ_b is the scale parameter (time position of the bottom in ns) and k_b is the shape parameter.

A nonlinear least-squares (NLS) approach using the Levenberg-Marquardt optimisation algorithm [72], [73] was performed to fit the sum of three functions $\hat{P}(t)$ (Fig. 6). The NLS fitting was initialised with values provided by the peak detection method for the amplitudes and time positions (i) of the Gaussian function (A_s, μ_s) and (ii) of the Weibull function (A_b, λ_b). The shapes of the Gaussian (σ_s) and Weibull functions (k_b) are initialised as $\sigma_s = k_b = T_0/2$, where T_0 is the emitted pulse width at half maximum. The triangle function amplitude is initialised by $A_c = A_s/2$. The triangle vertices a, b and c are initialised with μ_s, $\mu_s + 3\sigma_s$, λ_b, respectively.

The NLS fitting provides fitted parameter values. The bathymetry estimate D_e could be calculated as follows:

$$D_e = c_w \frac{(\lambda_b - \mu_s)}{2} \cos(\theta_L) \quad (7)$$

where c_w is the celerity of light in water (m/s) and θ_L is the local incidence angle. θ_L depend on the incidence angle of the sensor, the water refractive index and the water surface and bottom slope.

Next, the bias $\bar{\varepsilon}$, i.e., mean of errors $\varepsilon = D_e - D_a$ and the standard deviation (*SD*) between the estimated depth retrieved from waveforms (D_e) and the actual depth, denoted as D_a, was calculated for each type of water using the usual accuracy statistics:

$\bar{\varepsilon} = \frac{1}{N}\sum_{i=1}^{N} \varepsilon_i$ with N equal to the number of waveforms.

$$SD = \sqrt{\frac{1}{N-1}\sum_{i=1}^{N} (\varepsilon_i - \bar{\varepsilon})^2}$$

1) Water parameter values limiting bathymetry detection

The range values of the dominant water parameters were divided into regular intervals (logarithmic scale), and the detection probability was mapped for each dominant water parameter pair. For each interval pair, the detection probability was defined as the ratio between the number of detectable waveforms and the total number of waveforms belonging to these intervals. From these maps, the threshold values of dominant water parameters are identified to delineate detection areas, i.e., areas where the detection probability is greater than zero.

2) Signal to Noise Ratio (SNR)

The noise in waveforms is a limiting factor in detecting bottom echoes and estimating bathymetry. Thus, the ratio between the bottom peak amplitude and the standard deviation σ of the noise (sum of two noise contributions: $P_{bg}(t) + P_N(t)$), i.e., the signal to noise ratio, was calculated for each Wa-LiD waveform as:

$$SNR = \frac{max(P_b(t))}{\sigma} \quad (8)$$

The *SNR* distribution of detectable waveforms was calculated for each water type and different water depths. The lowest *SNR* values that permit the bathymetry to be detected were also identified.

III. Results

A. Global bathymetry probability in coastal and inland waters

Using the peak detection method described in method section 2.3, Fig. 7 presents the bathymetric probabilities, i.e., the percentage of waveforms with a detectable water bottom, we can expect from the two studied sensors for all coastal or inland water types. Obviously, the bathymetry probability decreases with water depth whatever the water type. With the

green sensor, the bathymetry probability becomes lower than 20% for water depths greater than 5 m in coastal waters and deep lakes (Fig. 7a). For rivers and shallow lake waters, the bathymetry probability is lower than 10% for depths higher than 2 m. The results obtained also show that for all water types, the bathymetry probability in the green sensor is more important than that in the UV. For example, the bathymetry probability is 53.5% in the coastal water compared with 22% in the UV (Fig. 7b).

With the UV sensor, the bathymetry probability is low for all water types and becomes lower than 10% for water depths greater than 3 m. Moreover, the highest probabilities are obtained for coastal waters, decreasing from 22% at a 1 m water depth down to 3% at 5 m. For river waters and shallow lakes, the bathymetry probability is close to 0 for any water depth (Fig. 7b). In deep lakes, the bathymetry probability varies from 10% at 1 m to 1.4% at 3 m.

B. Sensitivity analysis of simulated bottom echoes

Figs. 8 and 9 present the total sensitivity (TS) indices of the water parameters for the green and UV sensors. The TSs for each of the two system configurations were assessed for the four water types and for six different depths (1, 2, 3, 5, 10 and 15 m). For all water types and for the two system configurations, three water parameters have a negligible impact on the bottom waveforms with TS indices close to 0: the surface slope S_S, the bottom slope S_b and the specular bidirectional reflectance k_s. The results can be summarised as follows (Figs. 8 and 9):

- for coastal waters and with the green LiDAR sensor (Fig. 8a), the sediment concentration S is the dominant (the most impacting) parameter for all water depths. However, the TS index of the phytoplankton concentration (C_{ph}) increases with water depth and shows a higher impact from a 10 to 15 m depth. With the UV LiDAR sensor (Fig. 9a), the TS indices of S are the highest for all water depths (greater than 0.8 in Fig. 8a). For C_{ph}, the TS index increases strongly with the water depth and reaches high values for depths greater than 10 m. For the yellow substances concentration (a_{y0}), the TS index decreases with water depth from 0.5 at a 1 m depth to 0 for water depths greater than 5 m. The other water parameters (roughness r, bottom reflectance R_b) show negligible impacts in the UV and green configurations.
- in rivers, a_{y0} and S have the highest TS indices for all depths with both UV and green sensor configurations. The TS index of C_{ph} increases with water depth and reaches the highest values for depths greater than 5 m with the green sensor (Fig. 8b) and greater than 2 m with the UV sensor (Fig. 9b). The bottom reflectance R_b shows moderate TS indices (between 0.1 and 0.4 for the green and approximately 0.4 for the UV). The sensitivity of other parameters is very low.
- in deep lakes and for the green configuration (Fig. 8c), C_{ph} and a_{y0} show a higher impact on the bottom waveforms for all depths. Moreover, S and r show high sensitivity indices only for high water depths (>10 m). For the UV sensor configuration (Fig. 9c), a_{y0} shows the most important TS for any depth. For depths greater than 2 m, C_{ph} and S show higher values of TS. The parameter r shows remarkable values of TS for depths greater than 3 m. The bottom reflectance R_b shows a negligible impact in the two configurations and for all depths.
- in shallow lakes and for both green and UV LiDAR configurations, the TS indices of C_{ph}, a_{y0} and S are the highest for all depths and they increase with water depth. In the UV configuration, the TS values of these three parameters are more important than the *TS* values in the green configuration. The roughness r and the bottom reflectance R_b show negligible impacts.

C. Water parameters limiting bathymetry

The sensitivity analysis showed that three of the eight water parameters (S, a_{y0}, C_{ph}) have the highest impact on the bottom waveforms. We therefore hypothesised that these three dominant parameters are the most limiting to bathymetry. Maps of the bathymetry detection were thus produced for dominant parameter pairs for each water type, for each depth and for both sensors using the same simulated waveform database as previously. In the proposed sensitivity analysis study, the bottom slope S_b did not appear as an impacting parameter although it is known that the bottom slope influences strongly the bottom echoes (Fig. 4). Indeed, this is due to the log-normal distribution of S_b used for the waveforms simulations that limit effects of high slopes (> 10°) being lowly probable. Moreover, *SA* was performed for a fixed and limited range time in the waveform scale that did not permit to completely take into account the stretching effect of slopes on the bottom echo. For this reason we chose here to also consider bottom slope as a dominant factor.

Figs. 10, 11 and 12 present the results of bathymetry probability in function of (a_{y0},S) parameters, (C_{ph},S) parameters and in function of (S_b,S) parameters in coastal waters. The sub-figures present separate results for the green and UV sensors and for 1, 5 and 10 m water depths. For some intervals of water parameters corresponding to low values, the lowest probabilities (<0.1) are observed. These values are not significant because they correspond to a low number of simulated waveforms in these intervals of water parameters.

The shapes of the probability features on these maps in logarithmic scales are identical (circular and concentric shapes), and they show the interaction of parameter pairs in bathymetry probabilities. The interest of such maps is to identify the parameter threshold that delineates the areas where bathymetry is possible (probability greater than 0) and those where it is not. These maps may be seen as guidelines or abaci that permit the estimation of bathymetry probability from a space-borne LiDAR sensor on a particular river, lake or littoral environment. These thresholds of dominant water parameter values (sediment, yellow substance and phytoplankton concentrations), above which bathymetry detection fails, are resumed in Table 4.

For instance, at a 1 m coastal water depth and with green LiDAR, bathymetry cannot be performed when the sediment concentration S is higher than 76 mg/l or when the yellow substance concentration a_{y0} is higher than 4.5 mg/l or when the bottom slope S_b is higher than 10°. As a comparison, in 1m depth coastal water and with UV LiDAR, bathymetry cannot be performed when the sediment concentration S is higher than 30 mg/l or when the yellow substance concentration a_{y0} is higher than 0.4 mg/l or when the bottom slope S_b is higher than 8°.

D. Bathymetry accuracy

The waveforms with a detectable bottom were used to determine the water depth using the process detailed in the method section. The errors, i.e., the differences between the water depths retrieved from the fitted waveforms and the actual depths used for simulation, were calculated. Therefore, the usual error statistics, that is, the mean of errors (bias) and the standard deviation of errors (SD) were also computed. These statistics can be summarised as follows (Fig. 13).

For the green configuration, the bias ranges from -0.1 to -1.2 cm (Fig. 13a), with an SD between 1.7 and 5.0 cm (Fig. 13b). The over-estimations of the bathymetry observed in the river water at a 10 m depth and in the shallow lake water at a 5 m depth correspond to two cases where the percentage of detectable waveforms is very low (0.30 % and 0.33 %, respectively). Therefore, this overestimation related to low number of data is not significant.

For the UV sensor, the bias ranges from -0.4 to -2.0 cm (Fig. 13c), with SD values between 1.0 and 4.7 cm (Fig. 13d). An underestimation of the water depth was also observed for all water types and at all depths except in coastal water at a 10 m depth. The overestimation of the bathymetry observed for coastal water at a 10 m depth due to the lowest percentage (0.9%) of detectable waveforms is also considered non-significant.

E. Signal to noise ratio (SNR) of bottom echoes in waveforms with a detectable bottom

The signal to noise ratio (SNR) for bathymetry is defined here by the ratio of the bottom peak amplitude in the waveforms to the noise amplitude. To determine the distribution of SNRs for each water type and water depth, it was calculated for each simulated waveform with a detectable bottom. The minimum and maximum SNRs were calculated for each case in using the two studied LiDAR sensors (Table 5).

The SNR values obviously decrease with water depth in the green and the UV configurations for all water types.

Fig. 14 shows a sample of SNR boxplots in coastal water. For the green waveforms, the median of the SNR decreases with water depth from 358 at a 1 m water depth up to 21 at a 15 m water depth (Fig. 14a). For the UV waveforms, the median SNR decreases from 155 at a 1 m water depth up to 0 at a 15 m water depth (Fig. 14b). However, the most important task from the SNR calculation is to identify the lowest SNR values allowing bathymetry.

IV. Discussions

A. Green or UV space-borne LiDAR mission

The two sensor configurations used in this study are approachable with advanced technologies in the next few years (personal communication from the Astrium-EADS company, a European company in space transportation, satellite systems and services). All ALB systems use the 532 nm wavelength because it is the Nd-YAG derivative wavelength that most deeply penetrates turbid waters. Obviously, this is the space-borne sensor that gave the best overall performance. In comparison, to date the UV was not used for bathymetry in coastal and inland waters. However, with the used configuration in this study, the results show the interest of the UV configuration in clear coastal waters and deep lakes and for very shallow water depths. Moreover, these results on the UV sensor capacities could be improved by using higher laser emitted power since there is still room to increase this emitted power according to eye safety regulation.

Regarding the SNR values, the bottom peak amplitude without noise in the UV is lower than that in the green (approximately 40 times at a 1 m water depth). At the opposite, the noise power defined as the sum of the solar radiation noise and the detector noise is five times greater in the green than in the UV configuration. Consequently, the SNR values corresponding to LiDAR green waveforms are also obviously higher than those for the UV.

The main advantage of the UV sensor is its ability to be used for multiple applications, including bathymetry, forestry [40] and atmospheric sciences [74]. However, if future technologies with other high frequency pumped laser emerges, blue wavelength LiDAR (450 nm) should also be an interesting alternative for bathymetry [75].

B. Other factors affecting space-borne bathymetry

First, the bed morphology of all water types used in simulations is considered as a sloped plane with various slope values. Indeed, more complex morphologies of the bed (micro-geometry, algae presence, etc) within laser footprints may occur which provide additional uncertainty in bathymetry estimation and decrease the overall bathymetry probability results.

In addition, we assumed that the distributions of water parameters were consistent across the depth of water (one layer) and independent of each other.

Second, future works should include the atmospheric effects in the LiDAR signal simulations.

Third, the main limitation of spaceborne LiDARs is the mission's lifetime related to the laser shot number emitted in the operational period of LiDAR. Therefore, it will be difficult to obtain data with a high spatial density and a high revisit time from spaceborne LiDAR. In coastal waters, where the bathymetry varies very strongly with distance from the coast, a low spacing between successive footprints is necessary for correctly mapping the bathymetry. However, these other

aspects of the LiDAR mission configuration should also be explored in future works.

C. Bathymetry accuracy from space-borne LiDARs

Firstly, the used digitizing frequency is of 1 GHz which corresponds to a depth resolution of about 11.4 cm. This is the usual digitizing frequency of airborne sensors and GLAS sensors. The magnitude of errors due to this digitizing resolution for the explored depths (1m, 2m, 3m, 5m, 10m, 15 m) is of the same order that the computed accuracy. Consequently, the obtained accuracy statistics on the bathymetry estimations (standard deviation of random error and bias) mainly corresponds to the errors due to digitizing resolution and fitting method errors (inversion). These accuracy statistics are also depending on the distribution of explored depths.

Moreover, in actual data, there are other error budget items to consider which are neglected here. These additional errors come from GPS positioning of the satellite, the geometry of the laser beam, atmospheric conditions, scene complexity (presence of vegetation), etc [76], [77]. Indeed, the overall accuracy (here standard deviation of the random error) of the bathymetry results on the addition of variances of these different error items. For instance, these error items are:

- Errors of about 5 cm due to GPS positioning of the sensor [78].
- Errors of about 2 cm due to pointing error of the laser beam which are for satellite at 600 km height and a near nadir laser beam [79].
- Errors of about 4 cm due to atmosphere which acts to distort the path of the laser pulse as it travels to the target and back again and produce timing errors [78], [80].

The sum of these some error budget items is coherent with accuracy studies on ICESat errors founded in literature on flat and non-complex surfaces [81], [82].

For ALB, larger errors may come from higher pointing errors due to higher incidence angles, and higher platform positioning errors. Accuracy from for ALB manufacturers is about 25 cm [18]. However, the lower noise in the waveforms due to space detector technology allows to expect more accurate statistics than the one observed in experiments from ALB sensors [8], [19], [26].

Another limitation in this study comes from the peak detection method, which is not suitable for very shallow waters (<1 m) or more noisy waveforms whatever the depth is. For very shallow waters or other sensor configurations (higher FOV angles for example), other waveform processing methods should be developed.

The proposed algorithm is not generic and would surely fail to estimate bathymetry from more noisy waveforms. But, the lowest SNR values allowing bathymetry is approximately 1.1, which corresponds to theory [44] and proves that the proposed the algorithm is efficient for slightly noised LiDAR waveforms.

Moreover, the slight underestimation of the bathymetry observed for both the green and the UV may be also due to the triangle mathematical function used to fit the water column that slightly translates the positioning of the Gaussian function used to fit the bottom echo. Finally, the highest *SD* observed in coastal water at a depth greater than 2 m should be related to the low number of data.

V. Conclusions and perspectives

This work aimed to prospect future space-borne LiDAR sensors capacities for global bathymetry over inland and coastal waters. Two future space-borne LiDAR sensors were explored: an ultraviolet (UV) LiDAR and a green LiDAR emitting at 355 and 532 nm, respectively. The sensor performances were assessed from a methodology based only on waveform simulation. A wide waveform database was first built from the existing Wa-LID waveform simulator and from an experimental design representing observed distributions of water parameters from the literature assumed to be representative at the global scale. A bathymetry detection and estimation process based on Wiener filter and mathematical function fitting were applied to each waveform to determine i) the bathymetry detection rate (bathymetry probability) in coastal waters, shallow lakes, deep lakes and rivers for a range of water depths and ii) the expected bathymetry accuracies. Finally, by using a sensitivity analysis of waveforms, some limiting factors in bathymetry were identified and mapped for the most dominant water parameters.

The results show that the bathymetry probabilities (i.e., bathymetry detection rates) at a 1 m depth are 63%, 54%, 24% and 19% with the green LiDAR for deep lakes, coastal waters, rivers and shallow lakes, respectively, and 10%, 22%, 1% and 0%, respectively, with the UV LiDAR. Obviously, the detection rates for UV LiDAR are always lower than for green LiDAR, and the rates decrease when the water depth increases. At a 10 m depth, the bathymetry probability becomes 5%, 8%, 0% and 0% with the green LiDAR for deep lakes, coastal waters, rivers and shallow lakes, respectively. When the bathymetry is detectable, its accuracy for both sensors is approximately 2.8 cm for one standard deviation with a small underestimation (approximately -0.5 cm). These accuracy statistics only include the errors coming from the digitizing resolution and the inversion algorithm.

The sensitivity analysis results indicate three dominant water parameters, which are all related to water column properties: sediment, yellow substances and phytoplankton concentrations. Maps of bathymetry probability were made for each dominant water parameter pair, each water type, and each water depth. These maps allow us to identify the thresholds of dominant water parameters above which bathymetry detection fails. These maps are thus guidelines to estimating bathymetry probability from a space-borne LiDAR sensor on a particular river, lake or littoral environment.

The innovation of this paper mainly comes from the proposed global methodology chaining different compartments: signal modelling, experimental design, sensitivity analysis and signal inversion. This methodology should be considered as a starting point to explore the global

performances and limiting factors of any future space-borne LiDAR sensor totally or partially dedicated to bathymetry. Of course, it still exists many limitations in each methodological compartment but the global results permit to identify and rank these limitations which should be the points to be improved in future works. For instance, the sensor performances are strongly related to the representativeness of the waveform database at the global scale and, thus, to water parameter distributions. Here, we assumed that the distributions of the water parameters were homogeneous for any water depth. This assumption is certainly not entirely true, and it should be refined in future works. For other water parameters, such as water surface roughness or water specular coefficients, experiments and ground data acquisition are needed for a better estimation of distributions. This is true for all other parameters: there is a need to build or feed global databases on these parameters that will ensure better performance assessments. However, the proposed methodology in this paper is already capable of exploring other sensor configurations (e.g., the blue wavelength) for future bathymetric satellite LiDAR mission exploration.

ACKNOWLEDGMENTS

The authors would like to thank EADS (European Aeronautic Defence and Space Company) and CNES (French Space Agency), both of which supported this study, and especially Yves Pastol from SHOM (French Naval Hydrographic and Oceanographic Service) for his useful advice.

REFERENCES

[1] A. F. Blumberg and G. L. Mellor. "A description of a three-dimensional coastal ocean circulation model", *In: Heaps, N. (Ed.), Three-dimensional Coastal Ocean Models*, 1987, pp. 1–16.

[2] J. Ferreira, C. Vale, C. Soares, F. Salas, P. Stacey, and S. Bricker, "Monitoring of coastal and transitional waters under the E.U.", *Water Framework Directive Environ Monit Assess*, 135, 2007, pp. 195–216.

[3] N. A. Duong, F. Kimata and I. Meilano, "Assessment of Bathymetry Effects on Tsunami Propagation in Viet Nam", *Namadu Journal*, 9(6), 2008, pp.1-9.

[4] K. Westley, R. Quinn, W. Forsythe, R. Plets, T. Bell, S. Benetti, F. McGrath and R. Robinson, "Mapping Submerged Landscapes Using Multibeam Bathymetric Data: A case study from the north coast of Ireland", *International Journal of Nautical Archaeology*, 40 (1), 2011, pp. 99-112.

[5] J. Gao, "Bathymetric mapping by means of remote sensing: methods, accuracy and limitations", Progress In Physical Geography, 33, 2009, pp. 103–116.

[6] A. M. Duda, and M. T. El-Ashry, "Addressing the global water and environment crises through integrated approaches to the management of land, water and ecological resources", *Water International*, 25 (1), 2000 pp. 115-126.

[7] S. N. Lane, R. M. Westaway, and D. M. Hicks, "Estimation of erosion and deposition volumes in a large gravel-bed, braided river using synoptic remote sensing", *Earth surface processes and landforms*, 28 (3), 2003, pp. 249-271.

[8] P. J. Kinzel, C. W. Wright, J. M. Nelson and A. R Burman, "Evaluation of an experimental LIDAR for surveying a shallow, braided, sand bedded river", *Journal of Hydraulic Engineering*, 133 (7), 2007, pp. 838–842.

[9] D. Feurer, J. S. Bailly, C. Puech, Y. LeCoarer, and A. Viau, "Very high resolution mapping of river immersed topography by remote sensing," *Progress in Physical Geography*, 32 (4), 2008, pp. 1–17.

[10] T. B. Vermeyen, "Using an ADCP, depth sounder, and GPS for bathymetric surveys", *Proceedings of the World Environmental and Water Resources Congress*, Omaha, Nebraska, 21–25 May, 1996.

[11] R. L. Dinehart and J. R. Burau, "Repeated surveys by acoustic Doppler current profiler for flow and sediment dynamics", *Journal of Hydrology* 314, 2005, pp. 1–21.

[12] L. J. Poppe, S. D. Ackerman, E. F. Doran, A. L. Beaver, J. M. Crocker, and P. T. Schattgen, "Interpolation of Reconnaissance Multibeam Bathymetry from north-central Long Island Sound", *Open File Report 2005-1145, U.S. Geological Society*, 2006.

[13] R. L. Ferrari, "Folsom Lake Sedimentation Study", *Bureau of Reclamation Report, Technical Service Centre*, Denver, CO, 2005.

[14] H. Wirth and T. Brüggemann, "The development of a multiple transducer multi-beam echo sounder system for very shallow waters", *FIG Working Week Bridging the Gap between Cultures Marrakech, Morocco*, 18-22 May, 2011.

[15] J. Legleiter, A. Roberts and L. Rick, "Spectrally based remote sensing of river bathymetry", *Earth Surface Processes and Landforms*, 34, 2009, pp. 1039–1059.

[16] M. A. Fonstad, W. A. Marcus, "Remote sensing of stream depths with hydraulically assisted bathymetry (HAB) models", *Geomorphology*, 72 (1–4), 2005, pp. 320-339.

[17] G.C. Guenther, A.G. Cunningham, P.E. LaRocque, and D.J. Reid, "Meeting the accuracy challenge in airborne LiDAR bathymetry", *Proc. 20th EARSeL Symposium: Workshop on Lidar Remote Sensing of Land and Sea*, June 16-17, Dresden, Germany, 2000.

[18] R. C. Hilldale and D. Raff, "Assessing the ability of airborne LIDAR to map river bathymetry", *Earth Surface Processes and Landforms*, 33 (5), 2007, pp. 773–783.

[19] J. S. Bailly, Y. Le Coarer, P. Languille, C. J. Stigermark, and T. Allouis, "Geostatistical Estimations of bathymetric LIDAR errors on rivers", *Earth Surface Process and Landforms*, 35, 2010, pp. 1199-1210.

[20] S. Peeri, J.V Gardner, L.G Ward and J.R. Morrison, "The seafloor: A key factor in lidar bottom detection", *IEEE Transactions on Geoscience and Remote Sensing*, 49 (3), 2011, 1150-1157.

[21] J. L. Irish, and W. J. Lillycrop, "Scanning laser mapping of the coastal zone: the SHOALS system," *ISPRS Journal of Photogrammetry and Remote Sensing*, 54 (2-3), 1999, pp. 123-129.

[22] A. Cunningham, W. J. Lillycrop, G. C. Guenther and M. Brooks, "Shallow water laser bathymetry: accomplishments and applications", *Proceedings of the XVth Oceanology International Exhibition & Conference*, Brighton, 3, 1998, pp. 277–288.

[23] J. Feigels, "LIDARs for oceanological research: criteria for comparison, main limitations, perspectives," *Ocean Optics XI*, 1750, 1992, pp. 473–484.

[24] H. M. Tulldahl and K. O. Steinvall, "Analytical Waveform Generation from Small Objects in LIDAR Bathymetry", *Applied Optics*, 38 (6), 1999, pp. 1021-1039.

[25] H. M. Tulldahl and K. O. Steinvall, "Simulation of sea surface wave influence on small target detection with airborne laser depth sounding," *Applied Optics*, 42 (12), 2004, pp. 2462 – 2483.

[26] T. Allouis, J.-S. Bailly, Y. Pastol and C. Le Roux, "Comparison of lidar waveform processing methods for very shallow water bathymetry using Raman, near-infrared and green signals", *Earth Surface Process and Landforms*, 35, 2010, pp. 640–650.

[27] S. Peeri and W. Philpot, "Increasing the existence of very shallow-water lidar measurements using the red-channel waveforms", *IEEE Transactions on Geoscience and Remote Sensing*, 45 (5), 2007, pp. 1217–1223.

[28] C. Flener, E. Lotsari, P. Alho and J. Käyhkö, "Comparison of empirical and theoretical remote sensing based bathymetry models in river environments", *River Research and Applications*, 28 (1), 2012, pp.118-133.

[29] G. J. Perry, "Post-processing in laser airborne bathymetry systems", *Proc. ROPME/PERSGA/IHB Workshop on Hydrographic Activities in the ROPME Sea Area and Red Sea*, October 24-27, Kuwait, 1999.

[30] W. J. Lillycrop, L. E. Parson, J. L. Irish, and M. W. Brooks, "Hydrographic surveying with an airborne LiDAR survey system" *Presented at the Second International Airborne Remote Sensing Conference and Exhibition*, San Francisco, CA, 24–27 June, 1996.

[31] X. Sun, J.B. Abshire, D. Yi and H. A. Fricker, "ICESat receiver signal dynamic range assessment and correction of range bias due to saturation", *EOS Trans. AGU*, 86 (52), 2005.

[32] D. T. Kokkinos, G. Tzeremes and E. Armandillo, "Determination of backscatter ratio and depolarization ratio by mobile lidar measurements

in support of EARTHCARE and AEOLUS missions", *Workshop on Lidar Measurements in Latin America*, 2011.

[33] H. Abdallah, N. Baghdadi, J. S. Bailly, Y. Pastol and F. Fabre, "Wa-LiD: A New LiDAR Simulator for Waters," IEEE *Geoscience and Remote Sensing Letters*, 9 (5), 2012, pp. 744-748.

[34] G.C. Guenther, "Airborne Laser Hydrography, system design and performance factors," *NOAA Professional Paper Ser. NOS1* (National Oceanic and Atmospheric Administration, Rockville, Md.), 1985.

[35] R. L. Cook, and K. E. Torrance, "A Reflectance Model for Computer Graphics," *ACM Transactions on Graphics*, 1, 1982, pp. 7 – 24.

[36] R. A. Smith, J. L. Irish and M. Q. Smith, "Airborne Lidar and airborne hyperspectral imagery: a fusion of two proven sensors for improved hydrographic surveying", *Proceedings of Canadian Hydrographic Conference* 2000, Montreal (Canada), pp. 10

[37] A. Bricaud, A. Morel and L. Prieur, "Absorption by dissolved organic matter of the sea (yellow substance) in the UV and visible domains," *Limnology and Oceanography*, 26 (1), 1981, pp. 43-53.

[38] Z. Liu, I. Matui and N. Sugimoto, "High-spectral-resolution lidar using an iodine absorption filter for atmospheric measurements", *Optical Engineering*, 38, 1999, pp.1661-1670.

[39] E. V. Browell, S. Ismail and W. B., "Grant, Differential absorption lidar (DIAL) measurements from air and space", *Applied Physics B: Lasers and Optics*, 67 (4), 1998, pp. 399-410.

[40] T. Allouis, S. Durrieu, P. Chazette, J.-S. Bailly, J. Cuesta, C. Véga, P. Flamant and P. Couteron, "Potential of an ultraviolet, medium-footprint lidar prototype for retrieving forest structure", *ISPRS Journal of Photogrammetry and Remote Sensing*, 66 (6),2011, pp. S92-S102.

[41] D. Morancais, R. Sesselmann, G. Benedetti-Michelangeli and M. Hueber, "The atmospheric lidar instrument (ATLID)", *Acta Astronautica*, 34, 1994, pp. 63-67.

[42] M. Lamboni, D. Makowski, S. Lehuger, B. Gabrielle, and H. Monod, "Multivariate global sensitivity analysis for dynamic crop models", *Field Crops Research*, 113 (3), 2009, pp. 312-320.

[43] T. K. Cossio, K. C. Slatton, W. E. Carter, K. Y. Shrestha, D. Harding, "Predicting Small Target Detection Performance of Low-SNR Airborne Lidar," *Selected Topics in Applied Earth Observations and Remote Sensing, IEEE Journal of* , 3 (4), 2010, pp.672-688.

[44] M. S. Belen'kii, "Effect of atmospheric turbulence on heterodyne lidar performance," *Appl. Opt*. 32, 1993, pp. 5368–5372.

[45] R. Agishev, A. Comeron, B. Gross, F. Moshary, S. Ahmed and A. Gilerson, "Application of the method of decomposition of lidar signal-to-noise ratio to the assessment of laser instruments for gaseous pollution detection", *Applied Physics B*, 79 (2), 2004, pp. 255-264.

[46] M. Rijkeboer, A. G. Dekker and H. J. Gons, "Subsurface irradiance reflectance spectra of inland waters differing in morphometry and hydrology", *Aquat. Ecol.*, 31, 1998, pp. 313–323.

[47] J.B. Keller, "Shallow-water theory for arbitrary slopes of the bottom", J. *Fluid Mech*., 489, 2003, pp. 345–348.

[48] F. Wobus, G.I. Shapiro, M.A. Maqueda, and J.M Huthnance, "Numerical simulations of dense water cascading on a steep slope", *Journal of Marine Research*, 69 (2-3), 2011, pp. 391-415.

[49] L. Leopold and T. Maddock, "The hydraulic geometry of stream channels and some physiographic implications", *U.S. geol Surv. Prof. Pap.*, 252, 1953, pp. 9-16.

[50] P. Beckmann, and A. Spizzochino, *The scatter of electromagnetic waves from rough Surfaces*, Norwood, MA: Artech House, 1987.

[51] E. J. Hochberg, M. J. Atkinson and S. Andrefouet, "Spectral reflectance of coral reef bottom-types worldwide and implications for coral reef remote sensing", *Remote Sensing of Environment*, 85, 2003, pp. 159–173.

[52] D.R. Lyzenga, "Passive remote-sensing techniques for mapping water depth and bottom features", *Applied Optics*, 17, 1978, pp. 379–383.

[53] J. T. O. Kirk, *Light and Photosynthesis in Aquatic Ecosystems*, Cambridge, UK, New York: Cambridge University, 3rd edition, 2011, 662 pp.

[54] C. D. Mobley, *Light and Water: Radiative Transfer in Natural Waters*, *Academic*, San Diego, Calif, 1994.

[55] L. Sipelgas, H. Arst, U. Raudsepp, T. Kouts and A. Lindfors, "Optical properties of coastal waters of north western Estonia: in situ measurements", *Boreal Environ. Res.*, 9 (5), 2004, pp. 447–456.

[56] J. A. Warrick, L. A. K. Mertes, D. A. Siegel, and C. Mackenzie, "Estimating suspended sediment concentrations in turbid coastal waters of the Santa Barbara Channel with SeaWiFS" *International Journal of Remote Sensing*, 25, 2004, pp. 1995-2002.

[57] L. C. Bowling, "Optical properties, nutrients and phytoplankton of freshwater coastal lakes in south- east Queensland", *Aust. J. Mar. Freshwat. Res*. 39, 1988, pp. 805–815.

[58] A. A. Gitelson., R. Khanbilvardi, B. Shteinman and Y. Yacobi, "Remote estimation of phytoplankton distribution in aquatic ecosystems Engineering Construction and Operations in Challenging Environments Earth and Space", *Proceedings of the Ninth Biennial ASCE Aerospace Division International Conference*, 2004, pp. 255-262.

[59] D. H. Jewson and J. A. Taylor, "The influence of turbidity on net phytoplankton photosynthesis in some Irish lakes", *Freshwater Biology*, 8, 1978, pp. 573–584.

[60] M. A. Moline, T. K. Frazer, R. Chant, S. Glenn, C. A. Jacoby, J. R. Reinfelder, J. Yost, M. Zhou and O. Schofield, "Biological Responses in a Dynamic Buoyant River Plume", *Oceanography*, 21 (4), 2008, pp. 70-89.

[61] M. L. Laanen, "Improving the remote sensing of Coloured Dissolved Organic Matter in inland freshwaters", Doctoral Theses - Earth and Life Sciences, Vrije university, Amesterdam, 2007.

[62] P. Cipollini and G. Corsini, "The effect of yellow substance on pigment concentration retrieval using 'blue to green' ratio", *Proceeding of IEEE International Geoscience and Remote Sensing Symposium, IGARSS-94*, 1994, pp. 772-777.

[63] I. M. Sobol, "Sensitivity estimates for non linear mathematical models", *Mathematical Modelling and Computational Experiments*, 1, 407–414, 1994.

[64] P. Bratley and B. Fox, "Implementing Sobol's quasi random sequence generator", *ACM Transactions on Mathematical Software*, 14 (1), 1988, pp. 88-100.

[65] S. Tarantola and M. Koda, "Improving Random Balance Designs For The Estimation Of First Order Sensitivity Indices", *Procedia - Social and Behavioral Sciences*, 2 (6), 1997, pp. 7753-7754.

[66] K. Campbell, M. D. McKay and B. J. Williams, "Sensitivity analysis when model outputs are functions", *Reliability Engineering and System Safety*, 91, 2006, pp. 1468–1472.

[67] B. Jutzi, and U. Stilla, "Range determination with waveform recording laser systems using a Wiener Filter," *ISPRS Journal of Photogrammetry and Remote Sensing*, 61 (2), 2006, pp. 95–107.

[68] B. Long, A. Cottin and A. Collin, "What Optech's Bathymetric LiDAR Sees Underwater", *Geoscience and Remote Sensing Symposium, Barcelone, IEEE International*, July 23-28, 2007, pp. 3170-3173.

[69] C. Mallet, F. Lafarge, F. Bretar, U. Soergel, C. Heipke, "Lidar waveform modelling using a marked point process", *Proceedings - International Conference on Image Processing, ICIP*, 2009, pp. 1713-1716.

[70] M. Evans, N. Hastings and B. Peacock, "Triangular Distribution", *Ch. 40 in Statistical Distributions, 3rd edition New York: Wiley*, 2000, pp. 187-188.

[71] P. Rosin and E. Rammler, "The Laws Governing the Fineness of Powdered Coal", *Journal of the Institute of Fuel* **7**, 1933, pp. 29–36.

[72] M. A. Hofton, J. B. Minster and J. B. Blair, "Decomposition of laser altimeter waveforms", *IEEE Transactions on Geoscience and Remote Sensing*, 38 (4 II), 2000, pp. 1989-1996.

[73] J. Reitberger, P. Krzystek, U. Stilla, "Analysis of full waveform LIDAR data for the classification of deciduous and coniferous trees", *International Journal of Remote Sensing*, 29 (5), 2008, pp. 1407-1431.

[74] M. Imaki and T. Kobayashi, "Ultraviolet high-spectral-resolution Doppler LiDAR for measuring wind field and aerosol optical properties," Appl. Opt., 44, 2005, pp. 6023-6030.

[75] A. Morel, B. Gentili, H. Claustre, M. Babin, A. Bricaud, J. Ras and F. Tièche, "Optical properties of the 'clearest' natural waters", *Limnology and Oceanography*, 52 (1), 2007, pp. 217–229.

[76] M. E. Charlton, A. R. G. Large and I. C., "Application of airborne lidar in riverenvironments: The River Coquet", *Northumberland, UK. Earth Surface Processes and Landforms*, 28, 2003, pp. 299-306.

[77] R. F. Brinkman and C. O'Neill, "LiDAR and photogrammetric mapping", *The Military Engineer*, May-June 2000.

[78] H. J. Zwally, B. Schutz, W. Abdalati, J. Abshire, C. Bentley, A. Brenner, J. Bufton, J. Dezio, D. Hancock, D. Harding, T. Herring, B. Minster, K. Quinn, S. Palm, J. Spinhirne, and R. Thomas, "ICESat's laser measurements of polar ice, atmosphere, ocean, and land," *Journal of Geodynamics*, 34 (3-4), 2002, pp. 405-445.

[79] T.J. Urban, B. E. Schutz and A.L Neuenschwander, "A survey of ICESat coastal altimetry applications: continental coast, open ocean island, and inland river",*Terrestrial, Atmospheric and Oceanic Sciences*, 19 (1-2), 2008, pp.1–19.

[80] J.W. Marini and C.W. Murray, "Correction Of Laser Range Tracking Data For Atmospheric Refraction At Elevation Angles Above 10°", NASA Technical Report 1973.

[81] H. Abdallah, J.-S. Bailly, N. Baghdadi, and N. Lemarquand, "Improving the assessment of ICESat water altimetry accuracy accounting for autocorrelation", *ISPRS Journal of Photogrammetry and Remote Sensing*, 66(6), 2011, pp. 833-844.

[82] J.W Chipman and T.M. Lillesand, "Satellite-based assessment of the dynamics of new lakes in southern Egypt", *International Journal of Remote Sensing*, 28 (19), 2007, pp. 4365–4379.

List of Tables

TABLE 1. SENSOR PARAMETER VALUES OF THE TWO INVESTIGATED LIDAR SATELLITE SENSORS (UV AND GREEN).

System parameters	Units	Sensor 1 (355 nm)	Sensor 2 (532 nm)
Pulse duration (T_0)	ns	3	3.5
Digitizing frequency	GHz	1	1
Receiver Area (A_R)	m²	0.63	0.63
Emitted Power (P_e)	MW	1.4	0.4
Incidence angle (θ)	deg	0	0
Detector responsivity (R_λ)	A/W	0.15	0.25
Divergence angle (γ)	µrd	16	60
Spot size	m	8	30
Field of view (FOV)	µrd	24	90
Altitude (H)	km	500	500
Emitted Optical efficiencies (η_e)		0.8	0.8
Received Optical efficiencies (η_R)		0.5	0.5
Loss factor (F)		1	1
Receiver obscuration (γ_r)		0.1	0.1
Electrical bandwidth (B)	MHz	500	500
Excess noise (G)		3	3
Dark current (Id)	A	10^{-10}	10^{-10}

TABLE 2. RANGE VALUES (MINIMUM-MAXIMUM) OF WATER PARAMETERS FOR ALL WATER TYPES (SURFACE AND BOTTOM SURFACE PARAMETERS). μ and σ DENOTE THE MEAN AND THE STANDARD DEVIATION OF THE LOG-NORMAL DENSITY FUNCTION.

Water Parameters		unit	Range values	Distribution
S_s	Surface slope	°	[0 – 1]	Uniform
S_b	Bottom slope	°	[0 – 35]	Log-normal (μ=3°, σ=6°)
k_s	Specular bidirectional reflectance	-	[0.6 – 0.9]	Uniform
r	Rms of facet slope (rugosity)	-	[0 – 0.5]	Uniform
R_b	Bottom Albedo	-	[0.05 – 0.17]	Uniform

TABLE 3. RANGE VALUES (MINIMUM-MAXIMUM) OF CONCENTRATIONS OF YELLOW SUBSTANCES AY0, PHYTOPLANKTON CPH AND SEDIMENT S FOR THE FOUR CONSIDERED WATER TYPES.

Type	**a_{y0} (m^{-1})**	**Reference**	C_{ph} **(mg m^{-3})**	**Reference**	**S (mg l^{-1})**	**Reference**
Coastal	0,06 – 3.82	[53]-[55]	1-50	NASA/GSFC	2.6-200	[56]
Shallow Lake	0.8 - 14.2	[53], [57]	4-468	[46]	3-100	[46]; USGS
Deep lake	0.1- 4.9	[46], [53], [57]	1-150	[58]	1-14	[46]
River	0.2 -19.1	[53], [59]	12-100	[46], [60]	1-273	USGS
Distribution	Log-normal	[61]	Log-normal	[61], [62]	Log-normal	[61], [62]

TABLE 4. MAXIMUM OF DOMINANT WATER PARAMETERS (S, A_{Y0}, C_{PH}) CORRESPONDING TO WAVEFORMS WITH DETECTABLE BOTTOMS (--=NO WAVEFORM AVAILABLE WITH A DETECTABLE BOTTOM WAS FOUND). MAXIMA ARE PRESENTED FOR THE TWO STUDIED LIDAR SENSORS (UV AND GREEN) FOR EACH WATER TYPE (COASTAL WATERS, RIVERS, DEEP LAKES AND SHALLOW LAKES) AND FOR DIFFERENT WATER DEPTHS (1, 2, 3, 5, 10 AND 15 M).

Green	**Coastal water**			**River**			**Deep lake**			**Shallow Lake**		
Depth	**max S**	**max a_{y0}**	**max C_{ph}**	**max S**	**max a_{y0}**	**max C_{ph}**	**max S**	**max a_{y0}**	**max C_{ph}**	**max S**	**max a_{y0}**	**max C_{ph}**
1m	76	4,5	190	56	5,1	285	41	4,7	443	59	5,3	436
2m	50	2,5	190	42	2,7	198	37	3,4	275	47	3,6	262
3m	34	2,2	113	17	1,7	109	20	2,2	128	20	2	146
5m	26	1,1	76	8	1	69	15	1,6	90	15	1,6	66
10m	15	0,7	44	5	0,6	37	12	1	48	--	--	--
15m	9	0,3	34	--	--	--	7	0,5	23	--	--	--
UV	**Coastal water**			**River**			**Deep lake**			**Shallow Lake**		
1m	30	0,4	190	16	0,4	106	15	0,5	421	--	--	--
2m	20	0,4	180	7	0,4	97	12	0,4	152	--	--	--
3m	15	0,2	105	--	--	--	10	0,3	128	--	--	--
5m	8	0,1	54	--	--	--	6	0,1	69	--	--	--
10m	6	0,1	31	--	--	--	--	--	--	--	--	--
15m	--	--	--	--	--	--	--	--	--	--	--	--

TABLE 5. MINIMUM AND MAXIMUM OF SNRS CORRESPONDING TO WAVEFORMS WITH DETECTABLE BOTTOMS. (--=NO WAVEFORM WITH DETECTABLE BOTTOM WAS FOUND AT THIS DEPTH FOR THIS WATER TYPE).

Green	**Coastal water**		**River**		**Deep lake**		**Shallow lake**	
Depth	**min SNR**	**max SNR**	**min SNR**	**max SNR**	**min SNR**	**max SNR**	**min SNR**	**max SNR**
1m	89	1810	83	1374	84	1852	60	1066
2m	14	1608	15	717	15	993	8	498
3m	10	1124	10	364	7,9	567	4,4	191
5m	4,1	1078	4,7	243	3,6	562	3,8	144
10m	3,5	789	3,9	180	2,9	377	--	--
15m	3,3	603	--	--	2,2	232	--	--
UV	**Coastal water**		**River**		**Deep lake**		**Shallow lake**	
Depth	**min SNR**	**max SNR**	**min SNR**	**max SNR**	**min SNR**	**max SNR**	**min SNR**	**max SNR**
1m	4,2	2401	9,1	647	6,7	1040	--	--
2m	1,9	1511	6,4	156	2,9	393	--	--
3m	2.7	968	--	--	2,6	206	--	--
5m	1,8	842	--	--	1,74	98	--	--
10m	1,1	571	--	--	NA	NA	--	--
15m	--	--	--	--	NA	NA	--	--

List of Figures

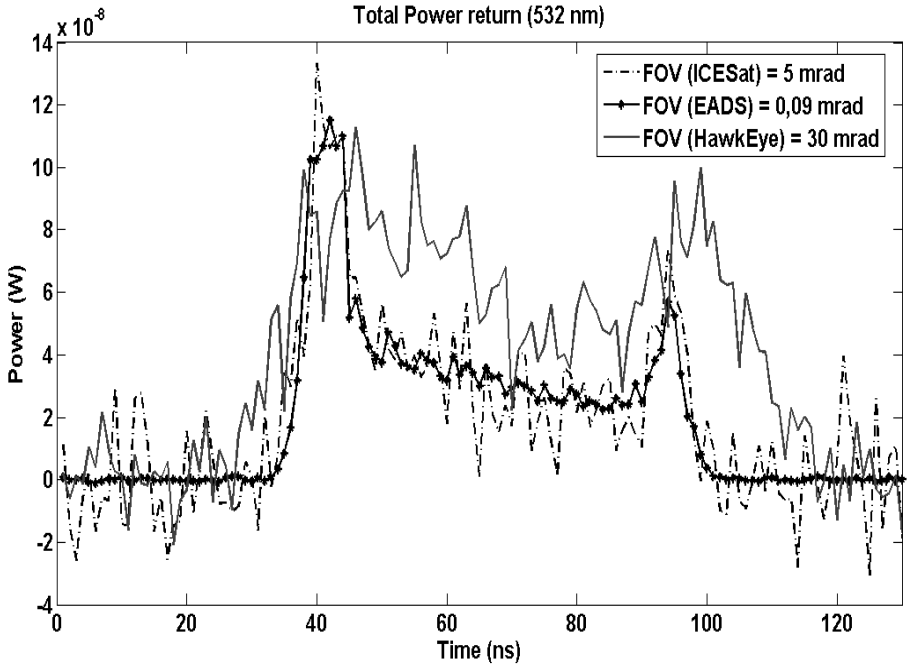

Fig. 1. Simulated 532 nm waveforms with different FOV angles (water depth=5m).

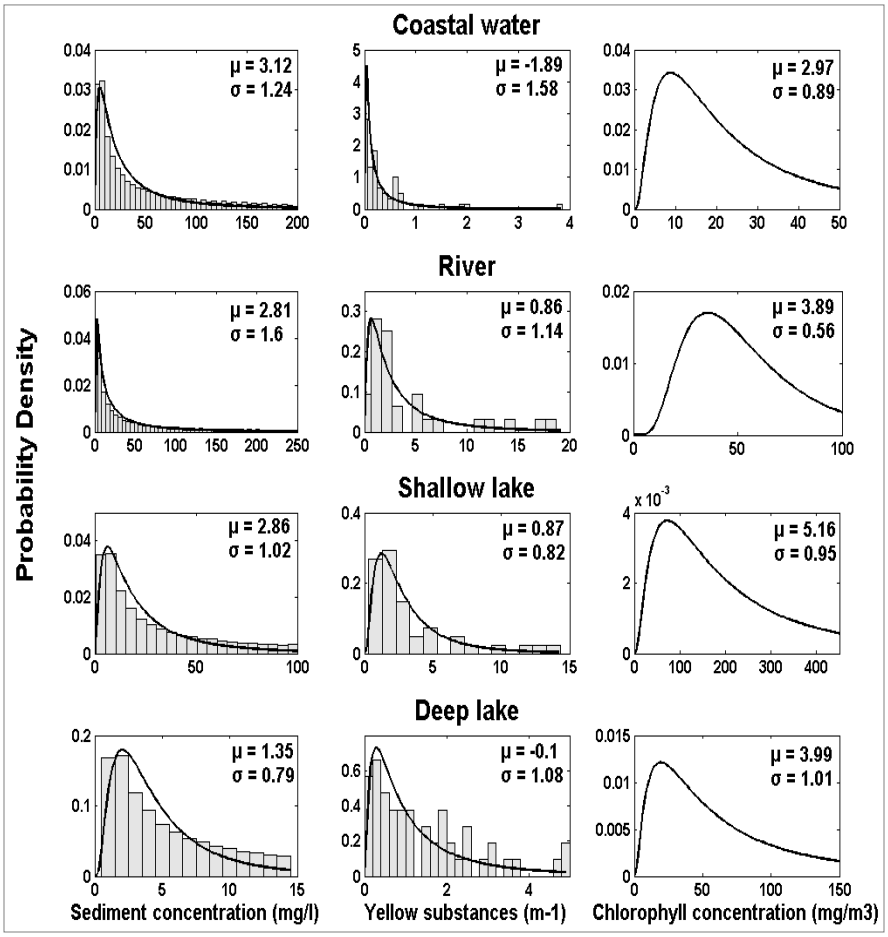

Fig. 2. Yellow substances a_{y0}, phytoplankton C_{ph} and sediment S concentration distributions for the four considered water types. μ and σ denote the mean and the standard deviation of the fitted log-normal density function (black curve), respectively.

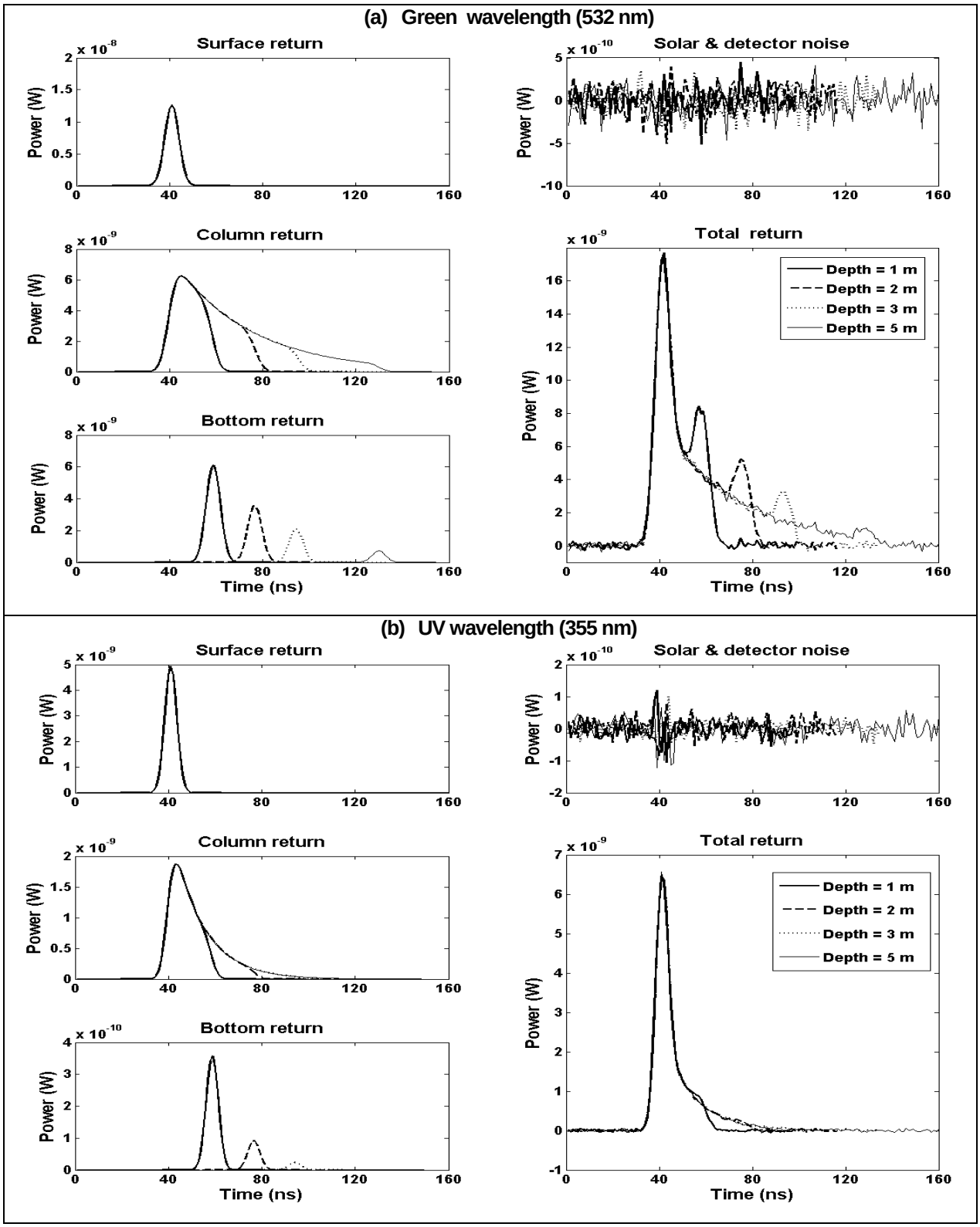

Fig. 3. Simulated LiDAR waveforms in coastal waters for 1, 2, 3 and 5 m water depths. (a) Green wavelength, and (b) UV wavelength.

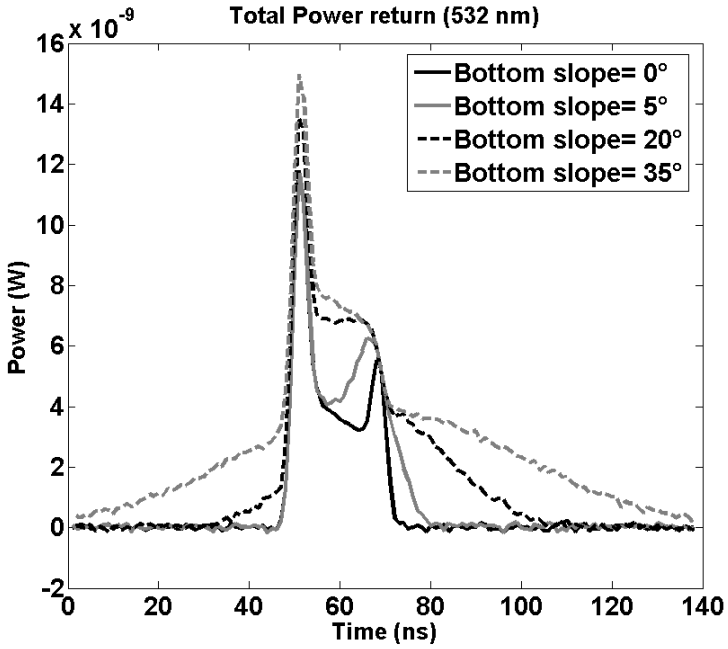

Fig. 4. Simulated green LiDAR waveforms in coastal waters for different bottom slope (S_b) at 2 m depth.

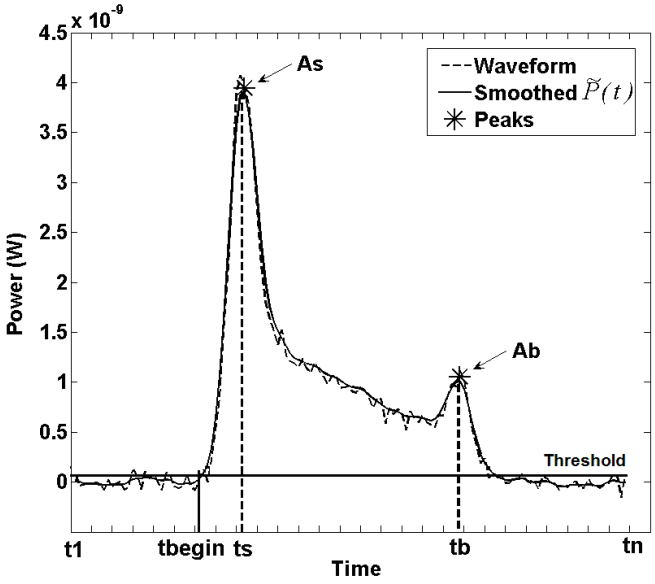

Fig. 5. Example of Wa-LiD waveform smoothed by the Wiener filter with a detectable bottom. t_{begin} and t_n are the beginning and the end of the time series, respectively; A_s and t_s are the amplitude and the time position of the surface peak; A_b and $t_{b.}$ are the amplitude and the time position of the bottom peak.

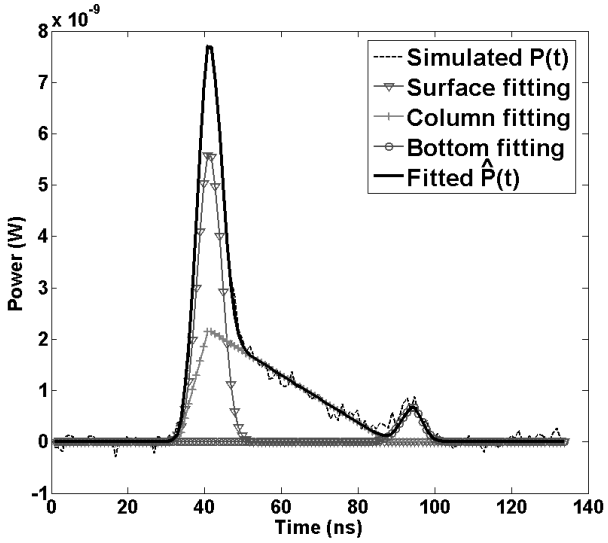

Fig. 6. Fitted simulated waveform with a sum of a Gaussian function (water surface peak), a triangle function (water column) and a Weibull function of water (bottom peak). The estimated depth is 2.9887 m for an actual depth of 3 m.

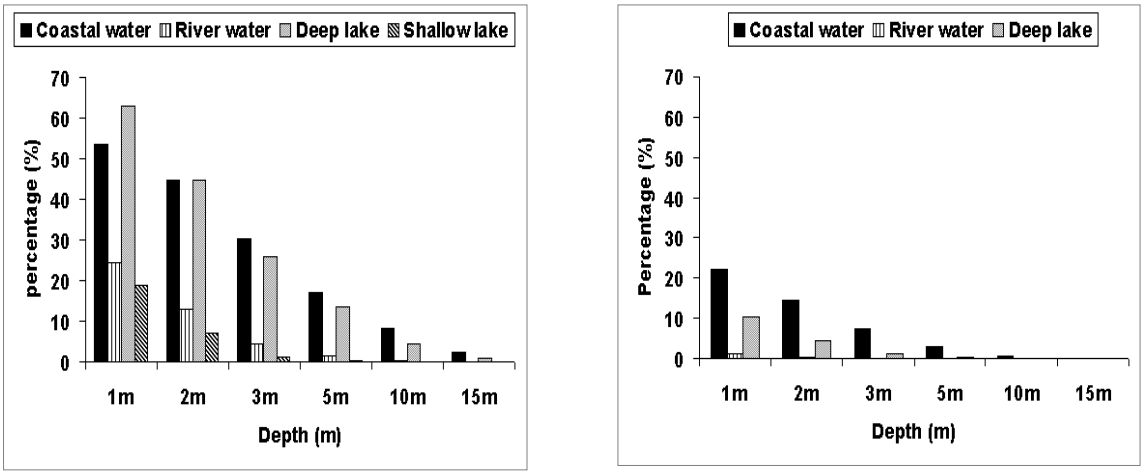

(a) Green configuration **(b) UV configuration**

Fig. 7. Global bathymetry probabilities.

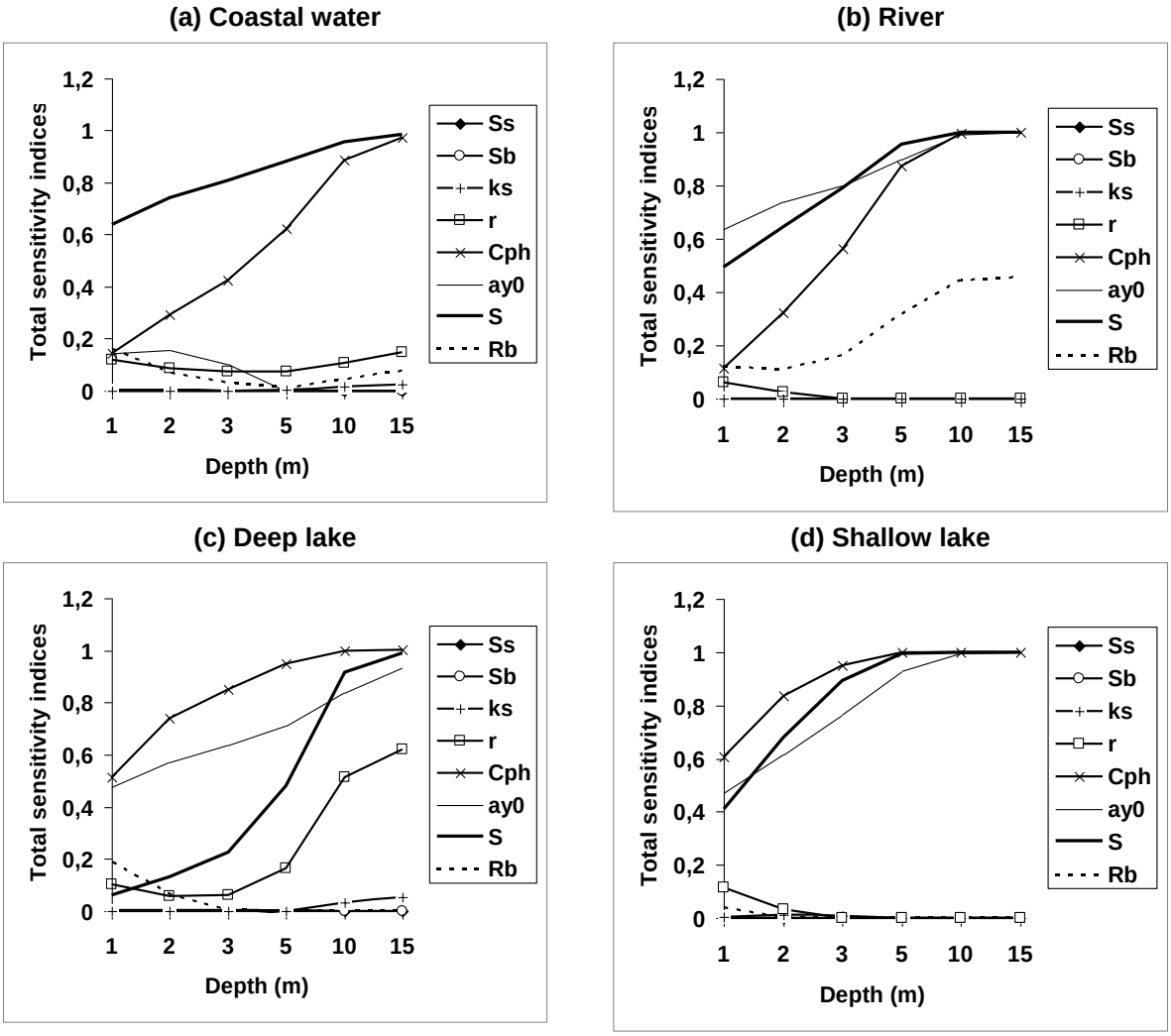

Fig. 8. Total Sobol indices related to water parameter variability for green sensor (532 nm) configuration across coastal water, river, deep and shallow lakes and for different depths (1, 2, 3, 5, 10 and 15 m). S_s: surface slope; S_b: bottom slope; k_s: specular bidirectional reflectance; r: root mean square of facet slope (water surface roughness); a_{y0}: yellow substances concentration; S: sediment concentration; C_{ph}: phytoplankton concentration and R_b: bottom albedo.

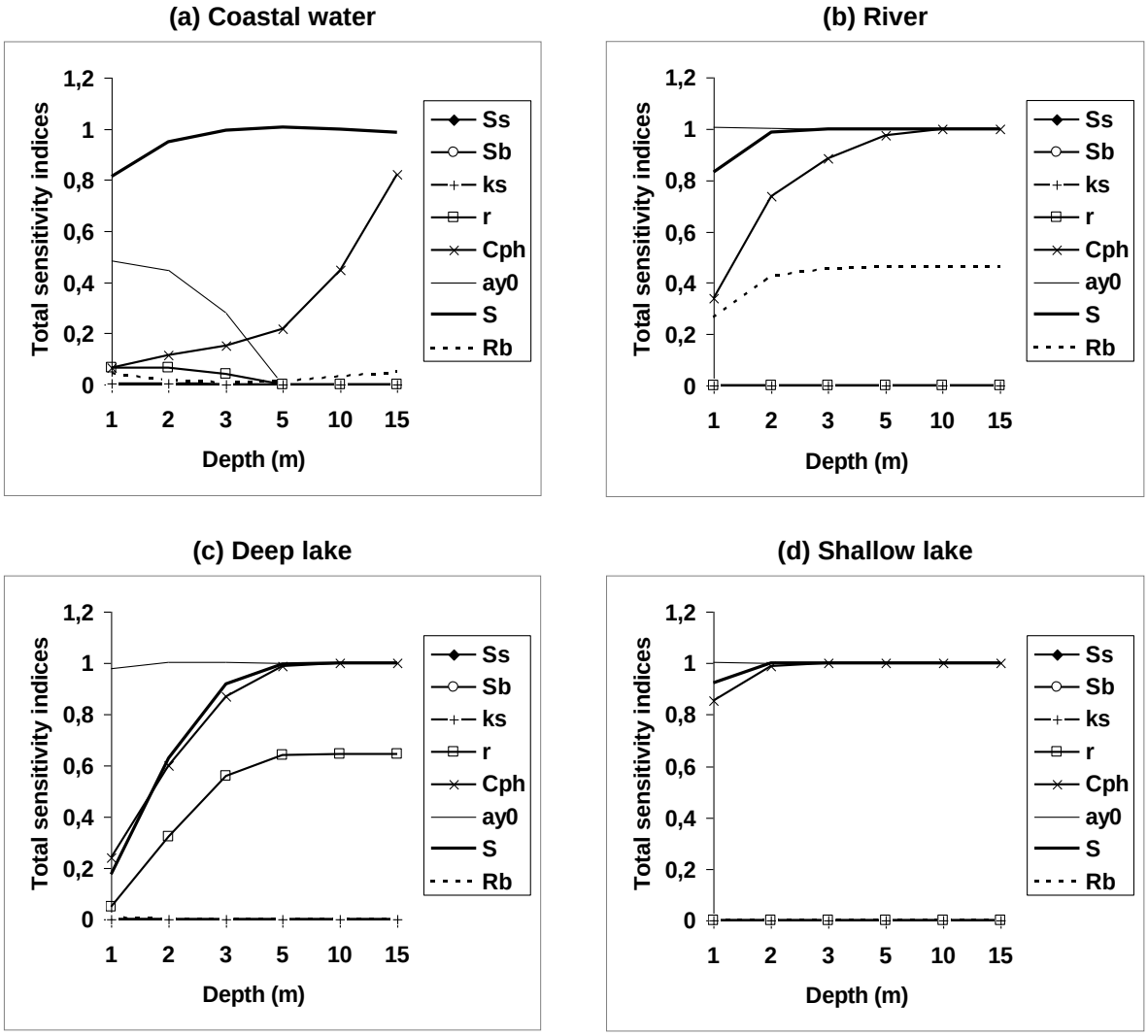

Fig. 9. Total Sobol indices related to water parameter variability for UV sensor (355 nm) across coastal water, river, deep and shallow lakes and for different depths (1, 2, 3, 5, 10 and 15 m). S_s: surface slope; S_b: bottom slope; k_s: specular bidirectional reflectance; r: root mean square of facet slope (water surface roughness); a_{y0}: yellow substances concentration; S: sediment concentration; C_{ph}: phytoplankton concentration and R_b: bottom albedo.

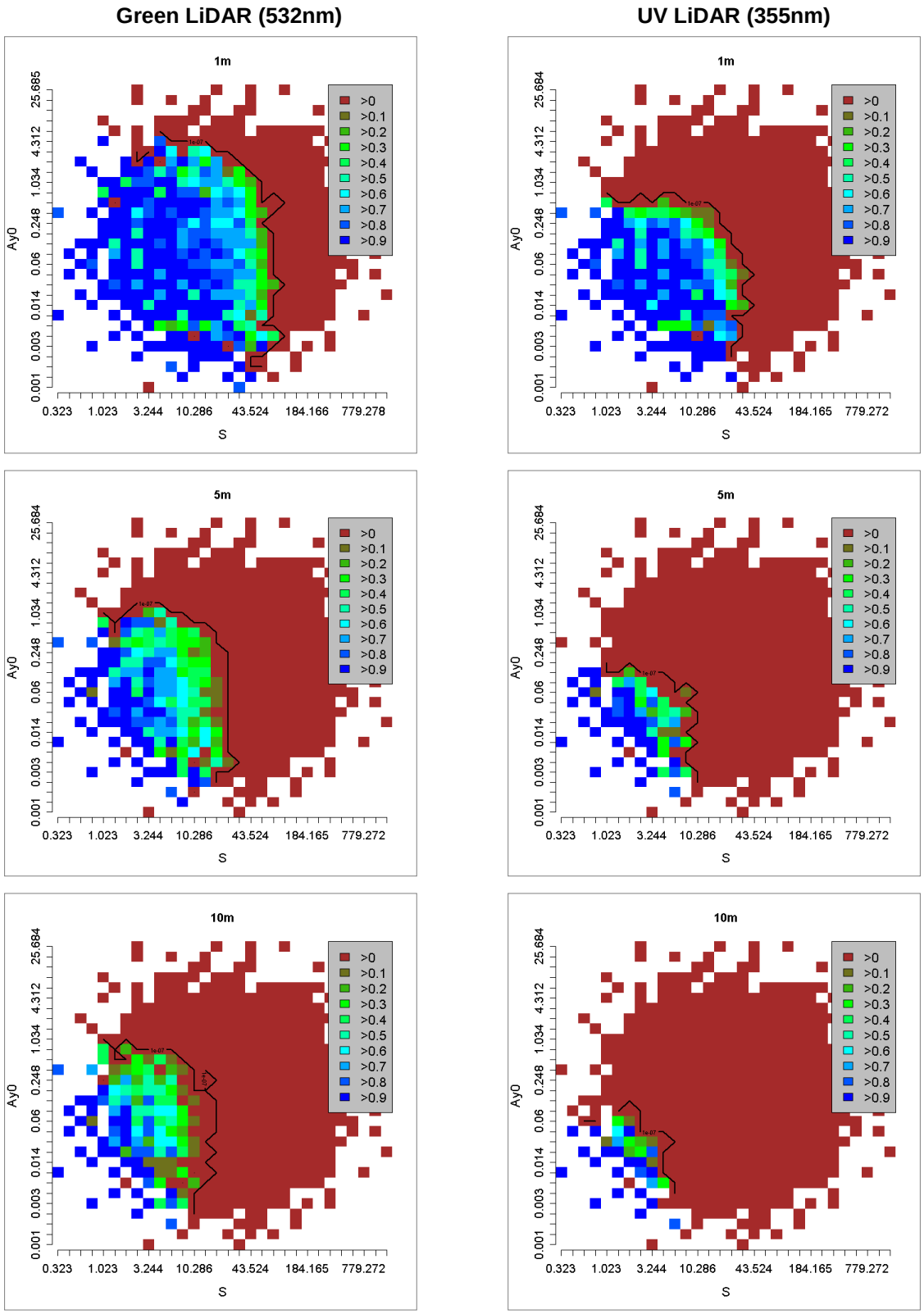

Fig. 10. Maps of bathymetry detection probability according to a_{y0} and S distributions in coastal water for 1, 5 and 10 m water depths for green and UV LiDARs (plotted with logarithmic scale). The black contour corresponds to very low probability values ($P=1e^{-7}$) and delineates the bathymetry detection area.

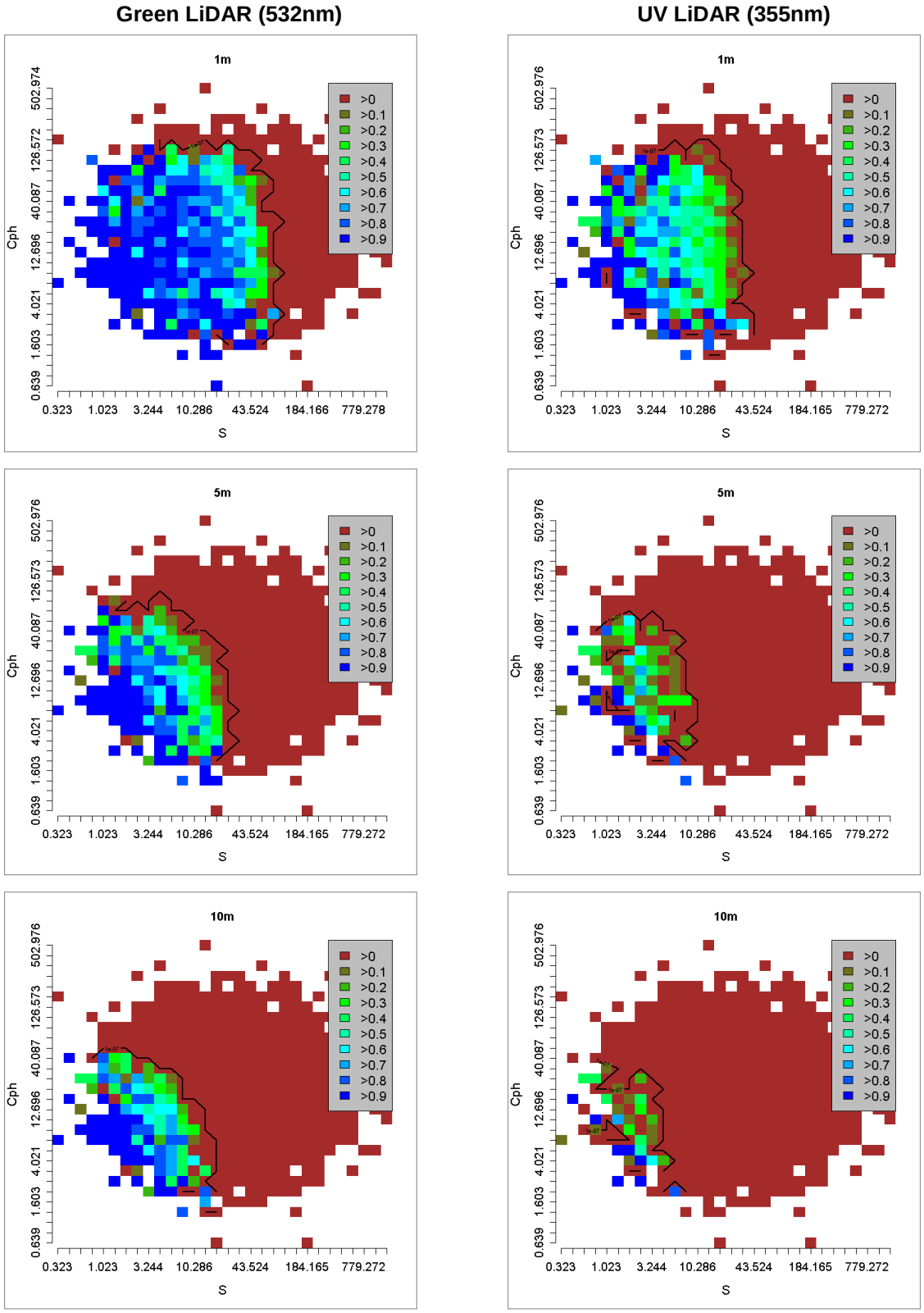

Fig. 11. Maps of bathymetry detection probability according to C_{ph} and S distributions in coastal water for 1, 5 and 10 m water depths for green and UV LiDARs (plotted with logarithmic scale). The black contour corresponds to very low probability values ($P=1e^{-7}$) and delineates the bathymetry detection area.

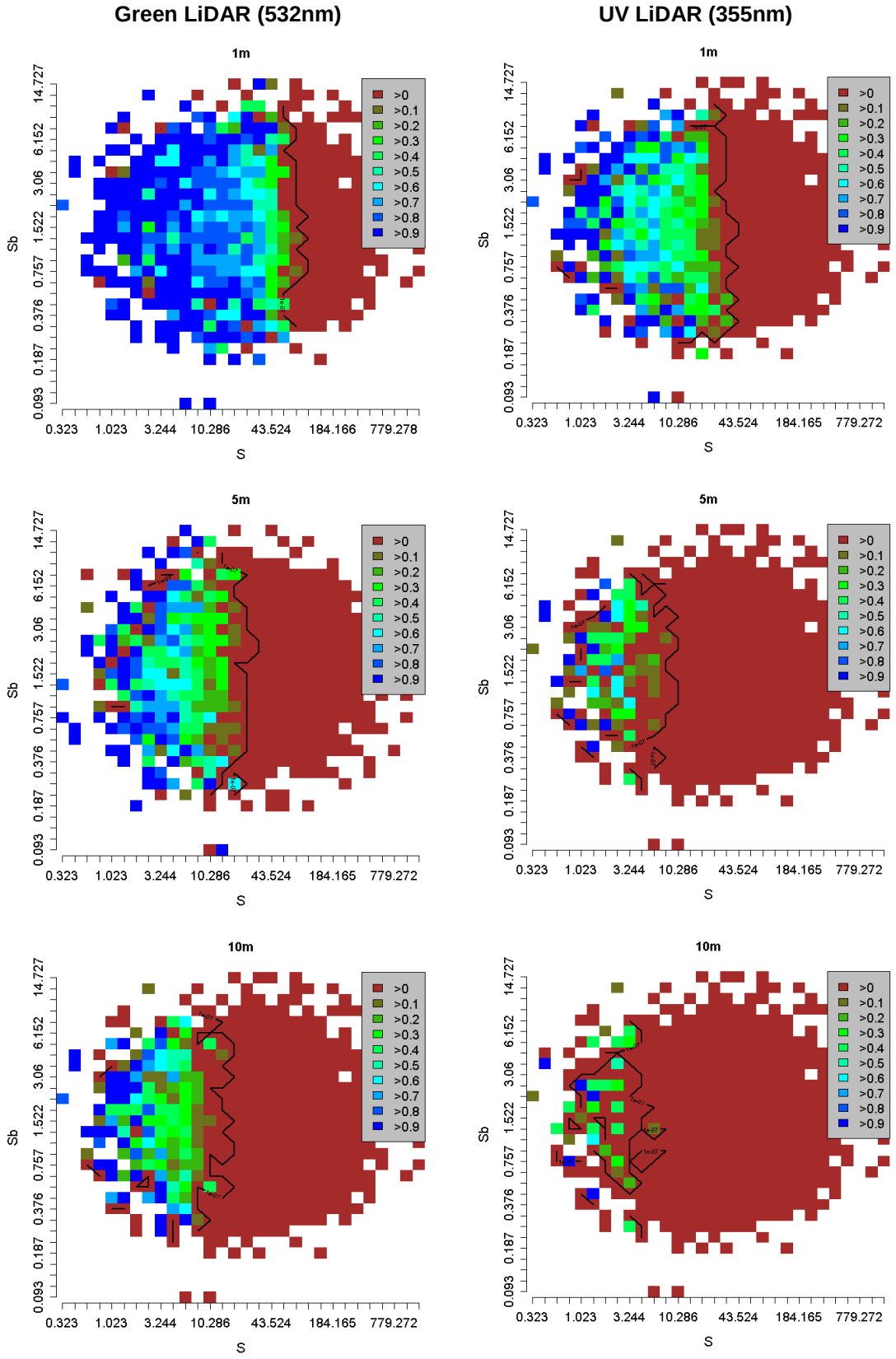

Fig. 12. Maps of bathymetry detection probability according to S_b and S distributions in coastal water for 1, 5 and 10 m water depths for green and UV LiDARs (plotted with logarithmic scale). The black contour corresponds to very low probability values ($P=1e^{-7}$) and delineates the bathymetry detection area.

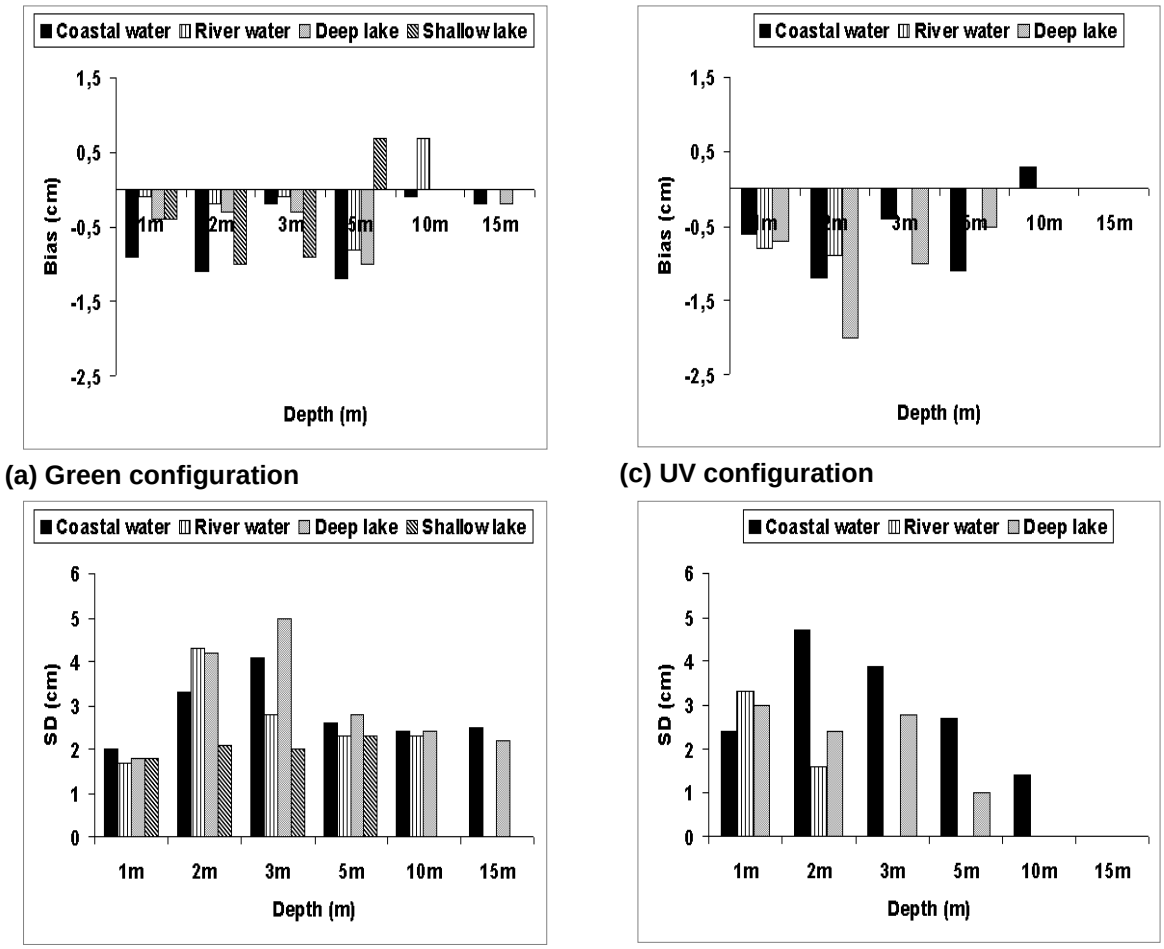

Fig. 13. Statistics on the bathymetry estimation errors: bias and standard deviations.

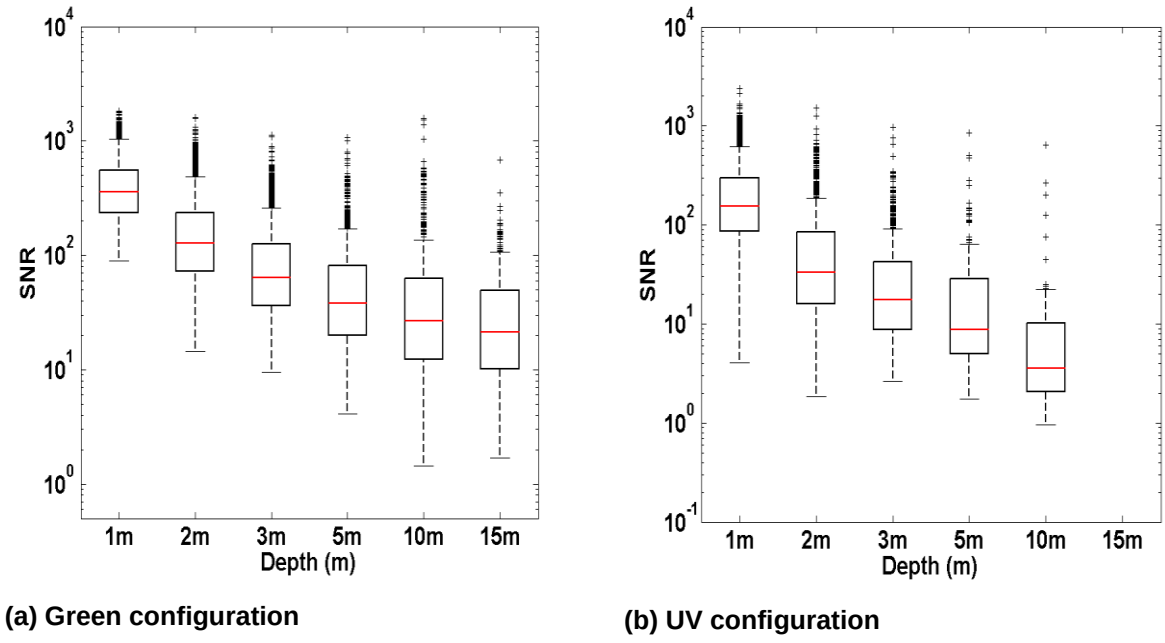

Fig. 14. Boxplots of SNRs (logarithmic scale) for waveforms with detectable bottoms at 1, 2, 3, 5, 10 and 15 m water depths in coastal waters for the green and UV sensors.

Conclusions et perspectives

Conclusions et perspectives

1. Conclusion

L'objectif de cette thèse était d'évaluer le potentiel de futurs capteurs LiDAR satellitaires pour estimer l'altimétrie et la bathymétrie des eaux de surfaces continentales et côtières. Une approche expérimentale puis une approche théorique basée sur des formes d'onde LiDAR simulées sont utilisées pour explorer les performances des LiDAR sur une large gamme de paramètres des milieux aquatiques. Les principaux résultats obtenus se résument comme suit :

1.1. Qualité des données altimétriques du capteur GLAS/ICESat-1 sur les eaux continentales :

ICESat-1 est à ce jour le seul capteur LiDAR satellitaire d'observation de la terre en mesure de fournir des données altimétriques acquises sur de nombreuses zones du globe entre 2003 et 2009. La qualité des données altimétriques du capteur GLAS sur les eaux continentales démontre le fort potentiel de la technique LiDAR pour l'estimation de l'altimétrie sur des surfaces en eau de grande taille. L'analyse des formes d'onde GLAS sur le lac Léman et les grands lacs américains a montré un phénomène de saturation du signal LiDAR. Les altitudes (ou hauteurs) calculées à partir des formes d'onde saturées sont imprécises. La correction de l'effet de saturation améliore nettement la qualité des estimations du niveau de l'eau. De ce fait, nous avons mis en évidence un phénomène de « décrochage » aux transitions terre-eau. En effet, lors de la transition terre-eau, le récepteur a besoin d'environ 0.25 s (soit 8 mesures ou 1,36 km) pour régler son gain et que les altitudes estimées à partir des données GLAS deviennent précises. Cette limitation est inhérente à la conception des chaines de détection et pourra être sûrement améliorée pour les futurs modèles. La distance moyenne de 1,36 km est donc la marge minimale à appliquer aux objets d'étude. Les objets d'études de petite taille, ne pouvant se voir appliquer une telle marge, ne peuvent donc être étudiés avec le satellite GLAS. A titre d'exemple la précision du satellite GLAS fut évaluée sur les cours d'eau en France. Seules 26 traces et une centaine d'empreintes GLAS ont été jugés

exploitables pour leur comparaison avec des mesures de référence provenant de l'ensemble de la base de données nationale sur l'eau (RNDE). Au final, la statistique d'erreur altimétrique RMSE estimée sur les cours d'eau en France est de 1,15 m environ. Peu précis sur l'altimétrie des niveaux des cours d'eau de petites tailles, GLAS n'est donc pas une alternative intéressante pour assurer leur surveillance.

Enfin, sur les grands lacs américains, nous avons mesuré puis analysé l'impact de l'autocorrélation temporelle entre les mesures successives du satellite GLAS/ICESat-1. Une autocorrélation significative a été observée pour 45% des traces. En moyenne, la prise en compte de l'autocorrélation dans l'incertitude des niveaux moyens des lacs donne une incertitude du niveau de l'eau moyen estimé 8 fois supérieure à ce qu'elle serait sans en tenir compte. Un biais global de 4,6 cm (sous-estimation de l'élévation par GLAS) et une incertitude d'écart type global de 11,6 cm ont ainsi été calculés.

Le lancement du capteur ICESat-II est prévu pour 2016 avec une taille d'empreintes de 50m espacés de 140m, suivant une fréquence d'émission de 50Hz et un FOV (Field of View) de 140 µrad (Abdalati et al., 2010). Pour GLAS/ICESat-I, ces paramètres étaient de 60m (au mieux), 170m, 40Hz et 140 mrad respectivement. Pour ICESat-II, deux options ont été étudiées pour l'acquisition des mesures (Abdalati et al., 2010):

- La première est une approche quadri-faisceaux. Dans cette configuration, un élément optique diffractif serait utilisé pour diviser le faisceau principal en quatre faisceaux distincts, orientés vers les coins d'un carré de plusieurs kilomètres de large et centrée sur le point nadir. Cette approche permet de bien caractériser la pente locale le long de la trace. Il augmente également la couverture spatiale en sur-échantillonnant le long de la trace. L'approche quadri-faisceaux, cependant, réduit considérablement la quantité d'énergie laser dans chaque faisceau, qui à son tour réduit le nombre de mesures efficaces qui seraient acquises à chaque faisceau.
- La deuxième approche utilise un type différent de système laser, un lidar micro-pulse (Degnan, 2002), pour mesurer une altitude de surface sur une bande de chaque côté du faisceau principal. Ce système utilise un laser vert à impulsions à haute répétition (10 kHz), moins d'énergie (100 µJ de), largeur

d'impulsion plus courte (~ 1 ns). Un émetteur laser unique ayant l'énergie du laser suffisante sera divisé en plusieurs faisceaux en utilisant un élément optique diffractif. L'architecture actuelle de l'instrument se compose d'un système de 9 faisceaux de petites empreintes (10 m) (Yu et al., 2010). Cette approche présente l'avantage significatif d'une couverture dense et d'une capacité de produire plus de données puisque le système est basé sur une possibilité de détecter le retour d'un photon unique dans chaque empreinte (récepteur par comptage de photons). Cette augmentation d'échantillonnage ainsi que les petites empreintes de 10m sont avantageux car ils devraient permettre de détecter des objets de petites tailles. De plus, ils permettraient d'améliorer la précision de la mesure altimétrique.

La configuration quadri-faisceaux pourrait également être réalisée avec des lasers multiples, mais l'utilisation simultanée de plusieurs lasers a un impact significatif sur les besoins en puissance ainsi que sur la durée de la mission. Pour cette raison, les considérations programmatiques et scientifiques ont abouti à la sélection du lidar micro-pulse (deuxième approche) pour la mise en œuvre de ICESat-II (masse < 10 kg, volume < 40 x 25 x 15 cm^3, puissance < 100 kw).

Reste à évaluer la qualité des spots des futurs capteurs ICESat-II à la transition terre-eau car on peut s’attendre à un meilleur ajustement du gain et donc une meilleure précision sur l’élévation des petits cours d’eau. En effet, pour surmonter le handicap posé par la saturation en milieu spéculaire très réfléchissant, les scientifiques proposent d'agrandir la surface de réception du détecteur et d'intégrer un meilleur système de contrôle de gain qui sera la mise à jour la plus importante pour ICESat-II (Abdalati et al., 2010). Si ICESat-II conjugue une précision et une haute répétitivité, il pourrait être un instrument précieux pour le suivi altimétrique des niveaux d'eau, et pourquoi pas des cours d'eau.

Pour ICESat-I, une grande partie des données n’est pas exploitable en raison du bruit atmosphérique (Abdalati et al., 2010). Un champ de vue (FOV) plus petit sur ICESat-II permettra de réduire le bruit provenant du rayonnement solaire, ce qui permet d'améliorer la précision altimétrique.

1.2. Outil de simulation des formes d'onde LiDAR

Le modèle Wa-LiD développé dans cette thèse permet de simuler des trains d'onde LiDAR pour différentes configurations de capteurs LiDAR (longueur d'onde, puissance émise …), et pour différents milieux en eau (concentrations en sédiment, substance jaune (acides humiques), phytoplancton, etc). L'avantage de ce modèle est sa capacité à simuler des trains d'onde pour des longueurs d'onde de 300nm à 1500nm. De plus, ce modèle utilise les lois de transfert radiatif à travers l'eau et intègre une représentation géométrique explicite et paramétrable des propriétés de la surface de l'eau.

La qualité des simulations Wa-LiD a été analysée en comparant les simulations aux formes d'onde observées par le capteur satellitaire GLAS/ICESat-I sur le Lac Léman (proche infrarouge) et du capteur aéroporté HawkEye-II sur une zone côtière dans la partie nord de l'île de la Réunion dans les canaux du proche infrarouge et du vert. Les résultats montrent une bonne similarité des distributions des rapports signal à bruit (SNR) des trains d'ondes observés et des SNR des trains d'onde simulés. Cette comparaison à montrer aussi par, inversion sur des paramètres inconnus ou difficilement mesurables, certes limités, une bonne capacité du modèle à reproduire des formes d'onde observées.

Dans ce travail de thèse, nous avons supposé en première approche que les distributions des paramètres de l'eau étaient homogènes pour toute la profondeur de l'eau (une seule couche) et indépendantes entre elles. Aussi, notre modèle ne tient pas compte du phénomène de la stratification des propriétés dans la colonne d'eau et de la diffusion multiple provenant de particules en suspension multiple scattering »). En effet, les principaux phénomènes impliqués dans l'atténuation du signal lidar dans l'eau sont l'absorption et la diffusion simple, cette dernière étant dépendante de la nature et de la taille des particules (Cox et Munk, 1956). Un point important dans des travaux futurs serait d'intégrer la taille des diffuseurs dans la modélisation de la colonne d'eau et d'intégrer leurs effets dans le train d'onde simulé. Dans le modèle développé, la morphologie du fond pour chaque type de l'eau est considérée comme uniforme ayant une géométrie simplifiée (une seule pente globale). Nous n'avons donc pas considéré de rugosité du fond. En réalité, des géométries plus complexes de l'empreinte laser sur le sol (micro-géométrie) et des

éléments perturbateurs (les algues) seraient idéalement à prendre en compte dans le modèle.

En outre, le bruit ajouté dans nos simulations comprend à la fois le bruit du détecteur et le bruit provenant de radiations solaires. Les travaux de modélisation ne tiennent pas compte de facteurs supplémentaires à prendre en compte comme la couverture nuageuse, les aérosols (diffusion de Mie) et les molécules (diffusion de Rayleigh) qui interagissent avec le signal LiDAR (atténuation, diffusion multiple). Le milieu atmosphérique est constitué de molécules: vapeur d'eau, et de particules microniques en suspension : aérosols, gouttelettes, cristaux, hydrométéores et les cristaux: noyaux de congélation. Chaque particule ou molécule diffuse la lumière Laser dans toutes les directions suivant une indicatrice de diffusion qui dépend de sa taille, de sa forme, de son indice de réfraction. On parle, en effet, du bruit atmosphérique qui dépend de l'atténuation et du volume de diffusion par les particules et les molécules constituant l'atmosphère (Agishev et al., 2004; Belinkii, 1993).

En revanche, le simulateur Wa-LiD intègre un modèle détaillé de l'état de la surface de l'eau, selon le modèle de Cook et Torrance (1982) qui représente la surface comme une multitude de micro-facettes. Ce modèle est plus adaptable aux eaux continentales (rivières) si tant est que l'on dispose de lois de distributions de la rugosité de la surface de l'eau des eaux continentales (même problématique sur la rétrodiffusion des ondes radar sur les cours d'eau pour la mission SWOT). Il apparaît cependant plus difficilement transposable d'appliquer ce modèle à l'état de la surface de la mer qui est plus traditionnellement paramétré en fonction de la vitesse du vent qui, elle, permet la génération des vagues (Petri, 1977). Cox et Munk (1954) ont par exemple proposé un modèle empirique de réflectance-transmission à travers l'eau basé sur la distribution des pentes des vagues en fonction de l'angle d'incidence du capteur et de la direction du vent. La figure 2 représente la réflectance selon Cox et Munk (1954) en fonction de l'angle d'incidence du capteur pour une direction orthogonale à celle du vent. Cette figure montre que pour des petits angles d'incidence, la variation de la vitesse du vent n'a pas un grand effet. Si l'angle d'incidence augmente, un petit changement dans la vitesse du vent peut avoir un effet important sur la réflectance de la surface de l'eau. Il pourra être judicieux dans de futurs travaux d'intégrer une option du simulateur Wa-LID offrant la possibilité de

paramétrer l'état de la surface de la mer en lien avec la vitesse du vent et la direction du vent ou d'autres approches.

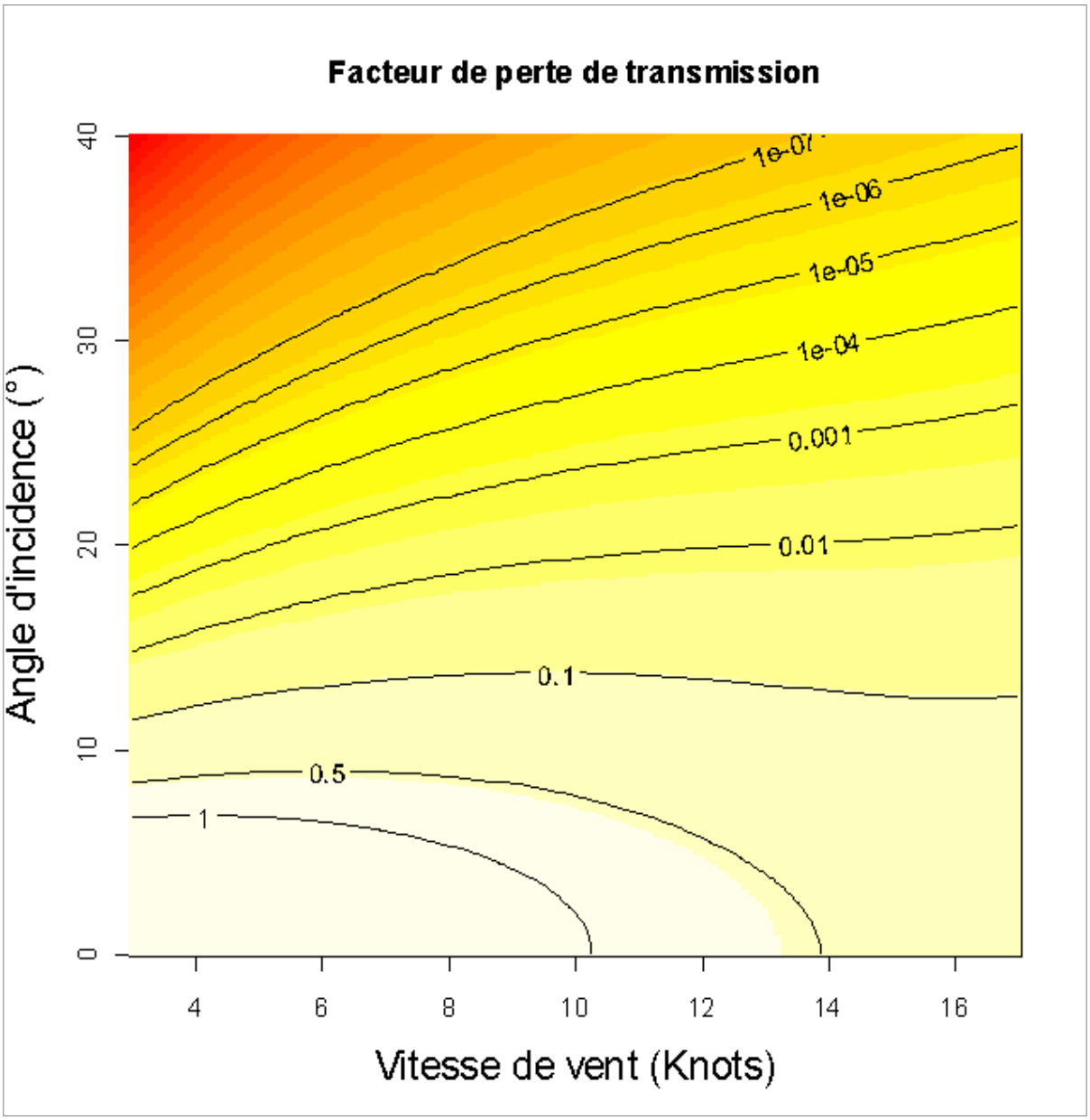

Fig. 2. Facteur de perte de transmission à travers la surface (Réflectance) en fonction de l'angle d'incidence et de la vitesse du vent (en nœuds marins) pour une direction orthogonale du vent.

1.3. Potentiel de deux configurations de futurs capteurs LiDAR satellitaires pour l'estimation de la bathymétrie

La performance bathymétrique de deux configurations de futurs capteurs LiDAR spatiaux émettant dans l'UV et le vert (Table 4), effectuée sur les eaux côtières, les rivières, les lacs profonds et les lacs peu profonds a été explorée en utilisant des formes d'ondes simulées suivant des distributions globales des différents paramètres de l'eau assumées comme représentatives à l'échelle mondiale.

System parameters	Units	Sensor 1 (355 nm)	Sensor 2 (532 nm)
Pulse duration (T_0)	ns	3	3.5
Digitizing frequency	GHz	1	1
Receiver Area (A_R)	m²	0.63	0.63
Emitted Power (P_e)	MW	1.4	0.4
Incidence angle (θ)	deg	0	0
Detector responsivity (R_λ)	A/W	0.15	0.25
Divergence angle (γ)	µrd	16	60
Spot size	m	8	30
Field of view (FOV)	µrd	24	90
Altitude (H)	km	500	500
Emitted Optical efficiencies (η_e)		0.8	0.8
Received Optical efficiencies (η_R)		0.5	0.5
Loss factor (F)		1	1
Receiver obscuration (γ_r)		0.1	0.1
Electrical bandwidth (B)	MHz	500	500
Excess noise (G)		3	3
Dark current (Id)	A	10^{-10}	10^{-10}

Table. 4. Configurations des deux futurs capteurs LiDAR satellitaires dans l'UV et le vert

L'analyse des formes d'onde a montré que les probabilités de détection du fond de l'eau (estimation possible de la bathymétrie) avec le LiDAR vert sont plus prometteuses. Les taux de détection pour le LiDAR UV sont toujours inférieurs à ceux du LiDAR vert pour les configurations instrumentales utilisées, et les taux diminuent drastiquement avec l'augmentation de la profondeur de l'eau et la turbidité pour un fond de pente nulle ou faible.

La méthode d'inversion simplifiée que j'ai développée pour estimer la bathymétrie, montre que, la précision sur l'estimation de la bathymétrie pour les deux capteurs est d'environ 2,8 cm si l'on ne tient compte que des erreurs liées à cette inversion. Cette précision est due principalement à la résolution de numérisation et aux erreurs de fitting (méthode d'inversion). Cette précision est également fonction de la répartition des profondeurs explorées (1m, 2m, 3m, 5m, 10m et 15m). Cependant, d'autres sources d'erreur ont été négligées dans cette étude. Ces erreurs proviennent en général du positionnement GPS du satellite, de la géométrie du faisceau laser, des conditions atmosphériques, de la complexité de la scène (présence de végétation), etc. (Charlton et al., 2003; Brinkman and O'Neill, 2000). Ainsi, la précision globale (écart-type de l'erreur aléatoire de bathymétrie) résulte de l'ajout des variances des différents éléments d'erreur:

• erreur du positionnement GPS du capteur d'environ 5 cm (Zwally et al., 2002).

• erreur due au pointage du faisceau laser d'environ 2 cm pour un satellite à 600 km d'altitude ayant un faisceau laser proche du nadir (Urban et al., 2008).

• erreur due à l'atmosphère d'environ 4 cm (Marini et Murray, 1973) (Zwally et al., 2002).

La somme de ces erreurs est cohérente avec le résultat des études de précision sur les données GLAS/ICESat rencontré dans la littérature sur des surfaces planes et non-complexe (Abdallah et al., 2011; Chipman and Lillesand, 2007).

2. Perspectives

Une innovation de cette thèse vient des méthodologies proposées pour estimer les performances globales et les facteurs limitant de deux configurations de futurs capteurs LiDAR satellitaires dédiés exclusivement ou partiellement à la bathymétrie. Bien sûr, les performances estimées dans cette thèse sont fortement liées à la base de données des formes d'onde simulées et les hypothèses de distribution des paramètres de l'eau, considérés comme représentatives à l'échelle mondiale.

2.1. Paramètres et limites

En ce qui concerne les paramètres du milieu ainsi que les configurations instrumentales utilisée dans cette thèse pour explorer les performances bathymétriques, des recherches complémentaires seront nécessaires pour affiner l'analyse au travers de la distribution de ces paramètres:

L'analyse de sensibilité menée est globale et dépend aussi bien de la structure du modèle (les équations) que de la distribution des paramètres du milieu. L'analyse de sensibilité sur le pic de fond a montré que trois paramètres ont la plus forte influence: les concentrations en sédiment, phytoplancton et substances jaunes (acides humiques). Par ailleurs, la pente du fond est aussi un paramètre qui influence fortement les formes d'ondes et a un impact direct sur la précision de l'estimation de la bathymétrie (cf. Figure 3). La figure 3 montre que pour une pente supérieure à 5°, son effet sur les formes d'ondes est très important. Cependant, l'effet de la pente du fond est resté limité dans l'analyse de sensibilité du fait de la distribution log-normal des pentes considérées (moyenne= 3 et écart type= 6) dans les simulations. Les paramètres de cette distribution prise globalement pour les quatre types d'eau définis dans cette thèse (eau côtière, rivière, lac profonde et lac peu profonde) ne sont pas toujours représentatifs par type. Pour les travaux futurs, il serait intéressant de raffiner les distributions de pente par type d'eau (eaux côtières, etc) à considérer pour mieux analyser l'effet global de la pente du fond sur la mesure de bathymétrie. A noter que la configuration UV est quatre fois moins sensible à la pente locale que la configuration « vert » compte tenu de la taille réduite du spot au sol.

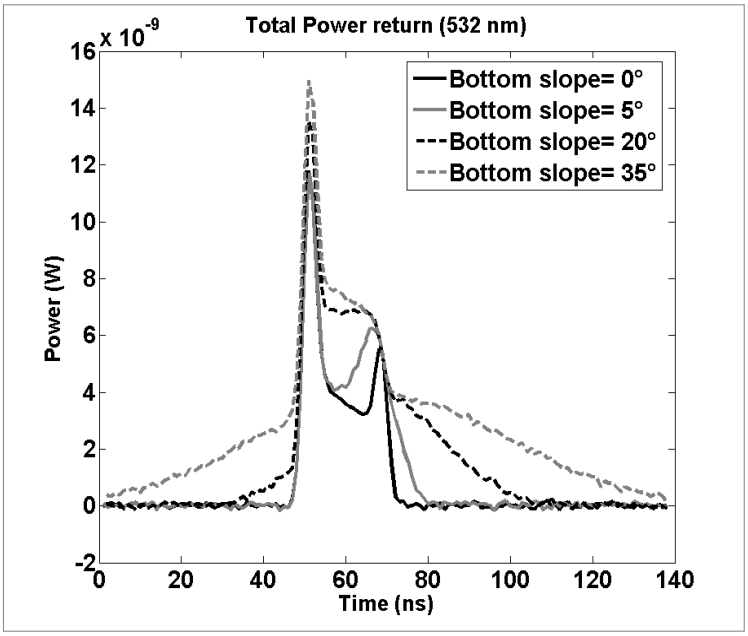

Fig. 3. Formes d'onde LiDAR simulées dans le vert (paramètres instrumentaux, cf. Table 4) pour une eau côtière (ay0=0.6 m-1, Cph=4 mg/m3, S=2.8 mg/l, r=0.1, Ks=0.9 Rb=0.12) et pour différentes pentes du fond à 2 m de profondeur.

2.2. Vert ou UV ?

L'analyse des performances bathymétriques dans le chapitre 3 des lasers vert et UV a montré le fort potentiel du vert. En effet, le laser vert (532 nm) est la longueur d'onde la plus utilisée par les LiDAR bathymétriques. L'avantage de cette longueur d'onde est sa capacité à pénétrer l'eau alors que l'UV est plus atténuée dans l'eau (impure). Le vert est très limité par la sureté oculaire au niveau d'énergie émise. La figure 4 présente des trains d'ondes simulés dans le vert et l'UV avec respectivement des empreintes de 8 m (Fig. 4a) et de 30 m (Fig. 4b). La figure 4a montre que pour de petite empreinte (8 m) et avec une énergie plus importante on peut pénétrer aussi bien dans l'UV que dans le vert. Ainsi que pour une énergie émise dans l'UV de l'ordre de 28 mJ (énergie maximale permise), on pourrait s'attendre à des performances bathymétriques plus élevées (probabilité de détection plus élevée) que celles obtenues avec une énergie émise de 15mJ. Tandis que pour des grandes empreintes (30 m) le vert reste plus performant que l'UV à haute énergie (Fig. 4b).

En plus, l'UV a prouvé ses potentialités pour des applications atmosphériques (Browell et al., 1998) et forestières (Allouis et al., 2011). Dans les futurs travaux, il serait nécessaire de réfléchir à des futures missions LiDAR satellitaires en utilisant des longueurs d'ondes pouvant être utilisées pour plusieurs applications thématiques (UV par exemple). En utilisant une longueur d'onde qui pourra fédérer plusieurs applications (atmosphérique, forestière et bathymétrique), nous pourrions espérer une plus grande chance de voir aboutir une mission spatiale LiDAR.

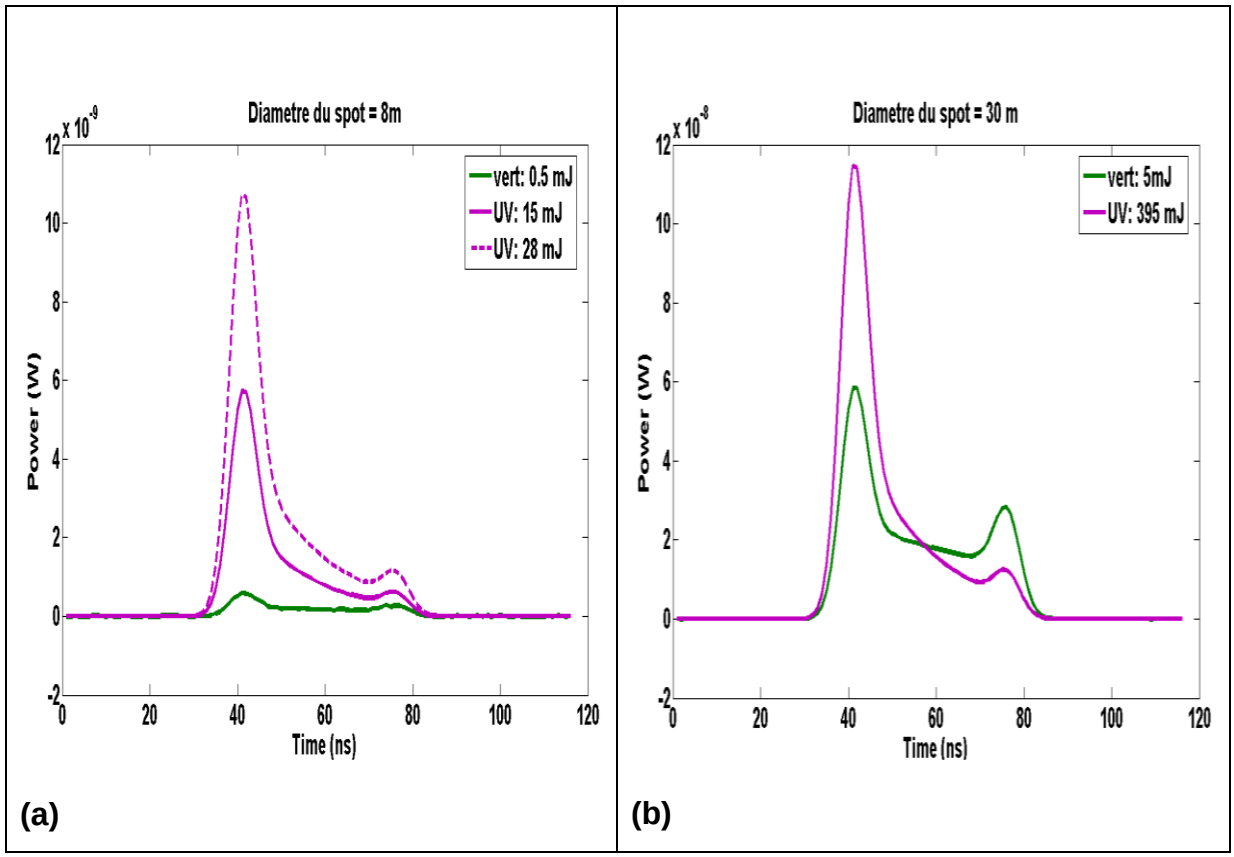

Fig.4. Trains d'ondes simulées dans l'UV et le vert dans une eau côtière à 2 m de profondeurs. a) pour un spot de 8 m utilisant les énergies maximale permise pour l'UV et le vert (0.5 mJ et 28 mJ, respectivement) et l'énergie émise utilisée dans notre configuration UV (15 mJ). b) pour un spot de 30 m utilisant les énergies maximales permises pour l'UV et le vert (5 mJ et 395 mJ respectivement)

2.3. Méthode d'inversion

Dans le traitement des formes d'ondes, d'autres méthodes de filtrage pourraient être testées sur le signal LiDAR (convolution par gaussienne par exemple). Pour les fonctions d'ajustement des différents retours LiDAR, et surtout pour celui de la

colonne d'eau, nous avons utilisé une fonction triangle qui n'a pas parfaitement ajusté la contribution de la colonne d'eau. En outre, cette fonction semble causer une sous-estimation de la bathymétrie. Dans des travaux futurs, nous pourrions tester d'autres fonctions pour mieux ajuster la contribution de la colonne d'eau, avec une fonction trapèze par exemple. De plus, la principale limitation est que notre méthode d'inversion n'est pas adaptée pour les eaux très peu profondes (<1 m). D'autres méthodes de traitement de formes d'onde devraient être développées pour estimer ces faibles profondeurs.

2.4. LiDAR Satellitaire

L'utilisation des données LIDAR à partir d'une plate-forme satellite présente plusieurs avantages qui semblent prometteuses pour de futures recherches. Récemment, des recherches ont été menées dans ce sens en utilisant les données du satellite CALIPSO (Cloud Aerosol Lidar and Infrared Pathfinder Satellite Observations). En effet, le satellite CALIPSO a été lancé en 2006 pour étudier les impacts radiatifs des nuages et des aérosols. L'objectif de CALIPSO est d'améliorer la modélisation de l'évolution du climat, de fournir des mesures globales du profil vertical de l'atmosphère et les propriétés optiques des couches nuageuses et des aérosols : tous ces paramètres permettent de mieux cerner le rôle des aérosols et des nuages dans le climat. L'instrument LiDAR du CALIPSO est similaire à celui du GLAS. Ce capteur fonctionne avec deux longueurs d'onde différentes (1064 nm et 532 nm) à 705 km d'altitude, avec un angle d'incidence de 3°, un FOV de 160 µrad, des empreintes au sol de 70 m espacées de 330 m, et un pulse émis d'une largeur de 20 ns et d'une énergie de 100 mJ (Hu et al., 2007). Le récepteur de CALIPSO possède un élément de polarisation qui permet d'atténuer les réflexions de surface. L'interaction du signal avec l'eau permet de réfléchir la lumière avec une polarisation changée. On quantifie la modification de l'état de polarisation lumineuse par le calcul du rapport de dépolarisation. Le rapport de dépolarisation est une mesure extrêmement utile car elle permet de distinguer facilement la cible détectée.

Si l'eau est claire et peu profonde (< 20 m) et dans des très bonnes conditions atmosphériques (sans nuages), le signal CALIPSO dans le vert (532 nm) pénètre dans la colonne d'eau et atteint le fond.

Battaglia (2010) a évalué le potentiel du LiDAR vert polarisé de CALIPSO pour détecter la bathymétrie des eaux côtières aux Bahamas et dans l'atoll de Kure. Les

principaux résultats de cette étude montrent que : i) CALIPSO permet de détecter de manière fiable les eaux claires peu profondes jusqu'a environ 20 m et ii) la précision bathymétrique de CALIPSO (30 - 60 cm) est sensiblement plus faible en comparaison aux systèmes LIDAR aéroportés tels que SHOALS (15 cm).

Bibliographie

Abdallah H., Bailly J.S., Baghdadi N., and Lemarquand N. (2011). Improving the assessment of ICESat water altimetry accuracy accounting for autocorrelation. *ISPRS Journal of Photogrammetry and Remote Sensing*, 66 (6), pp. 833-844.

Abdalati W., Zwally H., Bindschadler R., Csatho B., Farrell S.L., Fricker H.A., Harding D., Kwok R., Lefsky M., Markus T., Marshak A., Neumann T., Palm S., Schutz B., Smith B., Spinhirne L. and Webb C. (2010). The ICESat-2 Laser Altimetry Mission," *Proceedings o/the IEEE*, 98 (5), pp.735-751.

Ackermann F. (1999). Airborne laser scanning--present status and future expectations. *ISPRS Journal of Photogrammetry and Remote Sensing*, 54, pp.64-67.

Agishev R., Comeron A., Gross B., Moshary F., Ahmed S. and Gilerson A. (2004). Application of the method of decomposition of lidar signal-to-noise ratio to the assessment of laser instruments for gaseous pollution detection. *Applied Physics B*, 79 (2), pp. 255-264.

Aladin N., Crétaux J., Plotnikov I.S., Kouraev A.V., Smurov A.O., Cazenave A., Egorov A.N. and Papa F. (2005). Modern hydro-biological state of the Small Aral sea. *Environmetrics*, 16 (4), pp. 375–392.

Adler-Golden S.M., Acharya P.K., Berka A., Matthew M.W. and Gorodetzky D. (2005). Remote Bathymetry of the Littoral Zone From AVIRIS, LASH, and Quickbird Imagery, *IEEE Trans. Geosci. and Rem. Sens.*, 43(2), pp. 337-347.

Allouis T., Durrieu S., Chazette P., Bailly J.-S., Cuesta J., Véga C., Flamant P. and Couteron P. (2001). Potential of an ultraviolet, medium-footprint lidar prototype for retrieving forest structure", *ISPRS Journal of Photogrammetry and Remote Sensing*, 66 (6), pp. S92-S102.

Baltsavias E.P. (1999). Airborne laser scanning: existing systems and firms and other resources. *ISPRS Journal of Photogrammetry and Remote Sensing*, 54, pp.164-198.

Battaglia N. (2010). Utility of satelitte LiDAR waveform data in shallow water. Master thesis, Naval Postgraduate School, Monterey, pp. 85.

Belen'kii M. S. (1993). Effect of atmospheric turbulence on heterodyne lidar performance. *Appl. Opt*. 32, pp. 5368–5372.

Bercher N. (2008). Précision de l'altimétrie satellitaire radar sur les cours d'eau. Ph.D. thesis, AgroParisTech.

Beres M., and Haeni F.P. (1991). Application of ground-penetrating-radar methods in hydrogeologic studies. *Ground Water*, 29 (3), pp. 375-386.

Bergeon B. (2004). L'altimétrie par laser scanner aéroporté. *Géomatique Expert*, 35, pp.19-24.

Bhang K.J., Schwartz F.W. and Braun A. (2007). Verification of the vertical error in Cband SRTM DEM using ICESat and Landsat-7, Otter Tail County, MN. *IEEE Transactions on Geoscience and Remote Sensing*, 45 (1), pp. 36–44.

Bierwirth P.N., Lee T. and Burne R.V. (1993). "Shallow sea-floor reflectance and water depth derived by unmixing multispectral imagery", *Photogrammetric Engineering & Remote Sensing*, 59 (3), pp. 331-338.

Binding C.E., Bowers D.G. and Mitchekson-Jacob E.G. (2005). Estimating suspended sediment concentration from ocean colour measurements in moderately turbid waters; the impact of variable particle scattering properties, *Remote Sensing of Environment*, 94, pp. 373-383.

Birkett C.M. (1995a). The contribution of Topex/Poseidon to the global monitoring of climatically sensitive lakes. *J. Geophys. Res.,* 100 (C12), pp. 25179-25204.

Birkett C.M. (1995b). The global remote sensing of lakes, wetlands and rivers for hydrological and climate research. *Geoscience and Remote Sensing Symposium, Quantitative Remote Sensing for Science and Applications*, 3. pp. 1979–1981.

Birkett C. M. (1998). Contribution of the topex nasa radar altimeter to the global monitoring of large rivers and wetlands. *Water Resources Research*, 34(5), pp. 1223–1239.

Birkett C.M., Murtugudde R. and Allan T. (1999). Indian Ocean climate event brings floods to east Africa's lakes and the Sudd Marsh. *Geophys. Res. Lett*. 26, pp. 1031-1034.

Birkett C. M. (2000). Synergistic remote sensing of lake chad : variability of basin inundation. *Remote Sensing Environnement*, 72, pp. 218–236.

Birkett C.M., Mertes L.A.K., Dunne T., Costa M. and Jasinski J. (2002) Altimetric remote sensing of the Amazon: application of satellite radar altimetry. *J Geophys Res*, 107 (D20), p. 8059.

Bisquay H., Lannuzel S. and Michaux P. (2001). Evaluation des performances bathymétrqiues d'un sondeur multifaisceaux. Guide technique de l'Epshom, 44 p.

Bolideau C. (2010). *Apports du LiDAR à l'étude de la végétation des marais salés de la baie du Mont-Saint-Michel.* Ph.D. thesis Univ Paris-Est Marne-la-Vallée.

Brando V.E., Janet M.A., Magnus W., Arnold G. D., Stuart R. Ph., and Chris. R. (2009). A physics based retrieval and quality assessment of bathymetry from suboptimal hyperspectral data. *Remote Sensing of Environment*, 113, pp. 755-770.

Brinkman R.F. and O'Neill C. (2000). LiDAR and photogrammetric mapping. *The Military Engineer*, May-June 2000.

Brooks R.L. (1982). Lake elevation from satellite radar altimetry from a validation area in Canada. Report, Geosci. Res.

Browell E.V., Ismail S. and Grant W.B. (1998). Differential absorption lidar (DIAL) measurements from air and space", *Applied Physics B: Lasers and Optics*, 67 (4), pp. 399-410.

Brown G.S. (1977). Skylab S-193 radar experiment analysis and results, *NASA report NASA CR-2763*, Feb. 1977.

Brown L.R. (2011). World on the edge: How to prevent environmental and economic collapse. New York: *W. Norton & Co Inc.*

Calmant S. and Seyler F. (2006). Continental surface waters from satellite altimetry. *Comptes rendus. Géoscience*, 338 (14-15), pp.1113–1122.

Cazenave A., Bonnefond P. and DoMinh K. (1997). Caspian Sea level from Topex/Poseidon altimetry: level now falling. *Geophys. Res. Lett.* 24, pp. 881-884.

Cazenave A. and Nerem S. (2002). Redistributing earth's mass. *Science*, 297:783–784.

Chaponnière P. (2004). Teledetection et bathymetrie des rivieres: application a la Durance. Master's thesis, Ecole Nationale Superieure de Geologie (ENSG).

Charlton M.E., Large A.R.G. and Fuller I.C. (2003). Application of airborne lidar in river environments: The River Coquet. *Northumberland, UK. Earth Surface Processes and Landforms*, 28, pp. 299-306.

Chipman J.W. and Lillesand T.M. (2007). Satellite-based assessment of the dynamics of new lakes in southern Egypt. *International Journal of Remote Sensing*, 28 (19), pp. 4365–4379.

Clark S. and Edwards A.J. (1995). Coral transplantation as an aid to reef rehabilitation: Evaluation of a case study in the Maldive Islands. *Coral Reefs*, 14, pp. 201-213.

Cook R. L. and Torrance K. E. (1982). A Reflectance Model for Computer Graphics. *ACM Transactions on Graphics*, 1, pp. 7 – 24.

Cosgrove B. and Rijsberman F. (2000). World water vision. *Journal of Hydraulic Research/De Recherches Hydrauliques*, 38 (4), p. 57.

Cox C. and Munk W. (1954). Measurement of the roughness of the sea surface from photographs of the sun'sglitter. *J. Opt. Soc. Am.*, 44, pp. 838-850.

Cox C. and Munk W. (1956). Slopes of the sea surface deduced from photographs of sun glitter, Bull. Scripps Inst. Oceanography, 6 (9), pp. 401-488.

Cretaux J. and Birkett C. (2006). Lake studies from satellite radar altimetry. *Comptes Rendus Geosciences*, 338, Issues 14-15, La Terre observée depuis l'espace, November December, pp. 1098–1112.

Cunningham A., Lillycrop W. J., Guenther G. C. and Brooks M. (1998). Shallow water laser bathymetry: accomplishments and applications. *Proceedings of the XVth Oceanology International Exhibition & Conference*, Brighton, 3, pp. 277-288.

Degnan J. J. (2002). BPhoton-counting multikilohertz microlaser altimeters for airborne and spaceborne topographic measurements. *J.Geodyn*., 34 (3–4), pp. 503–549.

De Joinville O., Ferrand B. and Roux M. (2002). Levé laser aéroporté: état de l'art, traitement des données et comparaison avec des systèmes imageur. *Revue Française de Photogrammétrie et de Télédétection*, 166, pp.72-81.

De Oliveira Campos I., Mercier F., Maheu C., Cochonneau G., Kosuth P., Blitzkow D. and Cazenave A. (2001). Temporal variations of river basin waters from topex/poseidon satellite altimetry. Application to the amazon basin. *Earth and planetary sciences*, 333, pp. 633–643.

Duda A. M. and El-Ashry M. T. (2000). Addressing the global water and environment crises through integrated approaches to the management of land, water and ecological resources. *Water International*, 25 (1), pp. 115-126.

Esteves L.S., Toldo Jr. E.E., Dillenburg S.R. and Tomazelli L.J (2002). Long- and short-term coastal erosion in southern Brazil**.** *Journal of Coastal Research*, 36, pp. 273–282.

Ferrari R.L. and Collins K.L. (2006). Reservoir survey and data analysis. In: *Erosion and Sedimentation Manual*, Chapter 9, CT Yang (ed). Bureau of Reclamation, Technical Service Center, Denver, CO.

Feurer D., Bailly J-S., Puech C., LeCoarer Y., and Viau A. (2008). Very high resolution mapping of river immersed topography by remote sensing. *Progress in Physical Geography*, 32 (4), pp. 1–17.

Frappart F., Seyler F., Martinez J.-M., Leon J. G. and Cazenave A. (2005). Floodplain water storage in the negro river basin estimated from microwave remote sensing of innundation area and water levels. *Remote Sensing of Environment*, 99, pp. 387–399.

Gao J. (2009). Bathymetric mapping by means of remote sensing: methods, accuracy and limitations. *Progress In Physical Geography*, 33, pp. 103–116.

Gilvear D.J., Davids C. and **Tyler A.N.** (2004). The use of remotely sensed data to detect channel hydromorphology. River Tummel, Scotland. *River Research and Applications*, 20, pp. 795–811.

Gopinath G. and Seralathan P. (2005). Rapid erosion of the coast of Sagar island, West Bengal - India. *Environmental Geology*, 48 (8), pp. 1058-1067.

Guenther G.C., Cunningham A.G., LaRocque P.E., and Reid D.J. (2000). Meeting the accuracy challenge in airborne LiDAR bathymetry. *Proc. 20th EARSeL Symposium: Workshop on LidarRemote Sensing of Land and Sea*, June 16-17, Dresden, Germany.

Heege T., Hausknecht P. and Kobryn H. (2007). Hyperspectral seafloor mapping and direct bathymetry calculation using HyMap data from the Ningaloo reef and Rottnest Island areas in Western Australia. *Proceedings 5th EARSeL Workshop on Imaging Spectroscopy*, Bruges, Belgium, April 23-25 2007, pp. 1-8.

Hell B. (2011). Mapping bathymetry from measurement to application. PHD thesis, Department of Geological Sciences Stockholm University Sweden.

Hardy T.B., Anderson, P.C., Neale, M.U. and **Stevens D.K. (**1994). Application of multispectral videography for the delineation of riverine depths and mesoscale hydraulic features. In Marston, R. and Hasfurther, V., editors, *Effects of human-induced changes on hydrologic systems*, Symposium of the American Water Resources Association, Jackson Hole, Wyoming, pp. 445–54.

Hilldale R.C. and Mooney D.M. (2007). Identifying stream habitat features with a two-dimensional hydraulic model. Prepared for the Yakima River Basin Water Storage Feasibility Study, Bureau of Reclamation, Technical Service Center, Denver, CO, January.

Hilldale R.C. and Raff D. (2007). Assessing the ability of airborne LIDAR to map river bathymetry. *Earth Surface Processes and Landforms*, 33 (5), pp. 773–783.

Hodgson M. and Bresnahan P. (2004). Accuracy of Airborne Lidar-Derived Elevation: Empirical Assessment and Error Budget. *Photogrammetric Engineering & Remote Sensing*, 70, pp. 331-340.

Houghton J.I., Quarmby J. and Stephenson T. (2001). Municipal wastewater sludge dewaterability and the presence of microbial extracellular polymer. *Water Science and Technology*, 44 (2-3), pp. 373-379.

Hu Y., Powell K., Vaughan M., Tepte C., Weimer C. and Beherenfeld B. (2007). Elevation information in tail (EIT) technique for LIDAR altimetry. *Opt Express* **15**, pp. 14504–14515.

IHO Standards for Hydrographic Surveys , (5th Edition, February 2008 Special Publication No. 44, Published by the International Hydrographic Bureau Monaco).

IEC, International Electrotechnical Committee, Amendment 2 to IEC 60825-1, Safety of laser products – Part 1: Equipment classification, requirements and user's guide, Geneva, 2001.

ICNIRP, International Commission on Non-Ionizing Radiation Protection (1997). Guidelines on Limits of Exposure to Broad-band Incoherent Optical Radiation (0,38 to 3 μm). *Health Physics* 73**,** pp. 539-554.

ICNIRP, International Commission on Non-Ionizing Radiation Protection (2000). Revision of guidelines on limits of exposure to laser radiation of wavelengths between 400 nm and 1.4 μm, *Health Phys*, 79, pp. 431-440.

Jay S., Guillaume M. and Blanc-Talon, J. (2012). Underwater Target Detection With Hyperspectral Data: Solutions for Both Known and Unknown Water Quality, *Selected Topics in Applied Earth Observations and Remote Sensing, IEEE Journal of* , 5(4), pp.1213-1221.

Jerlov N. (1976). *Marine optics*. Amsterdam: Elsevier.

Jing E. and Datt. B. (2010). Detection of coastal bathymetry using hyperspectral imagery, *OCEANS 2010 IEEE - Sydney* , pp.1-4.

Jolivet P., Pastol Y. and Lamarre V. (2009). Litto3D– v 1.0, spécifications techniques de la base de données SHOM/IGN « Litto3D». *Rapport technique Version 1.4*, pp. 16.

Kanno A. and Tanaka, Y. (2012). Modified Lyzenga's Method for Estimating Generalized Coefficients of Satellite-Based Predictor of Shallow Water Depth, *Geoscience and Remote Sensing Letters, IEEE* , 9(4), pp.715-719.

Kenny A.J., Andrulewicz E., Bokuniewicz H., Boyd S.E., Breslin J. (2000). An overview of seabed mapping technologies in the context of marine habitat classification. *Annual Report of ICES WGEXT*.

Kinzel P. J., Wright C. W., Nelson J. M. and Burman A. R. (2007). Evaluation of an experimental LIDAR for surveying a shallow, braided, sand bedded river. *Journal of Hydraulic Engineering*, 133 (7), pp. 838–842.

Koblinsky C.J., Clarke R.T., Brenner A.C. and Frey H. (1993). Measurements of river level variations with satellite altimetry, *Wat. Resour. Res.* 29(6), pp.1839-1848.

Kosuth P., Blitzkow D. et Cochonneau G. (2006). Establishment of an altimetric reference network over the amazon basin using satellite radar altimetry (topex/poseidon). In *Venice 2006 Symposium "15 years of progress in radar altimetry"*.

Kouraev A., Zakharova E., Samain O., Mognard N. and Cazenave A. (2004). Ob' river discharge from topex/poseidon satellite altimetry (1992-2002). *Remote Sensing of Environment*, 93, pp. 238–245.

Lafon V., Froidefond J.M., Lahet F. and Castaing P. (2002). SPOT shallow water bathymetry of a moderately turbid tidal inlet based on field measurements," *Remote Sensing of Environment*, 81, pp. 136-148.

Lane S.N., Chandler J.H. and Richards K.S. (1994). Developments in monitoring and terrain modeling small-scale river-bed topography. *Earth Surface Processes and Landforms* 19, pp. 349 – 368.

Leckie D., Cloney E., Jay C. and **Paradine D.** (2005). Automated mapping of stream features with high-resolution multispectral imagery: an example of the capabilities. *Photogrammetric Engineering and Remote Sensing*, 71, pp. 145–55.

Lee H., Shum C. K., Yi Y., Ibaraki M., Kim J. -W., Braun A., Kuo C. -Y., and Lu Z. (2009). Louisiana wetland water level monitoring using retracked TOPEX/POSEIDON altimetry. *Marine Geodesy*, 32, pp. 284−302.

Lee Z.P., Carder K.L., Hawes S.K., Steward R.G., Peacok T.G. and Davis C.O. (1994). A model for interpretation of hyperspectral remote sensing reflectance », *Applied Optics*, 33, pp. 5721-5732.

Lee Z.P., Carder K.L., Mobley C.D., Steward R.G., and Patch J.S. (1998). Hyperspectral remote sensing for shallow waters: A semi-analytical model. *Applied Optics*, 37, pp. 6329-6338.

Lee Z.P., Carder K.L., Mobley C.D., Steward R.G. and Patch J.S. (1999). Hyperspectral remote sensing for shallow waters : Deriving bottom depths and water properties by optimization. *Applied Optics*, 38, pp. 3831-3843.

LEI M. (2011). Simulation d'images d'un futur imageur multispectral géostationnaire dédié à la couleur de l'eau.Université de Bourgogne, pp. 164

Lesser M.P. and Mobley C.D. (2007). Bathymetry water optical properties and benthic classification of coral reefs using hyperspectral remote sensing imagery, *Coral Reefs*, 26, pp. 819-829.

Lillycrop W.J., Parson L.E., Irish J.L. and Brooks M.W. (1996). Hydrographic surveying with an airborne LiDAR survey system. Presented at the Second International Airborne Remote Sensing Conference and Exhibition, San Francisco, CA, June 24-27.

Liew S.H., Chen P., Saengtuksin B. and Chew Wai Chang, (2011). Estimating water optical properties, water depth and bottom albedo using high resolution satellite imagery for coastal habitat mapping, Geoscience and Remote Sensing Symposium (IGARSS), IEEE International, pp.2338-2340.

Loubersac L., Burban P.Y., Lemaire O., Varet H. and Chenon F. (1991). Integrated study of Aitutaki's lagoon (Cook Islands) using SPOT satellite data and in situ measurements : bathymetric modelling. *Geocarto Int.*,6, pp. 31-37.

Lurton X. (2000). Swath bathymetry using phase difference: theoretical analysis of acoustical measurement precision. *IEEE Journal of Oceanic Engineering*, 25 (3), pp. 351-363.

Lysenga D. R. (1978). Passive remote sensing techniques for mapping water depth and bottom features. *Applied Optics*, 17 (3), pp. 379-383.

Lyzenga,D.R., Malinas N.P. and **Tanis F.J.** (2006). Multispectral bathymetry using a simple physically based algorithm. *IEEE Transactions on Geoscience and Remote Sensing* 44, pp. 2251–2259.

Maheu C., Cazenave A. and Mechoso C.R. (2003). Water level fluctuations in the plata basin (south america) from topex/poseidon satellite altimetry. *Geophysical research letters*, 30 (3), pp.1143–1146.

Marcus W.A., Leigleiter C.J., Aspinall R.J, Boardman J.W. and Crabtree RL. (2003). High spatial resolution hyperspectral mapping of in-stream habitats, depths, and woody debris in mountain streams. *Geomorphology*, 55, pp. 363 – 380.

Marini J.W. and Murray C.W. (1973). Correction Of Laser Range Tracking Data For Atmospheric Refraction At Elevation Angles Above 10°. *NASA Technical Report*.

Maritorena S., Morel A. and Gentili B. (1994). Diffuse reflectance of oceanic shallow waters : influence of water depth and bottom albedo. *Limnology and Oceanography*, 39, pp. 1689-1703.

Maritorena S. (1996). Remote sensing of the water attenuation in coral reefs : a case study in French Polynesia. *International Journal of Remote Sensing*, 17, pp. 155-166.

Marks K. and Bates P. (2000). Integration of high-resolution topographic models with floodplain flow models. *Hydrological Processes*, 14, pp. 2109-2122.

Mason I.M., Rapley C.G., Street-Perrott F.A. and Guzkowska M. (1985). ERS-1 observations of lakes for climate research. *Proc. EARSeL/ESA* Symposium "European Remote Sensing Opportunities", Strasbourg, 31 March-3 April 1985.

McCulloch M. , Forbes D.L. and Shaw J. (2002). Coastal Impacts of Climate Change and Sea-level Rise on Prince Edward Island. *Geological Survey of Canada, Dartmouth, NS*, Scientific Team Synthesis report, 1, pp. 65.

McGranahan G., Deborah B. and Bridget A. (2007). The rising tide: assessing the risks of climate change and human settlements in low elevation coastal zones. *Environment & Urbanization* 19(1), pp. 17-37.

Mercier F. (2001). Altimétrie spatiale sur les eaux continentales : apport des missions Topex/Poseidon et ERS1&2 à l'étude des lacs, mers intérieures et bassins fluviaux. Thèse Univ. Toulouse III-Paul Sabatier, 9/11/2001, 190p.

Mercier F., Cazenave A. and Maheu C. (2002). Interannual lake level fluctuations (1993-1999) in Africa from Topex/Poseidon: connections with ocean-atmosphere interactions over the Indian ocean. *Global and Planetary Changes*, 32, pp. 141-163.

Miles E. L. (1998). "The concept of ocean governance: Evolution towards the 21st century and the principle of sustainable ocean use. Paper prepared for SEAPOL workshop on ocean governance and system compliance in the Asia-Pacific context. *Rayong, Thailand, 1997.*

Miller L.S. (1979). Topographic and backscatter characteristics of GEOS 3 overland data. *Journal of geophysical research*, 84 (B8), pp. 4045-4054.

Morris C.S. and Gill S.K. (1994a). Variation of great lakes waters from Geosat altimetry. *Water Resour. Res*., 30, pp. 1009-1017.

Morris C.S. and Gill S.K. (1994b). Evaluation of the Topex/Poseidon altimeter system over the great Lakes. *J. Geophys. Res*., 99 (C12), pp. 24527-24539.

Petri K.J. (1977). Laser radar reflectance of Chesapeake Bay waters as a function of wind speed. *IEEE Trans. Geoscience Electronics* GE-15, 2, pp. 87-96.

Philpot W.D. (1989). Bathymetric mapping with passive multispectral imagery. *Applied Optics*, 28, pp. 1569-1578.

Ponchaut F. and Cazenave A. (1998). Continental lake level variations from Topex/Poseidon (1993-1996). C. R. Acad. Sci. Paris, 326, pp. 13-20.

Renard V. and Allenou J.P. (1979). Le sea-beam, sondeur à multi-faisceaux du N/O "Jean Charcot" description, évaluation et premiers résultats. *Revue Hydrographique Internationale*, 56(1), pp. 557-593.

Ruggiero P., Komar P.D., McDougal W.G., Marra J.J. and Beach R.A. (2001). Wave runup, extreme water levels and the erosion of properties backing beaches. *Journal of Coastal Research*, 17 (2), pp. 407-419.

Service Hydrographique de Canada (2006). Synthèse critique des outils de télédétection appliqués à la cartographie des habitats benthiques en domaine côtier. *Revue bibliographique*, pp. 153.

Spicer K.R., Costa J.E., and Placzek G. (1997). Measuring flood discharge in unstable stream channels using ground-penetrating radar, *Geology*, 25, pp. 423-426.

Stocks T. (1937). Morphologie des Atlantischen Ozeans. In Wissenschaftliche Ergebnisse der Deutschen Atlantischen Expedition auf dem Forschungs- und Vermessungsschiff Meteor, 3, pp. 1925–1927.

Tulldahl H. M. and Steinvall K. O. (1999). Analytical Waveform Generation from Small Objects in LIDAR Bathymetry. *Applied Optics*, 38 (6), pp. 1021-1039.

Urban T.J., Schutz B.E. and Neuenschwander A.L. (2008). A survey of ICESat coastal altimetry applications: continental coast, open ocean island, and inland river. *Terrestrial, Atmospheric and Oceanic Sciences*, 19 (1-2), pp. 1–19.

Von Szalay, P. G., and McConnaughey R. A. (2002). The effect of slope and vessel speed on the performance of a single beam acoustic seabed classification system. *Fisheries Research*, 54, pp. 181−194.

Vörösmarty C.J., Green P., Salisbury J. and Lammers, R.B. (2000). Global water resources: Vulnerability from climate change and population growth. *Science*, 289 (5477), pp. 284-288.

Walther S.C., Marcus W., Fonstad M.A. (2011). Evaluation of high-resolution, true-colour, aerial imagery for mapping bathymetry in a clear-water river without ground-based depth measurements. *International Journal of Remote Sensing*, 32 (15), pp. 4343-4363.

Ward K. and Gallagher B. (2011). Utilizing Vessel Traffic and Historical Bathymetric Data to Prioritize Hydrographic Surveys. *The Hydrographic Society of America*.

Westaway R.M., Lane S.N., Hicks D.M. (2000). Development of an automated correction procedure for digital photography for the study of wide, shallow gravel-bed rivers. *Earth Surface Processes and Landforms* 25, pp. 200-226.

Winterbottom SJ and Gilvear DJ. (1997). Quantification of channel bed morphology in gravel bed rivers using multispectral imagery and aerial photography. *Regulated Rivers: Research and Management,* 13, pp. 489 - 499.

Wirth H. and Brüggemann T. (2011). The development of a multiple transducer multi-beam echo sounder system for very shallow waters FIG Working Week 2011 Bridging the Gap between Cultures Marrakech, Morocco, 18-22 May.

Zwally H.J., Schutz B., Abdalati W., Abshire J., Bentley C., Brenner A., Bufton J., Dezio J., Hancock D., Harding D., Herring T., Minster B., Quin, K., Palm S., Spinhirne J. and Thomas, R. (2002). ICESat's laser measurements of polar ice, atmosphere, ocean, and land. *Journal of Geodynamics* 34 (3-4), pp. 405–445.

Yu A.W., Stephen M.A., Li S. X., Shaw G.B., Seas A., Dowdye E., Troupaki E., Liiva P., Poulios D., and Mascetti K. (2010). Space laser transmitter development for ICESat-2 mission. *Proc. SPIE*, 7578, 757809.